RHEOLOGICAL AND MORPHOLOGICAL CHARACTERIZATION OF HIERARCHICALLY NANOSTRUCTURED MATERIALS

by

Benjamin Ning-Haw Wang

B.S., Chemical Engineering
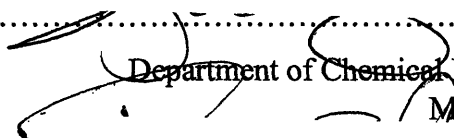
Stanford University 1998

Submitted to the Department of Chemical Engineering
in Partial Fulfillment of the Requirements for the Degree of

Doctor of Philosophy in Chemical Engineering
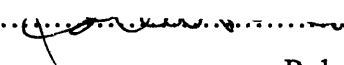at the
Massachusetts Institute of Technology

JUNE 2007

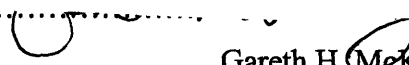© 2007 Massachusetts Institute of Technology
All rights reserved

Signature of Author...
Department of Chemical Engineering
May, 23, 2007

Certified by...
Robert E. Cohen
St. Laurent Professor of Chemical Engineering
Thesis Supervisor

Certified by...
Gareth H. McKinley
SoE Professor of Teaching Innovation in Mechanical Engineering
Thesis Supervisor

Accepted by..
William J. Deen
Carbon P. Dubbs Professor of Chemical Engineering
Chairman, Committee for Graduate Students
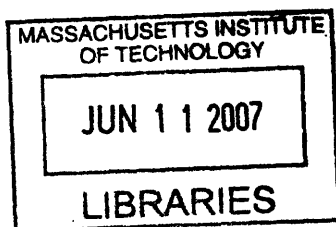
1

RHEOLOGICAL AND MORPHOLOGICAL CHARACTERIZATION OF HIERARCHICALLY NANOSTRUCTURED MATERIALS

by

Benjamin N. Wang

Submitted to the Department of Chemical Engineering on May 23, 2007
in Partial Fulfillment of the Requirements for the Degree of
Doctor of Philosophy in Chemical Engineering

ABSTRACT

Hierarchically nanostructured materials exhibit order on multiple length scales, with at least one of a few nanometers. The expected enhancements for applications using these materials include improved mechanical, thermal and electrical properties; however, control of the morphology which governs material performance and fabrication remains a challenge. The development of novel quantitative characterization techniques is important to connect the underlying morphology to relevant processing parameters and macroscopic behavior. Rheological and morphological analysis can illustrate these governing structure-property relationships for hierarchically nanostructured materials based on "0-D" polyhedral oligomeric silsesquioxane (POSS) particles, "1-D" carbon nanotubes (CNTs), and "2-D" clay nanoparticles.

We develop a technique, using small-angle X-ray scattering, which provides quantitative measurements of the morphological characteristics of CNT films, including shape, orientation, CNT diameter, and spacing between CNTs. The method reflects a locally averaged measurement that simultaneously samples from millions of CNTs while maintaining the necessary precision to resolve spatial morphological differences within a film. Using this technique we elucidate spatial variation in pristine films and study changes in the film structure as a result of mechanical manipulations such as uniaxial compression and capillarity-induced densification.

We study the rheological properties of blends formed from POSS and clay nanoparticles incorporated into PMMA in shear and extensional flow fields. Relevant morphological parameters, such as volume fraction, aspect ratio of the clay particles, and POSS miscibility are determined using wide angle X-ray scattering and transmission electron microscopy. The interdependence between melt rheology and morphology are understood within a theoretical framework for percolated physical networks, providing for comprehensive guidance regarding the performance and processing of POSS and clay based nanocomposites.

Thesis Supervisors: Professor Robert E. Cohen
                      St. Laurent Professor of Chemical Engineering

                      Professor Gareth H. McKinley
                      SoE Professor of Teaching Innovation in Mechanical Engineering

To Kim

ACKNOWLEDGEMENTS

---

[1] More evidence of awesomeness provided at the end of the acknowledgements section titled "Quantitative determination of metabolic processing power using linear regression of live human animal data"

who always had my best interest at hand, provided guidance when needed, and happily applauded my return to school; she did it all, everything that made her a fantastic advisor, mentor, and friend.

I am blessed with an incredible family. My parents, Kang and Edith, have never faltered in their unconditional love and support for everything that happened to pique my interest. They provided me with the luxury of educational opportunities and the freedom of choice. They gave me my first love of science and showed me why the world needs science concurrently with why science is completely about the world, but is not above it. My parents, David and Doreen, likewise have never stopped supporting, cheering, and inspiring me to be a better person every single day. My brothers and sisters, Gretchen, Alex, Jess, Evelyn, Lindsey, and Dave were always there in the tough times and the great, getting in and out of trouble. It is crazy to think that we are all, ahem, adults, buying houses, graduating, and awaiting the next exciting adventures that life has in store for us. And thank goodness for the D.O.L.E.A.C, Mr. Tibbins, and Mr. Wilson; the Maine Coons of my life. I can't say enough of what all of my family has meant to me as a person, and I will always cherish their love.

Finally, I dedicate this thesis to my wife, Kim, my greatest love. I could not have accomplished this without her love and support. The tough times in school were always mollified by the galvinizing look in her eyes, and the great times were infinitely more so while I shared them with her. I look forward to my life with you always.

ACKNOWLEDGEMENTS APPENDIX: Quantitative determination of metabolic processing power, or "awesomeness" using linear regression of live human animal data

Introduction

It is well known that drinking alcoholic beverages can result in some and any of the following results: an increased blood alcohol level, inebriation, wrecktimification, achieving a state of "lamination", or having a great time. There are drawbacks to consider in this methodology however. Some of the repercussions that can occur include: inebriation, hangovers, vomiting, caresses from pink kangaroos, using only their marsupial pouches (Such experiences can be found in the literature, most completely in "Mr.T don't want no Jibber Jabber", by T., Mr.) It is therefore important, to quantify a population's ability to achieve a certain blood alcohol level (BAC, latin *badius awesomus consumptionus*).

Experimental Conditions

Volunteers

We solicited volunteers consisting of 31 total participants, 11 females, 20 males.

Materials

The variety of alcoholic inputs ranged from Pabst Blue Ribbon to Napa Valley Chardonnays. The measurement device was a Department of Transportation certified Alcohawk device.

Potential Sources of Error [EDITOR'S NOTE]

In addition to the standard sources of error in these types of experiments (wait time before measurement, types/sizes of drinks, temporal spacing between drinks) the lack of control demonstrated by the researchers was clearly a factor of their own inebriation and should be controlled for in future experiments.

Results

97 total measurements were taken. Median number of drinks = 3. Max BAC achieved = 0.23. Average BAC achieved = 0.11.

The following chart is a summary of all data. An early stage predictive model was developed using linear regression. The model currently only factors in the gender of the subject. The bold lines represent the best fit for both males and females, with the accompanying dashed lines representing 95% confidence intervals. The green line, while a form of transportation found in Boston, MA, is actually the line of no-transportation (i.e. if you are above this line, do NOT drive).
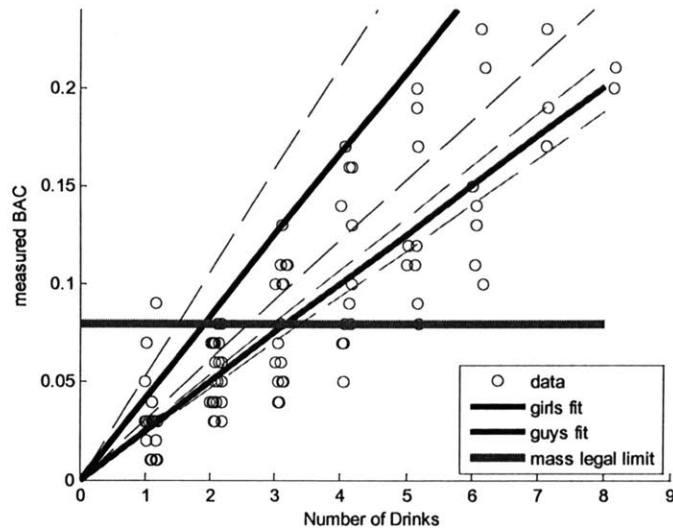
Averaging across all data points, given a specified number of drinks you would get a much better fit for the entire population as shown below, with associated error bars.

$$y = 0.0257x + 0.0049$$
$$R^2 = 0.9895$$
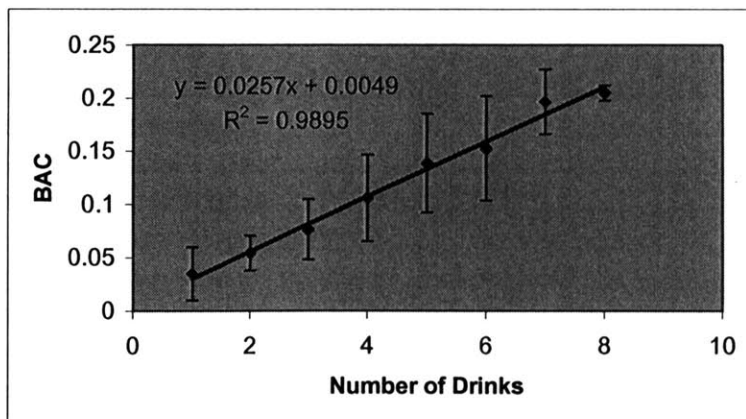
Conclusions and Future Work

The experiment was a success in that the subpopulation of North Eastern US residents (MIT and Harvard) demonstrated a high ability to consume ethanol to "double digit" levels. Further experiments will have to be run to address issues of experimental error. We look forward to soliciting more volunteers to partake in another study.

TABLE OF CONTENTS

LIST OF FIGURES

14

LIST OF TABLES

1. INTRODUCTION

1.1. Overview of hierarchically nanostructured materials

Novel nanostructured materials have attracted broad interest from scientists and engineers across many disciplines. The use of nanostructured materials, materials with relevant length scales on the order of 1 – 100 nm, promises to spawn enhancements in mechanical, electrical, thermal, and surface properties. Despite significant advances in the fundamental understanding, synthesis and processing of these materials, commercial realization of these improvements remain elusive. This is largely due the inability to identify and control the relevant parameters which govern the underlying morphology. Further understanding of the relationships between structure and resultant property is required to bridge the gap between lab-scale research and functional applications.

There are two design paradigms towards the fabrication of nanostructured materials: "top-down" and "bottom-up". The "top-down" approach has been adopted by the microelectronics and semiconductor industries, where a structure is carved and sculpted from a monolithic substrate, such as a silicon wafer. After numerous masking, patterning and dissolution steps, the remaining feature becomes an integrated building block for complex fluidic or electronic devices. This method is advantageous because of the parallel nature of fabrication; several devices can typically be made from one initial substrate. The difficulties inherent in this approach include the costs and development of smaller and more robust "nano-shovels", or masking and patterning technologies. The "bottom-up" approach, which takes advantage of so-called "self-assembly", relies on the thermodynamic and kinetic interactions between atomically distinct materials to form energetically favorable, stable, geometric shapes (Ikkala and ten Brinke 2002; Whitesides and Grzybowski 2002). Typical examples include micro-phase separation in block copolymers (Bates *et al.* 1982; Register 2003), electrostatic interactions between polyelectrolytes (Nolte *et al.* 2004), or hydrogen bonding in colloidal multilayers (Lee *et al.* 2005).

Hierarchically nano-structured materials are those which exhibit order on at least two characteristic length scales, one of which is on the nanometer scale. Essentially the hierarchical structure arises from the superposition of a typically larger length scale over an integrated nanoscale material (see Figure 1-1). The fabrication of the hierarchical structures usually takes advantage of both of the above-mentioned design approaches. Block copolymer thin films and polyelectrolyte multilayers have been templated by microcontact printing with PDMS molds (molds are made from a "top-down" masking procedure) providing micron-scale localization of a nano-structured film for applications in cell arrays (Kim *et al.* 2006) or carbon nanotube (CNT) growth (Bennett *et al.* 2006). Nano-reactor chemistry, utilizing functional chemical groups to perform *in situ* re-dox reactions, has been used to localize silver nanodots into polyelectrolyte multilayers, providing a change in refractive indices for optical Bragg (Wang *et al.* 2002) and Rugate filters (Nolte *et al.* 2004). Utilizing the native immiscibility between polymer pairs in multilayer coextrusion processes can give rise to new materials with significantly different barrier properties (Mueller *et al.* 2000), optical characteristics (Weber *et al.* 2000; Tangirala *et al.* 2004), electrical conductivity (Nazarenko *et al.* 1999) and glass transition temperatures (T_g) (Liu *et al.* 2003; Liu *et al.* 2004; Liu *et al.* 2006). The introduction of additional length scales potentially provides significant advantages in function and flexibility. However, these benefits are typically accompanied by augmented complexity in the morphology and corresponding processing requirements. Accordingly the development and improvement of techniques which yield quantitative characterization of the morphology of nanostructured materials continues to be an active area of research.

A straightforward method for designing nanoscale material is to blend a nanoparticle into a polymeric matrix. Nanoparticles typically have large surface area to volume ratios which can give rise to large observable enhancements in material performance at low loadings (Moniruzzaman and Winey 2006). Typical nanoparticles can take on several geometric forms and can often possess a broad range of aspect ratios. These materials range from carbon nanotubes (CNTs) to exfoliated clay to silica polyhedral oligomeric silsesquioxane (POSS) cages, representing the geometric forms of lines, planes and points, respectively. Nanoparticle incorporation into a polymeric matrix is typically accomplished by random mixing using mechanical forces (twin-screw extrusion) or solution blending(Schaefer *et al.* 2003; Tanoue *et al.*

2004; Brown *et al.* 2005). However, the relative strength of filler-filler interaction compared to filler-matrix interactions determines the underlying morphology of the composite, including dispersion or flocculation and aggregation of particles. In fact, due to the same large surface area to volume ratio that gives rise to the improvement in material properties, it has been shown that very small amounts of POSS can be added to PMMA before aggregation occurs (Kopesky *et al.* 2004). Because these large changes in structure can change with small changes in loading, investigations of the performance and processing of these materials using these fillers will rely on accurate characterizations of the morphology and the rheology of these nanoparticle based systems.
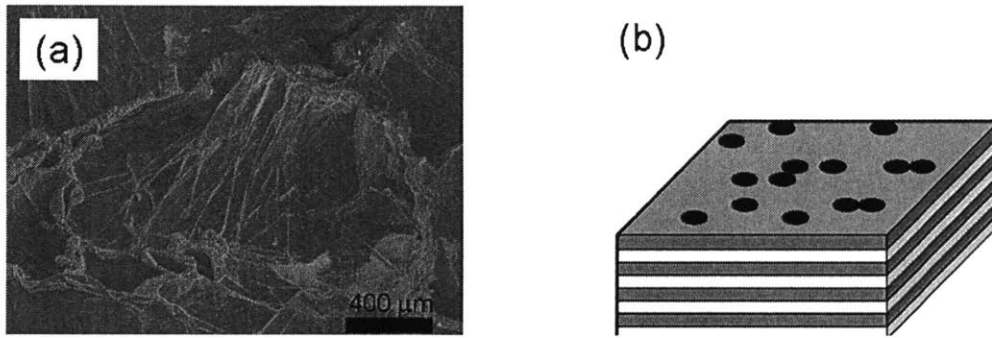
Figure 1-1. Examples of hierarchically nano-structured materials. (a) Carbon nanotube (CNT) cellular foams created from vertically aligned CNT films are formed from nanometer scale CNTs but are bundled together into micron scale features (b) Schematic of composite film formed by multilayer coextrusion of two polymers with clay platelets confined to alternating grey layers

1.2. Nanoparticles: dots, rods, and plates

The focus of this thesis will be on the morphological and rheological characterization of hierarchically nanostructured materials based on three specific types of nanoparticles: (1) multiwall carbon nanotubes (MWCNTs), (2) clay sheets, and (3) polyhedral oligomeric silsesquioxane (POSS) silica-cages (see Figure 1-2). All of these systems can either possess an inherent hierarchical structure or be incorporated into a larger polymeric one through fabrication processes such as multilayer coextrusion (Schrenk and Alfrey Jr. 1978; Alfrey Jr. and Schrenk 1980), *in situ* polymerization or cross-linking in a low viscosity polymer (Garcia *et al.* 2007), or

polymer stamping (Bennett *et al.* 2006). The three particles were chosen because they represent three distinct "nano-dimensions" and geometric shapes. POSS is nanoscopic in all dimensions, a so-called zero dimensional particle, "0-D", because it has zero length scales greater than the nanometer scale. CNTs are "1-D" because the CNT lengths are typically tens of microns to several millimeters while the radial dimension is typically ~ 3 - 30 nm. Clay sheets, when they are exfoliated, are "2-D" because only the thickness of the plate is on the order of a nanometer whereas the length and width typically 100 – 1000 nm. Thus these three nanoparticles are reasonable physical representations of the aforementioned point, line, and plane which can provide for an experimental correspondence with previously developed theoretical predictions of structure-property relationships based on geometric shapes.
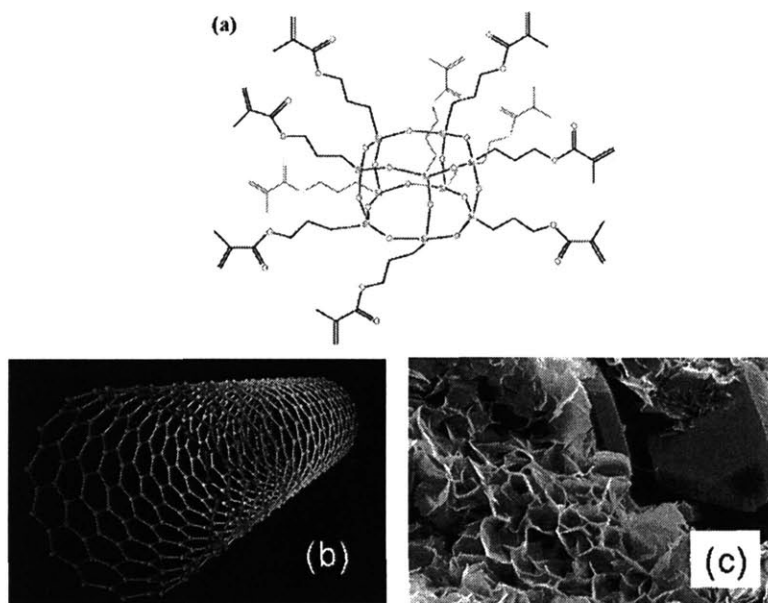
Figure 1-2. Nanoparticles used in this thesis: (a) an illustration of "0-D" POSS ten-cornered cage structured, functionalized with methoxypropyl methacrylate group (image from Kopesky *et al.* (Kopesky *et al.* 2005)), (b) molecular simulation representation of a "1-D" singlewall CNT (image from http://www.wikipedia.org), and (c) SEM micrograph of native "2-D" montmorillonite clay (image from http://www.webmineral.com).

1.2.1. "0-D" POSS

POSS nanoparticles are hybrid organo-silica cages, with the chemical composition $R_xSi_xO_{1.5x}$. The R- groups can be decorated with a variety of functional groups at the Si corners. A ten-cornered cage with methoxypropyl-methacrylate groups is shown in Figure 1-2a. A diverse library of R- groups has been developed, allowing the interactions between POSS particles and a surrounding matrix to be tailored to the user's desires (Kopesky *et al.* 2005; Bizet *et al.* 2006). The R- groups can also be used for chemistry. Several groups have incorporated POSS into a polymeric backbone as a copolymer (Kim *et al.* 2002; Turri and Levi 2005). Because POSS is flexibly combined with macromolecular materials, the resulting nanocomposite is an ideal one for applications in plasticizing polymers, improvement in thermal characteristics, and enhancement in mechanical toughness (Liu and Zheng 2005; Kopesky *et al.* 2006; Soong *et al.* 2006; Ciolacu *et al.* 2007). A significant amount of research has been performed on the morphological and rheological characterization composites based on various POSS molecules (Romo-Uribe *et al.* 1998; Kopesky *et al.* 2004; Joshi *et al.* 2005; Kim and Mather 2006; Kopesky *et al.* 2006).

1.2.2. "1-D" Carbon Nanotubes (CNTs)

CNTs are graphitic tubes of pure carbon. The molecular simulation representation of a single walled CNT is shown in Figure 1-2b. In certain pure forms they possess ultrahigh conductivity, thermal conductivity and mechanical strength making them useful for practically any application (Baughman *et al.* 2002; Snow *et al.* 2003; Cao *et al.* 2005). However growth and production yield of CNTs remains costly and high purity material is rare. Dispersion is a significant challenge as strong van der Waals forces between adjacent CNTs are difficult to overcome. Despite the challenges of working with CNTs, there have been significant efforts to create stand-alone applications out of CNTs (Kymakis and Amaratunga 2002; Rouse and Lillehei 2003; Artyukhin *et al.* 2006) as well as incorporate them as fillers into polymers or other hierarchical structures (Chen *et al.* 2006; Hernandez *et al.* 2006; Moniruzzaman and Winey 2006). Furthermore the recent advances in thermal CVD of dense millimeter long CNT films

have provided an avenue for macroscopic scale up of production (Futaba *et al.* 2006; Hart and Slocum 2006).

1.2.3. "2-D" Clay

Clay is the generic name for a class of layered silicates that are both found naturally or synthesized. They have already found their way into commercial industrial applications as a toughening agent. The native morphology of clay is an aggregate, a lamellae typically 10 – 1000 nm in width and length and consisting of many individual platelets ~1 nm in thickness and separated by ~1 nm as shown in Figure 1-3. In addition to van der Waals forces which prevent dispersion of the individual platelets, electrostatic interactions enhance flocculation. Most research efforts in improving clay-polymer nanocomposite properties have been focused on achieving an exfoliated morphology, where few tactoids are observed (Manias *et al.* 2001). This is typically accomplished by the introduction of small molecule swelling agents, *in situ* polymerization of the matrix, or the use of mechanical energy to force the platelets apart.
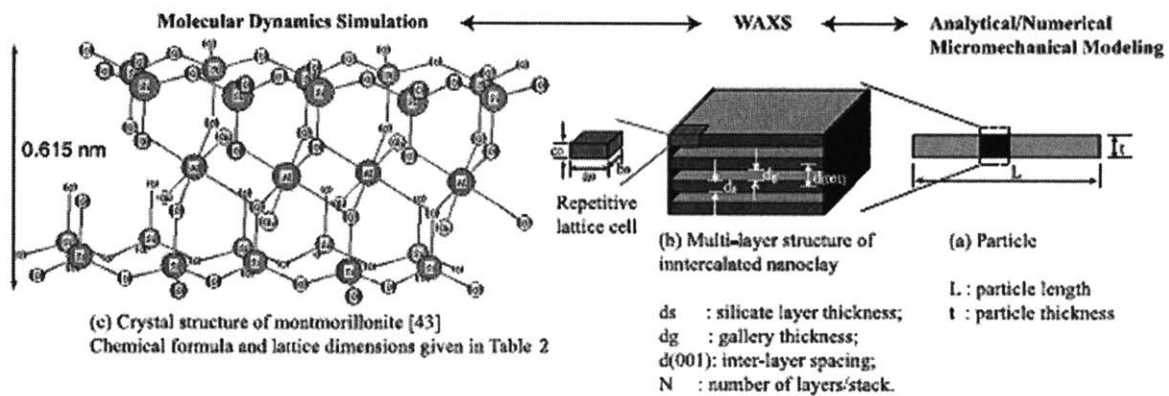
Figure 1-3. Illustration of clay morphology modified from (Sheng *et al.* 2004).

1.3. Morphological and rheological characterization

1.3.1. Electron Microscopy

Standard morphological characterization of nanostructured materials include direct visualization techniques such as electron microscopy, atomic force microscopy, and optical microscopy as well as indirect methods such light, neutron, and x-ray scattering, and thermal characterization. Electron microscopy is a ubiquitous and robust method which can image nanometer scale dimensions with angstrom resolution (high resolution transmission electron microscopy [HRTEM]) up to length scales of several hundred microns (in scanning electron microscopy [SEM]). Despite the optimal size range of the techniques for studying hierarchically nano-structured materials, there are several short comings. Electron density can be low, especially for polymeric systems, yielding low contrast images, necessitating staining of the films and making it challenging to measure dimensions quantitatively (Bates *et al.* 1982). Electron microscopy, especially HRTEM is, by definition, a local measurement; it is tedious, requiring the analysis of multiple micrographs which does not guarantee statistical validity. Furthermore the necessity of microtoming can cause unintended mechanical interference with the native morphology. It can be challenging to resolve feature sizes less than 100 nm using SEM. Overall however, electron microscopy has been shown to be invaluable at determining the miscibility limits for POSS-filled PMMA (Kopesky *et al.* 2004; Kopesky *et al.* 2005) and PVC (Soong *et al.* 2006), measuring orientation in clay filled polypropylene (PP) foams (Okamoto *et al.* 2001), and illustrating the complex structures of CNT cellular foams (Chakrapani *et al.* 2004).

1.3.2. X-ray scattering

Scattering methods are indirect techniques that provide the Fourier transform of real-space information. The difference between the methods of light, neutron, and x-ray scattering is the range of accessible length scales (though contrast can be optimized for a specific system), while the essential physics of scattering radiation remains the same. For simplicity, and because it will be a focal point for this research, we discuss only X-ray scattering. X-ray scattering is an average technique which samples over a large population of nanoscale materials in a sample.

26

The beam spot is typically hundreds of microns in diameter; thus the data can reflect information for a large number of scattering events from nanoscopic materials.

The dimensional information obtained from a full range for small-angle X-ray scattering (SAXS) is ~ 100 nm – 1 nm and for wide-angle x-ray scattering (WAXS) is 10 nm – 0.5 nm. Larger length scales can be accessed using ultra SAXS (USAXS) with resolution up to the micron scale. A representative scattering curve for polyethylene (Lupolen 1840H, BASF) in both SAXS and WAXS is shown in Figure 1-4. Because of the wide range of length scales which can be probed using x-ray scattering, both SAXS and WAXS have been widely used in investigating nanoparticle filled systems, including POSS, CNTs, and clay.

WAXS patterns of POSS molecules in a polymeric matrix have been used to provide information about the lattice spacing between aggregated POSS molecules through Bragg's Law:
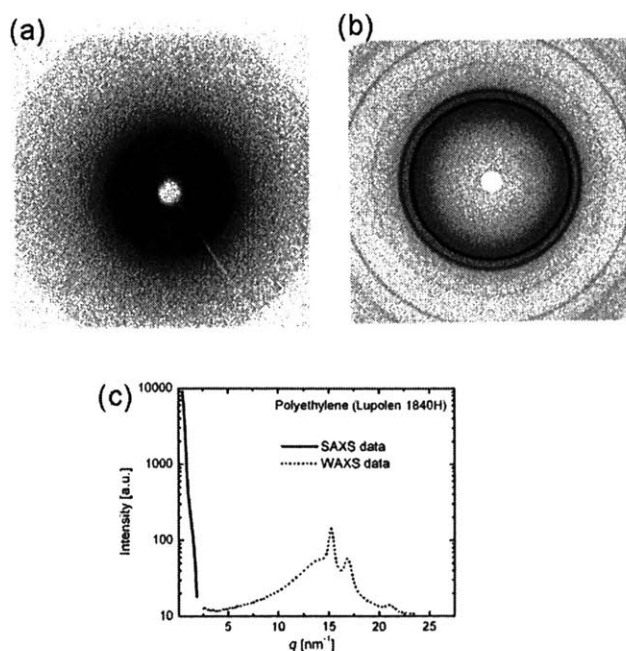
Figure 1-4. X-ray scattering from polyethylene (Lupolen 1840H, BASF) with (a) 2-D SAXS and (b) 2-D WAXS patterns taken simultaneously. (c) Combined scattering curves obtained from 2-D patterns.

$$d = \frac{\lambda}{2\sin\theta} \qquad\qquad (1\text{-}1)$$

where λ is the wavelength of X-rays, d is the lattice spacing, and θ is one-half of the scattering angle. Average tactoid or crystallite domain sizes can be estimated from the breadth of the Bragg reflection using the Scherrer equation:

$$t = \frac{\lambda}{B\cos\theta} \qquad\qquad (1\text{-}2)$$

where t is the thickness of the crystallite and B is the full-width at half-max of the Bragg reflection. The lack of a peak suggests a homogeneous and random dispersion of POSS in a polymeric matrix and a sharp peak is suggestive of a large domain of aligned crystallographic planes.

WAXS is an appropriate method for studying the morphology of POSS molecules in a polymeric matrix, as the individual cages tend to be small (~1 nm). In addition they are roughly isotropic in shape, with an aspect ratio of unity. CNTs and clay platelets are typically much larger with the nano-dimension ranging from ~ 1 – 50 nm and the long dimensions ranging from 50 nm to 2 mm, giving rise to large aspect ratios. Because of the anisotropy in dimensions, it is useful to provide a quantitative assessment of the alignment of the particles. This can be obtained from a two-dimensional x-ray scattering pattern through orientation parameters:

$$f = \frac{1}{2}\left(3\langle\cos^2\phi\rangle - 1\right) \qquad\qquad (1\text{-}3)$$

where f is the Hermans orientation parameter (with limiting values of 1, 0, -1/2 to indicate vertically aligned, randomly oriented, and horizontally aligned, respectively) and $\langle\cos^2\phi\rangle$ is the mean-square cosine of the azimuthal angle, calculated from:

$$\left\langle \cos^2 \phi \right\rangle = \frac{\int\limits_0^{\pi/2} I(\phi)\sin\phi\cos^2\phi\, d\phi}{\int\limits_0^{\pi/2} I(\phi)\sin\phi\, d\phi} \qquad (1\text{-}4)$$

where ϕ is the azimuthal angle and $I(\phi)$ is the x-ray intensity at a specified value of ϕ.

WAXS has been used to characterize the extent of dispersion, intercalation, or exfoliation in CNT bundles or clay tactoids by measuring separation between particles when the distances are small (Jeon et al. 2004; Prasad et al. 2004). SAXS has the advantage of providing a larger length scale measure of separation as a counterpart to the information obtained from WAXS. In addition very low angle features in SAXS curves can correspond to a measurement of the size of particles. In general SAXS intensity curves can be interpreted through the combination of experimental considerations and intra- and inter-particle interference of scattered x-rays. This combination can be expressed as:

$$I(q) = AF(q)S(q) \qquad (1\text{-}5)$$

where q is the scattering vector where $q = 4\pi\sin\theta/\lambda$, A is a constant that accounts for the experimental details, $F(q)$ is the form-factor which is the contribution from single-particle scattering and $S(q)$ is the structure factor which corresponds to the interference of scattered x-rays from multiple particles.

For dilute particulate systems, low angle scattering contains dimensional information as stated by Guinier's Law (Guinier and Fournet 1955; Brady 2003):

$$I(q) = N(\Delta\rho)^2 \nu^2 \exp\left(\frac{-q^2 R_g^2}{3}\right) \qquad (1\text{-}6)$$

where N is the number of particles in the scattering volume, $\Delta\rho$ is the difference in electron scattering densities, ν is the volume of the particles, and R_g is the radius of gyration of the particles. The constants in front of the exponential term provide only a vertical shift in the log-

log plot of *I(q)* vs. *q*. Thus the decay in *I(q)* provides information about R_g. For a given *a priori* assumption of the shape of the particle (sphere, rod, platelet), it is straightforward to calculate the geometric dimensions of the particle.

1.4. Rheology

Traditional rheological characterization is used primarily to measure material functions, such as steady shear and extensional viscosities which are relevant to the optimization of processing conditions. Understanding the behavior of complex fluids in these flow-fields can be important for controlling the processing steps required for fabricating complex hierarchically nanostructured materials. In addition rheology has been shown to be an extremely sensitive measure of underlying structure and provides another complementary method for quantitative evaluation of morphological characteristics. For polymeric systems there are many commercial instruments that can provide this information.

However similar to X-ray scattering, rheology is an inverse technique and requires an assumption about the behavior of the material through constitutive equations. Rheological measurements of hierarchically nanostructured materials can often give rise to unexpected rheological behavior, requiring some knowledge of the underlying morphology. It has been shown that immiscibility between polymer pairs gives rise to decreased chain entanglement at the interface (Helfand and Tagami 1972; Helfand and Sapse 1975; Furakawa 1989; Goveas and Fredrickson 1998). For shear flow in coextruded multilayers this manifests as an apparent slip or a bulk reduction of viscosity, as increasing volume of less-entangled interphase are formed (Zhao and Macosko 2002; Adhikari and Goveas 2004). This gives rise to measured viscosities which violate the log additive rule which hold for typical blends of polymers:

$$\log \eta_{\text{mixture}} = \phi_a \log \eta_a + \phi_b \log \eta_b \qquad (1\text{-}7)$$

where $\eta_{i=mixture,a,b}$ is the shear viscosity of mixture, polymer a, or polymer b, and $\phi_{i=a,b}$ are the volume fractions. In extensional flows, coextruded multilayers of immiscible polymer pairs exhibit interfacial tension driven strain hardening and enhancement in the transient stress growth

30

function (Levitt and Macosko 1997). The generation of additional interface requires additional energy which is input in the form of mechanical work. Theoretical treatments of the effect of interfacial tension on the linear viscoelastic properties was summarized in the Palierne model, which incorporates interfacial tension into a constitutive equation for blends of immiscible polymers in the low strain limit (Palierne 1990; Graebling et al. 1993; Delaby et al. 1995). The hallmark of a strong contribution from the interface is the appearance of a plateau in G' in small amplitude oscillatory shear (SAOS) which extends into the terminal region due to the long relaxation time of droplets returning to their equilibrium spherical shape. Again this provides evidence that rheological characterization of structured blends of polymers provides a sensitive measurement of the underlying morphological properties, including the amount of interface that exists within a blend. A more detailed discussion on the interplay between rheology, interfacial tension, and morphology of immiscible polymer blends is included in Appendix 10.1.

The incorporation of nanoscale fillers can also give rise to convoluted rheological measurements, including both plasticization (a decrease in material functions) and reinforcement (an enhancement in material functions). The outcome largely depends on the relative interactions between particles and the polymeric matrix. Kopesky et al. (2005) demonstrated that the addition of methacryl-POSS to PMMA increases the free volume of the chains and corresponds to a decrease in material functions. However they also indicate that the copolymerization of POSS with PMMA, followed by subsequent incorporation of free POSS into the copolymer gives rise to substantial enhancement in material functions which arise from the "sticky" or inhibited reptation of the chains (Kopesky et al. 2004).

In addition to the experimental and theoretical examinations of spherical or isotropic fillers in polymeric matrices, there is a significant amount of theoretical literature which describes the rheological behavior of high aspect ratio fillers. High aspect ratio fillers differ significantly from isotropic particles in that they begin to interact with each other at much lower volume fractions. This is easily demonstrated in comparing the predicted shear modulus, G, from the Guth-Smallwood equation for hard spheres (Equation 1-8) to the Guth-Gold equation for rods (Equation 1-9) in Figure 1-5.

$$G(\phi) = G_{\phi=0}\left[1 + 2.5\phi + 14.1\phi^2\right] \tag{1-8}$$

$$G(\phi) = G_{\phi=0}\left[1 + 0.67p\phi + 1.62p^2\phi^2\right] \tag{1-9}$$

where p is the aspect ratio and ϕ is the volume fraction. It is clear that even at a moderate aspect ratio of $p = 10$, the difference is substantial. It is expected for many nanoparticle systems, such as CNTs, aspect ratios range from $10 - 1000$.

The large enhancement which is observed in material functions for high aspect ratio fillers compared to isotropic materials originates from the ability for particles to interact at much lower volume fractions. For example rods or platelets which are translated in a shear flow undergo a time-periodic rotation called a Jeffrey orbit (Larson 1999):

$$\tan\theta = p\tan\left(\frac{\dot{\gamma}t}{p+1/p}\right) + \tan\theta_0 \tag{1-10}$$

where θ is the angle formed by the axis of symmetry with the flow direction, p is the aspect ratio, $\dot{\gamma}$ is the shear rate, and θ_0 is the initial orientation of the particle at time = 0. The rotation results in a hydrodynamic volume for the particle which is larger than the actual material volume. Therefore the overlap concentration, c^*, the concentration at which solutions transition from dilute and non-interacting to a concentrated, for rods to a concentrated regime is typically less than that for spheres, or:

$$c^*_{rods} \sim \frac{1}{L^3} \quad < \quad c^*_{spheres} \sim \frac{1}{r^3} \tag{1-11}$$

where L is the rod-length and r is the sphere radius.
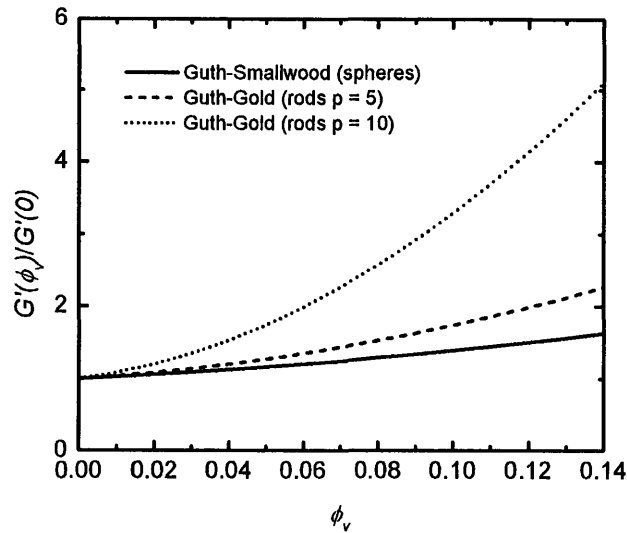
Figure 1-5. Comparison between Guth-Smallwood equation for hard sphere fillers vs. Guth-Gold equation for rod fillers. The high aspect ratio of rod fillers contributes to a larger enhancement in modulus at lower volume fractions.

For nanoparticles in a fluid, deviation from the Jeffrey orbit for a particle can be caused by the stronger effect of Brownian motion. In the case for non-interacting particles (i.e. low volume fractions), relaxation occurs through rotational diffusion of the particles until the particles are essentially random. The time scale over which this process occurs is given by:

$$\tau = \frac{1}{6D_{r0}}$$ (1-12)

where D_{r0} dilute solution rotational diffusivity. Several expressions for D_{r0} for different spheroids are given in Table 1-1 which can be related to viscometric properties of the fluid (Larson 1999).

Table 1-1. Dilute solution rotational diffusivities for spheroids. (Larson 1999)

Spheroid (p = aspect ratio)	Rotational Diffusivity (D_{r0})
Sphere (p=1)	$D_{r0} = \dfrac{k_B T}{\pi \eta_s d^3}$
disk (p << 1)	$D_{r0} = \dfrac{3 k_B T}{4 \eta_s d^3}$
rod (p >> 1)	$D_{r0} = \dfrac{3 k_B T \left[\ln(L/d) - 0.8 \right]}{\pi \eta_s L^3}$
spheroid (p > 1)	$D_{r0} = \dfrac{3 k_B T \left[\ln(2p) - 0.5 \right]}{\pi \eta_s L^3}$

As increasing amounts of filler are loaded into the matrix, the number of interactions that a particle has with neighboring particles increases correspondingly. Beyond a critical volume fraction a self-similar physical network can form which spans length scales much larger than the hydrodynamic radius of the particles. The volume fraction at which this occurs is called the percolation threshold, ϕ_c, and network is called a percolated network. Near ϕ_c, material functions related to the elasticity of the solid-like network, such as the storage modulus, by analogy with conductance (Garboczi *et al.* 1995; Jones 2002) have critical-like behavior described by:

$$G' \sim \left(\phi - \phi_c \right)^\mu \qquad (1-13)$$

where μ is the fractal exponent of the power-law behavior. It has been suggested that a larger magnitude of μ corresponds to greater interactions between particles. For particles with high aspect ratios, Monte Carlo simulations have shown that percolation is achieved at much lower volume fractions for rods and platelets than for spheres (Garboczi *et al.* 1995). For the typical aspect ratios for CNTs and clay platelets, $\phi_c \sim 0.01$ whereas for spheres $\phi_c \sim 0.3$.

1.5. Thesis objectives and method of approach

The objective of this thesis is to develop and demonstrate novel rheological and morphological characterizations for three different nanostructured materials: MWCNT films, POSS blended with PMMA and clay-filled PMMA. For MWCNT films we are specifically interested in developing an X-ray scattering technique that would provide quantitative measurements of morphological characteristics as a counterpart to electron microscopy. For the POSS-PMMA system we are specifically interested in examining the extensional rheology of the blend. For the clay-filled PMMA system we are interested in using rheology and morphological techniques to experimentally link the underlying structure of the different clay nanocomposites to the macroscopic melt behavior.

Chapter two describes how a novel extensional rheology fixture, the SERUTP (Sentmanat 2003; Sentmanat 2003; Sentmanat 2004), performed against various historical "gold-standard" elongational rheological measurements of polyethylene (PE). The device is focal point for the studies in chapters five and six. In this chapter we demonstrate how several types of extensional experiments can be performed on the SERUTP including transient stress-growth, creep and relaxation following step-strain in a uniaxial flow-field. We illustrate how the results from the SERUTP matched well with standard techniques on other traditional melt extensional rheometers. Using the SERUTP fixture, we experimentally illustrate that stability of uniaxial extensional flow of PE can be explained within the context of the Considere criterion.

Chapter three describes the development of a SAXS methodology for studying the morphology of MWCNT films, which provides quantitative measurements of the orientation and tube diameters. We determine, using two different catalyst substrates, that orientation can range from random to strongly vertically aligned in as-grown, pristine CNT films. We use a model, which employed the hard cylinder form factor for SAXS intensities, to measure CNT diameters that corresponded well with measurements from HRTEM. By scanning across the vertical dimension of the film we illustrate the presence of a spatial variation in both alignment and CNT diameter through the thickness of the film. Alignment is highest in the middle of the film and

CNT diameters increase with distance from the substrate which allows us to infer that the catalyst activity changes over the course of CNT growth.

Chapter four describes the extension of the SAXS methodology introduced in chapter three, by providing evidence for additional spatial variation in the CNT diameter originating from differences in the catalyst near the edge versus the interior of the substrate. Utilizing the combined analysis from chapters three and four, we provide a qualitative morphological map for MWCNT films. We then proceed to examine the effect of uniaxial compression on the CNT films and confirm that the orientational changes observed in the SAXS patterns correspond to a buckling response exhibited by the CNTs, validated by SEM. We also use capillarity induced densification of the film to create a cellular foam which exhibits a complex structure of dense ridges and horizontally aligned valleys. Examining the vertically resolved SAXS curves we observe an increase in intensity at low scattering angle, q, which corresponds to increased packing density of CNTs. Using *in situ* SAXS, we confirm this with time-resolved SAXS curves and indicate, using a model based on structure factor, that SAXS intensities can provide an estimate of the areal density of CNTs.

Chapter five describes the use of the SERUTP to characterize the extensional rheology of PMMA filled with methacryl-POSS (mPOSS). We examine the extensional rheology of blends of mPOSS with two different molecular weight PMMAs. For the case of a uniform dispersion of mPOSS in the PMMA matrix, we demonstrate that data from low-strain rate transient uniaxial extension matches well with linear viscoelastic (LV) data and high-strain data at high Deborah numbers give rise to plasticization of the PMMA matrix. For blends beyond the mPOSS-PMMA miscibility limit, the presence of a percolated network of phase-separated mPOSS gives rise to a large enhancement in the extensional viscosity of the blends, significantly larger than expected from LV data. Stress relaxation following cessation of extension experiments demonstrate accelerated relaxation of stress in PMMA due to the presence of mPOSS, and a long relaxation time plateau due to the presence of the secondary mPOSS-rich phase. We use WAXS in attempts to determine changes in the morphology and miscibility of mPOSS in PMMA during extension, but the results were inconclusive.

Chapter six describes a fundamental rheological study of clay-filled PMMA nanocomposites formed by emulsion polymerization. We determine the geometric dimensions and morphological properties of two different clay particles using WAXS and TEM. We employ a formalism, previously developed by Sheng *et al.*, to convert weight percentages into morphologically dependent volume fractions. We measure the linear viscoelastic behavior of the clay-filled PMMA. We demonstrate that for flows at De << 1 a percolated network theory for rods could quantitatively explain the enhancement in G' as a function of aspect ratio and volume fraction. For flows with De >> 1, the classic Guth-Gold filler theory provides a comparable guide. We then measure the extensional rheology of the nanocomposites, using the SERUTP, and demonstrate that the enhancement of extensional viscosities due to the presence of clay filler corresponds well to Batchelor's theory for elongated rods. Relaxation of stress following cessation of extension indicates a retarded relaxation with increased loading of clay.

Chapter seven summarizes the major thesis contributions and conclusions and chapter eight provides possible future directions for the continuation of this research.

2. MEASURING THE TRANSIENT EXTENSIONAL RHEOLOGY OF POLYETHYLENE MELTS USING THE SER UNIVERSAL TESTING PLATFORM

(portions of this chapter were published in the Journal of Rheology by M.L. Sentmanat, B.N. Wang, G.H. McKinley, 2005)

We use a new extensional rheology test fixture that has been developed for conventional torsional rheometers to measure the transient extensional stress growth in a number of different molten polyethylene samples including a linear low density polyethylene (Dow Affinity PL 1880), a low density polyethylene (Lupolen 1840H), and an ultrahigh molecular weight polyethylene (UHMWPE). The transient uniaxial extensional viscosity functions for the linear low density polyethylene (LLDPE) and low density polyethylene (LDPE) samples have both been reported previously in the literature using well-established instruments and this allows us to benchmark the performance of the new test fixture. Transient stress growth experiments are carried out over a range of Hencky strain rates from 0.003 to 30 s^{-1} and the data show excellent agreement with the published material functions. At deformation rates greater than 0.3 s^{-1} a true steady state extensional viscosity is not obtained in the LDPE samples due to the onset of necking failure in the elongating strips of polymer; however, the limiting values of the transient extensional viscosity at the onset of sample failure agree well with previously published values for the steady state extensional viscosity. This apparent steady-state extensional viscosity first increases with deformation rate before ultimately decreasing as approximately $\dot{\varepsilon}^{-0.5}$. In addition we perform extensional step-strain measurements at small Hencky strains and demonstrate good agreement with the relaxation modulus obtained from shear rheometry. Extensional creep measurements are performed over a range of constant imposed tensile stresses and also agree well with the measured shear creep compliance. Finally, tensile stress relaxation experiments are carried out after a range of imposed Hencky strains. These tests demonstrate that following large extensional deformations the tensile stresses relax nonlinearly and also that, beyond a critical strain, the material is unstable to viscoelastic necking and rupture. Additional transient extensional stress growth measurements using highly entangled linear UHMWPE samples show

greatly reduced strains to failure, that are in agreement with the predictions of the Considere theory.

2.1. Introduction

Measurement of the transient uniaxial extensional viscosity for a polymeric material remains a technical challenge. The situation has been somewhat alleviated in recent years by the development of commercial instrument designs such as the RME (Meissner and Hostettler 1994); however, even when a single common instrument is available, careful documentation and control of the test protocols and sample preparation is essential to avoid systematic deviations in results obtained using a single polymeric sample (Schulze et al. 2001). Many of these experimental difficulties are described in an early review article (Meissner 1985) and in the work of (Schweizer 2000). A recurring theme and important feature of the advances in extensional rheometry over the past 30 years has been the emphasis on well-controlled, widely distributed test materials and round-robin interlaboratory comparisons of different instrumental techniques and operating conditions. This was a hallmark of the early work on the IUPAC-A low density polyethylene by Laun, Münstedt and Meissner using stress-controlled and rate-controlled instruments of widely differing design (Laun and Munstedt 1979). This IUPAC material became an international standard reference material which could be used to validate the dynamical response of new rheometer designs and to which other materials could then be compared (Munstedt and Laun 1979; Munstedt and Laun 1981). Early attempts at repeating this success in extensional rheometry of polymer solutions using the polyisobutylene-based M1 test fluid (Sridhar 1990) were met with disappointment (James and Walters 1993). However, the wide scatter in these measurements arose because of the strong strain-rate and strain sensitivity of the extensional stresses exhibited in polymer solutions and the widely disparate design of the instruments which resulted in nonhomogeneous kinematics. More recent interlaboratory comparisons using a series of well-characterized dilute polystyrene solutions and a common design of filament stretching rheometer, have shown very good agreement (Anna et al. 2001). The test instruments that were involved in this study were of similar overall design to the original Münstedt tensile rheometer (Munstedt 1979); however, because of the increased importance of

gravity, surface tension, and inertia, special design considerations must be incorporated (McKinley and Sridhar 2002). A filament stretching rheometer also been used recently to characterize the transient extensional response of polyethylene melts that are closely related to those we investigate in the present study (Bach *et al.* 2003).

In the present work we seek to evaluate the performance of a new test fixture, known as the SER, developed for elongational rheometry by Sentmanat (Sentmanat 2003; Sentmanat 2003). The instrument employs the fiber windup technique first described by Macosko and Lorntson (Macosko and Lorntson 1973) in which a rotating fixture is mounted on the transducer of a conventional torsional rheometer. Further analysis of the kinematics and enhancements to this basic configuration were described by Connelly and co-workers (Connelly *et al.* 1979; Pearson and Connelly 1982) and Padmanbhan *et al.* (Padmanabhan *et al.* 1996). However, a limitation encountered in all of these previous studies was the onset of nonuniform stretching at moderate strains due to the no-slip boundary condition acting at the rigid (nonrotating) clamped end of the sample. In the SER fixture, this problem is circumvented by the use of a pair of counter-rotating rollers. Extensive experimental details of the instrument design and its dynamical range are provided in a recent publication (Sentmanat 2004); however, measurements from the instrument have not, until now, been benchmarked against existing data for a standard viscoelastic reference material. The original IUPAC A material is no longer a viable benchmark material due to irreversible aging over the past 30 years (Laun 2003). However, another low density polyethylene (BASF Lupolen 1840H) has recently been shown to exhibit a very similar response in extensional flow (Munstedt *et al.* 1998). A closely related grade (Lupolen 1810H) containing an anti-oxidant stabilizer package and possessing slightly higher zero-shear-rate viscosity has also been characterized in detail by Hachmann (Hachmann and Meissner 2003) and by Bach *et al.* (Bach *et al.* 2003). The rheological properties for this latter grade have also been fitted to a multimode model appropriate for branched materials by Verbeeten *et al.*(Verbeeten *et al.* 2001). In order to avoid any rheological influences of the stabilizer package, and on the recommendation of Laun (Laun 2003), we have focused in the present work on the unstabilized Lupolen 1840H grade studied by Münstedt and co-workers (Gabriel *et al.* 1998; Munstedt *et al.* 1998).

It is well known that low density polyethylene samples exhibit pronounced strain hardening in transient uniaxial elongation and this can minimize the consequences of kinematic nonhomogeneities in fiber-windup devices (Connelly *et al.* 1979). A more exacting test is thus provided by studying weakly strain-hardening materials such as linear low density polyethylene (LLDPE). Schulze *et al.* (Schulze *et al.* 2001) present a comparison of transient extensional stress growth data for a commercially available LLDPE (Dow Affinity PL1880) in a number of RME devices and also report corrected strain rates that are determined independently from visual inspection of sample. The transient extensional response of this material has also been measured using a filament stretching rheometer (Bach *et al.* 2003). We thus perform corresponding measurements of the transient extensional rheology in LLDPE using the SER fixture.

We first describe the preparation and rheological characterization of the test samples. We then use two independent sets of SER test fixtures, mounted on a controlled rate and controlled stress instrument respectively, to measure the extensional stress growth in the LLDPE samples. We then turn our attention to the more strain-hardening low density polyethylene (LDPE) materials. We investigate the tensile stress relaxation following imposition of a small Hencky strain, and then measure the onset of strain hardening under steady uniaxial stretching conditions. We also demonstrate the ability to make tensile creep measurements in LDPE using the SER fixture mounted on a controlled stress rheometer and compare the results with the corresponding measurements of Münstedt *et al.* (Munstedt *et al.* 1998). Finally, we measure the relaxation of the tensile stresses following cessation of steady elongation over a range of imposed deformation rates, and observe sample necking and viscoelastic failure at large strains. Finally, we explore the viscoelastic nature of this failure condition in more detail using an ultrahigh molecular weight polyethylene sample.

2.2. Materials and procedures

2.2.1. SER Fixture

Extensional rheological measurements were performed on a SER Universal Testing Platform (Xpansion Instruments LLC) specifically designed for use as a detachable extensional rheometer fixture on commercially available torsional rheometer systems. Two different SER models were employed in the present work: (a) a model SER-HV-A01 was used on both a

TA/Rheometrics ARES and an RDA-II rotational rheometer, and (b) a model SER-HV-P01 was used on an Anton Paar Physica MCR501 rotational rheometer host system. This device is a controlled stress instrument that can also be operated in a controlled-strain mode.

As shown in Figure 2-1, and described in detail by Sentmanat (Sentmanat 2003; Sentmanat 2003; Sentmanat 2004), the SER consists of paired master and slave windup drums mounted on bearings housed within a chassis and mechanically coupled via intermeshing gears. Rotation of the drive shaft results in a rotation of the affixed master drum and an equal but opposite rotation of the slave drum which causes the ends of the sample (which are secured to the drums by means of securing clamps) to be wound up onto the drums resulting in the sample being stretched over an unsupported length, L_0. Axial sagging of the sample is inhibited by mounting the molten sheet of the test sample vertically, rather than horizontally as in the RME, and is not an issue for samples with zero-shear-rate viscosities in excess of $10^4 Pa\ s$. A detailed analysis of the geometric requirements to be fulfilled in order to neglect sagging is provided in the appendix to Sentmanat (Sentmanat 2004).
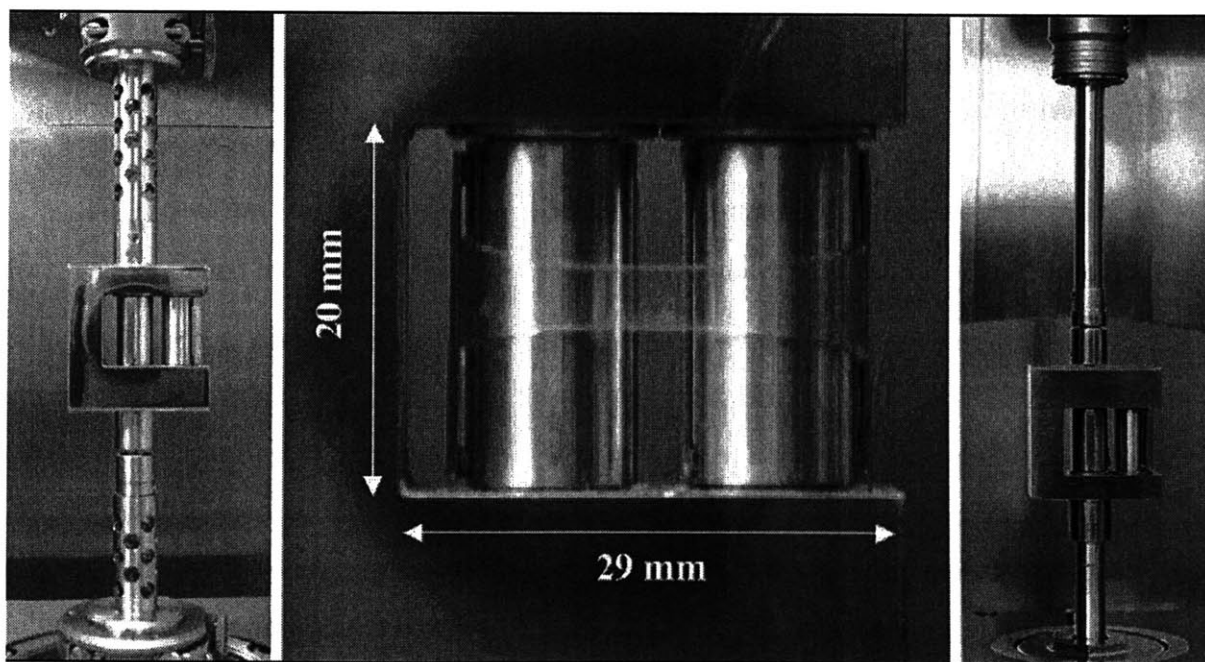
Figure 2-1. Photos of the SER universal testing platform, from left to right; (a) the model SER-HV-A01, (b) a polyolefin melt sample being stretched during an extensional rheology measurement, and (c) the model SER-HV-P01.

For a constant drive shaft rotation rate, V, a constant Hencky strain rate is applied to the sample specimen that can be expressed as

$$\dot{\varepsilon}_H = \frac{2\Omega R}{L_0} \qquad (2\text{-}1)$$

where R is the radius of the equidimensional windup drums, and L_0 is the fixed, unsupported length of the specimen sample being stretched which is equal to the centerline distance between the master and slave drums. The resistance of the specimen to elongation is observed as a tangential force, F, acting on both the master and slave drums which is then manifested as a torque, M, on the torque transducer attached to the fixture. It has been shown (Sentmanat 2004) that the measured torque signal, $M(t)$, is related to the tangential stretching force, F, in the following manner:

$$M(t) = 2RF(t) \qquad (2\text{-}2)$$

This expression has been shown to be valid for measured torque values greater than $M \geq 4.0 \times 10^{-5}$ Nm with bearing friction contributing less than 2% to the total measured torque signal.

For a constant Hencky strain rate experiment, the instantaneous cross-sectional area, $A(t)$, of a stretched molten specimen decreases exponentially with time, t. Now although the width and thickness dimensions of the prepared polymer specimens were measured at room temperature prior to loading on the SER, the polymer samples exhibit a decrease in density upon melting that is manifested as a volumetric expansion of the specimen span while loaded on the SER. In order to account for this dimensional expansion, affine expansion of the sample is assumed and the following expression was used to calculate the cross-sectional area of the molten polymer specimen for a constant Hencky strain rate experiment:

$$A(t) = A_0 \left(\frac{\rho_S}{\rho_M} \right)^{2/3} \exp\left(-\dot{\varepsilon}_H t\right) \tag{2-3}$$

where A_0 is the cross-sectional area of the specimen in the solid state, ρ_S is the solid state density, and ρ_M is the melt density of the polymer. Note that any expansion in the unsupported span length of the polymer is observed as a slight lag in the torque response that can be accounted for with a slight time offset in the recorded time data. For a constant Hencky strain rate, the tensile stress growth function, $\eta_E^+(t)$, of the stretched sample can then be expressed as

$$\eta_E^+(t) = \frac{F(t)}{\dot{\varepsilon}_H A(t)} \tag{2-4}$$

where $F(t)$ is the instantaneous extensional force exerted by the sample at time t as it resists stretching and as determined from the measured torque signal, $M(t)$ and Equation 2-2.

In an extensional stress relaxation experiment with the SER, the tensile relaxation modulus, $E(t)$, of the stretched sample can be found from the expression

$$E(t) = \frac{F(t)}{\varepsilon_H A(t)} \tag{2-5}$$

where $F(t)$ is the instantaneous extensional force at time t exerted by the sample as it relaxes from the imposed step Hencky strain, $\varepsilon_H = 2R\Delta\theta / L$. Although this has historically been a very difficult measurement to perform with conventional extensional melt rheometer technology, the use of a standard torsional rheometer makes this achievable because the drive system has been designed with the ability to rapidly impose a step angular displacement, $\Delta\theta$.

In a tensile creep experiment at a constant stress $\sigma_0 = F(t) / A(t)$, the tensile force imposed on the sample must vary in the same manner that the cross-sectional area of the sample varies; i.e., it must decrease exponentially with Hencky strain. Hence, in order to perform constant tensile stress experiments with the SER, the torque of the MCR501 controlled stress

rheometer is programmed in the firmware to decay exponentially with the angle of spindle rotation such that $M = M_0 \exp(-\varepsilon_H)$ where M is the applied torque, M_0 is the initial applied torque (based on the desired tensile creep stress for a given initial cross-sectional area of the melt sample), and $\varepsilon_H(t) = 2R\Delta\theta(t)/L$ is the measured Hencky strain. The extensional creep compliance is then defined as $D(t,\sigma_0) \equiv \varepsilon_H(t)/\sigma_0$.

2.2.2. Sample Preparation

Sample specimens of LLDPE Affinity PL1880 ($M_n = 36,000$, $M_W = 97,000$, $\eta_0 = 7.9 \times 10^4$ Pa s @ 130 °C) supplied by S. Costeux (Dow) and LDPE Lupolen 1840H ($M_n = 17,000$, $M_W = 240,000$, $CH_3/1000C=23$, $\eta_0 = 5.9 \pm 0.3 \times 10^4$ Pa s @ 150 °C) supplied by C. Gabriel (BASF) were prepared by compression molding approximately 7 g of polymer pellets at a temperature of 150 °C between smooth polyester film sheets to a nominal gage thickness of 0.65–1 mm. Sample thickness was controlled by using thin flat window frame molds of uniform gage, sandwiched between two flat steel platens. The samples were compression molded for a period of 10–15 min in a preheated hydraulic press and then removed and allowed to cool to room temperature by natural convection. Once the sample had cooled to room temperature, a long strip approximately 15–18 mm in width was cut from the flat molded sheet. Small rectangular specimens 12.7 mm in fixed width were then cut from the long strip section using a dual blade cutter with a fixed gap spacer. The final dimensions of the solid polymer specimens were approximately 17 mm in length x 12.7 mm in width, with thicknesses in the range of 0.65–1 mm.

Prior to sample loading, the SER fixture was heated to the desired value (130 °C for LLDPE and 150 °C for the LDPE tests) using the environmental chamber of the host system. Once the oven temperature had reached the set point, the fixture was allowed to soak at temperature for a minimum of 20 min prior to initial sample loading. The loading procedure involved opening the oven chamber door and using a pair of fine tweezers, loading and securing the specimen onto the preheated SER fixture, then closing the oven chamber door all within a

time span of about 20–30 s. A period of about 90 s was allowed to elapse prior to starting a test in order to allow the oven and sample specimen to reach the test temperature. The characteristic thermal diffusion time for sample equilibration may be estimated as $t_{diff} \approx \rho_M c_P h^2 / k$, where h is the sample thickness and k, c_P are the thermal conductivity and specific heat, respectively. For 1-mm-thick samples, using published values for polyethylene (k=0.241 W/mK; c_P =2570 J /kg K, ρ_M=0.782 g/cm^3) we find $t_{diff} \approx \rho_M c_P h^2 / k$ < 8.4 s. The sample is thus well equilibrated within 90 s.

The measured density of both polyethylene samples at room temperature is ρ_s =0.92 g/cm^3. In the melt state ($T \geq 136°$ C), the density of all polyethylenes is reported to vary with temperature as $\rho_M (T) = \left[1.262 + 9.0 \times 10^{-4} (T - 125°C) \right]^{-1}$ with ρ_M in g/cm^3 (Meissner and Hostettler 1994). At a test temperature of 150 °C, the correction factor in Equation 2-3 is thus $(\rho_s / \rho_M)^{2/3} = (0.92 / 0.78)^{2/3} \approx 1.12$.

At the end of a test, molten specimen remnants on the windup drum surfaces and securing clamps were immediately removed using a small scraping tool fashioned from brass shim stock. A representative image taken during an interrupted test with the oven doors open is shown in Figure 2-1. The hyperbolic shape of the material elements taken up by the rotating drums is evident. Once the majority of specimen remnants had been removed from the fixture, the windup drums were carefully wiped clean with a soft disposable laboratory wipe to remove any remaining residue off the drum surfaces.

2.3. Results and Discussion

2.3.1. Transient extensional stress growth of LLDPE

We first investigate the evolution in the transient extensional viscosity function $\eta_E^+ (\dot{\varepsilon}_H, t)$ for the Affinity LLDPE. The data presented in Figure 2-2 were generated with a model SER-HV-P01 mounted on an Anton Paar MCR501 torsional rheometer using the controlled rate mode

of operation. The solid line shows the linear viscoelastic envelope $\eta_E^+ = 3\eta^+$ obtained from start-up of steady shear experiments with a cone and plate fixture. Theoretical considerations show that this defines the LVE envelope of extensional flow behavior (Bird *et al.* 1987). The zero-shear-rate viscosity of the Affinity sample can be determined from the long time asymptote of this curve to be $\eta_0 = 7.9 \times 10^4$ Pa s, in good agreement with Schulze *et al.*(Schulze *et al.* 2001). The tensile stress growth curves for the Affinity polyolefin exhibit little deviation from the linear viscoelastic envelope for extension rates $0.01 \leq \dot{\varepsilon}_H \leq 20$ s^{-1} up to the maximum achievable Hencky strain of $\varepsilon_H = 4.5$. In Figure 2-3 we compare these measurements with the "corrected" extensional results reported in Figure 8 of the round-robin study of Schulze *et al.* (Schulze *et al.* 2001). Each curve is offset along the ordinate axis by one decade for clarity. The data were generated with 2 SER models: an SER-HV- P01 hosted on an Anton Paar MCR501 and an SER-HV-A01 hosted on a Rheometrics RDA-II. In the SER design there is no relative slippage between the two counterrotating rollers and the samples; we do not correct the imposed deformation rate a posteriori but rather we directly specify rates of $\dot{\varepsilon}_H = 0.01$, 0.095, and 0.895 s^{-1} in order to enable direct comparison with Schulze *et al.* (Schulze *et al.* 2001). If desired, the homogeneity of the deformation can be verified by direct analysis of video frames because the fixture does not rotate during operation; representative data is presented elsewhere (Sentmanat 2004). At the highest extension rate of $\dot{\varepsilon}_0 = 0.895$ s^{-1} a small amount of strain hardening can be detected for Hencky strains $\varepsilon_H \geq 1$; however, in general, the extensional stress growth closely follows the linear viscoelastic envelope. The agreement of both sets of SER results with the LVE data at short times provide validation of the accuracy and reproducibility of the SER fixtures. By contrast, the RME results exhibit poor agreement (with up to a factor of two difference (Schulze *et al.* 2001)) with the equivalent linear viscoelastic (LVE) results at short times. This discrepancy is attributed by the authors to the belts taking up initial sample slack at times $t \leq 0.5$ s.
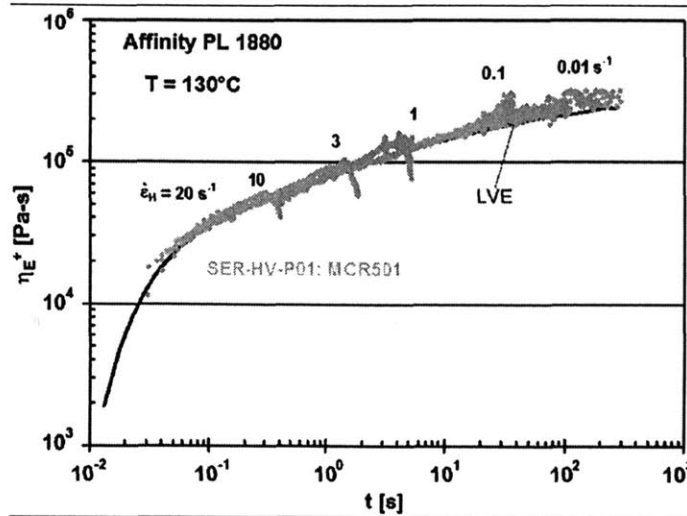
Figure 2-2. Tensile stress growth curves at a melt temperature of 130 °C for Affinity PL1880 LLDPE from Dow Chemical over a range of Hencky strain rates from 0.01 to 20 s^{-1} generated with the SER. Also shown is the LVE given by $\eta_E^+ = 3\eta^+$ obtained from cone and plate measurements in start-up of steady shear flow at $\dot\gamma = 0.003$ s^{-1}.
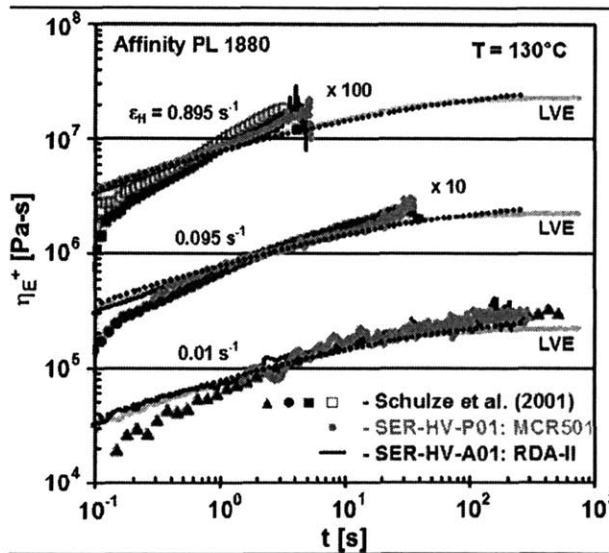
Figure 2-3. Tensile stress growth data at a melt temperature of 130 °C for Affinity PL1880 over a range of Hencky strain rates from 0.01 to 0.895 s^{-1} generated with the SER on two different host platforms, an MCR501 and RDA-II (light colored symbols and solid lines). The data are compared with extensional data taken from the literature [dark symbols from Schulze *et al.* (Schulze *et al.* 2001)]. Also shown is the linear viscoelastic envelope reported by Schulze *et al.* (Schulze *et al.* 2001) (light grey line), as well as our own measurements of the linear viscoelastic response (black dotted line) given by $\eta_E^+ = 3\eta^+$, obtained from cone and plate measurements in start-up of steady shear flow at $\dot\gamma = 0.003$ s^{-1}.

2.3.2. Shear Rheology of Lupolen 1840H

Having demonstrated the ability to measure the transient extensional viscosity of a very weakly strain-hardening material we now investigate a strongly strain-hardening low density polyethylene. The steady and transient shear rheology of Lupolen 1840H has already been studied in great detail by Münstedt and co-workers (Gabriel *et al.* 1998; Munstedt *et al.* 1998). Note that in these papers it is denoted as LDPE Melt I. Gabriel *et al.* (Gabriel *et al.* 1998) point out that long relaxation modes are present in the material as a result of the long chain branching and also that this material (which does not contain a stabilizer packaged is prone to thermal degradation at long times in excess of 3600 s). Following this earlier study (Gabriel *et al.* 1998) we perform creep measurements at shear stresses of $\tau_0 = 1000$, 100, and 10 Pa. At long times ($t \geq 500$ s) the compliance is found to increase linearly with time and becomes independent of stress amplitude. The zero-shear-rate viscosity of the sample can be computed from these measurements to be $\eta_0 = (5.9 \pm 0.3) \times 10^4$ Pa s in agreement with the published value of Gabriel *et al.* (Gabriel *et al.* 1998).

By using the techniques described by Gabriel *et al.* (Gabriel *et al.* 1998) and Kraft *et al.* 1999 (Kraft *et al.* 1999) — and which are now provided in modern software packages (TA Rheology Advantage version 5.0.38) — it is possible to use the measured creep data to augment measurements in small amplitude oscillatory shear flow without the need for excessively long test durations. In Figure 2-4 we show the measured linear viscoelastic moduli of Lupolen 1840H at 150°C together with the predicted values obtained from inverting a discrete retardation spectrum that was fitted to the creep data measured independently. The inset to Figure 2-4 also shows (on an expanded linear scale) the progressive change in the storage modulus measured at a single frequency of $\omega = 0.05$ rad/s. After an induction period of approximately 3000 s the material functions begin to change with increasing rapidity. For this reason all tests have been limited to durations of less than 1000 s. Small amplitude oscillatory shear flow experiments at temperatures $140 \leq T \leq 170$°C showed that before the onset of thermal degradation, the Lupolen samples obeyed the principles of time-temperature superposition with an Arrhenius activation energy of $E_a = 54.4$ kJ/mol.
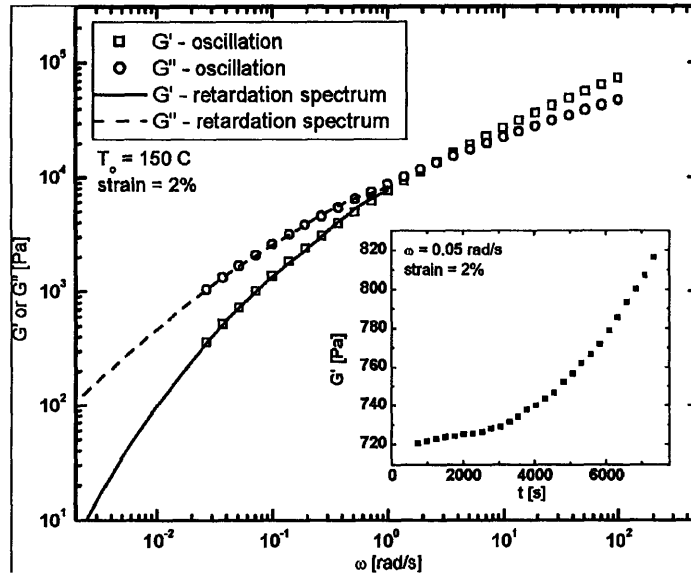
Figure 2-4. The linear viscoelastic moduli ($G'(\omega)$ and $G''(\omega)$) for Lupolen 1840H at 150 °C. Solid lines are calculated from creep measurements and the computed retardation spectrum, and the symbols are from small amplitude oscillation experiments. The inset data show the thermal stability of LDPE at 150 °C and the progressive change in the modulus for test times in excess of 3000 s.

2.3.3. Step strain relaxation modulus of Lupolen 1840H

There has been recent interest in investigating the stress relaxation in entangled polymer systems following imposition of a step extensional strain (Barroso and Maia 2002). As a validation of the capabilities of the SER fixture in the LVE flow regime, extensional stress relaxation experiments for a step Hencky strain of $\varepsilon_H = 0.4$ were performed with the SER-HV-A01 on a Lupolen 1840H sample at a melt temperature of 150 °C. This is the maximum step strain that can be imposed by the SER due to constraints imposed by the maximum angular displacement of the ARES motor ($\Delta\theta_{max} = 0.5$ rad). The resulting data for the tensile relaxation modulus (evaluated using Equation 2-5) can be compared with the LVE shear stress relaxation results taken from cone and plate measurements in step shear. As shown in Figure 2-5, a plot of the tensile relaxation modulus, $E(t)$, exhibits excellent superposition with a plot of $3G(t)$ taken

50

from the LVE shear stress relaxation data, and constitutes an experimental validation of Trouton's rule in stress relaxation mode.
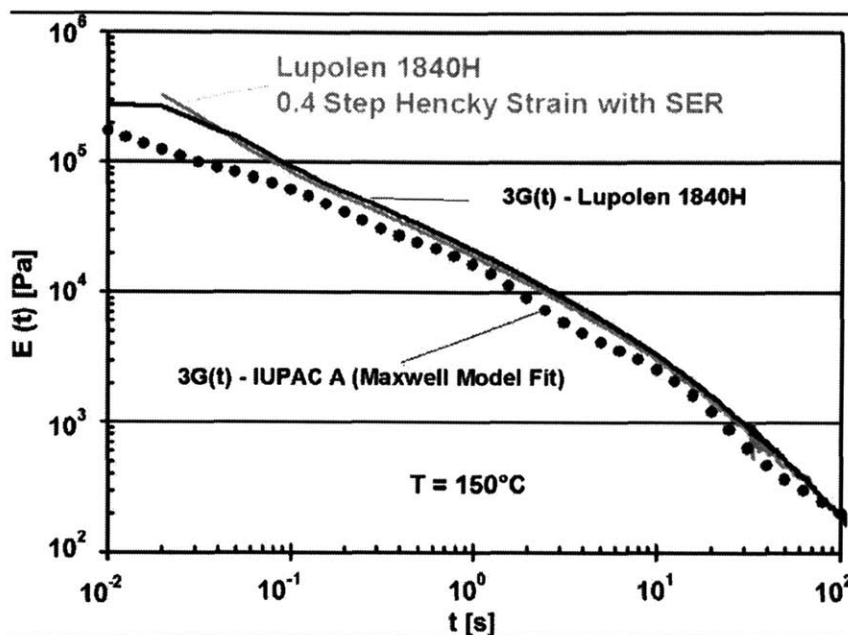
Figure 2-5. Tensile stress relaxation modulus at a melt temperature of 150 °C for Lupolen 1840H obtained from a step strain experiment with the SER to a Hencky strain of $\varepsilon_H = 0.4$ and a plot of $3G(t)$ using shear relaxation modulus data obtained from cone and plate measurements in a step shear experiment.

2.3.4. Transient extensional viscosity function

Start-up of steady extension experiments were performed on Lupolen 1840H at a melt temperature of 150 °C and over a range of Hencky strain rates from 0.003 to 30 s⁻¹, as shown in Figure 2-6. Once again we compare results obtained using separate SER fixtures mounted on both an MCR and an ARES rheometer. Superposed with the tensile growth data is the LVE shear stress growth data, $3\eta^+(t)$, for Lupolen 1840H at 150 °C taken from cone and plate measurements in start-up of steady simple shear flow. Data obtained at times $t \leq 0.01$ s are not plotted for either shear or extensional tests as they are convolved with the response function of the rheometer motors plus any residual sag in the sample resulting from uncorrected thermal expansion. The agreement between the low strain portion of the tensile stress growth curves and

the LVE simple shear data is noteworthy and provides experimental validation of the capabilities of the SER fixtures with regard to LVE flow characterization even for low deformation rates.

The significant strain hardening exhibited in the tensile stress growth behavior at large strains is inherent with polymer melts such as LDPE that contain a high degree of long-chain branching.
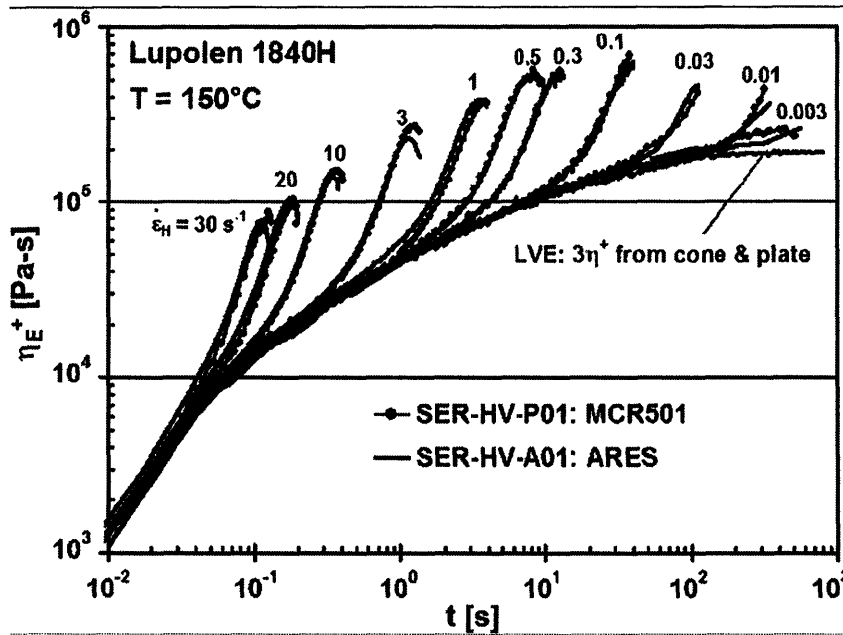
Figure 2-6. Tensile stress growth curves at a melt temperature of 150 °C for Lupolen 1840H over a range of Hencky strain rates from 0.003 to 30 s^{-1} generated with the SER on two different host platforms, an MCR501 and an ARES, and a plot of LVE $3\eta^+$ shear stress growth data taken from cone and plate measurements in start-up of steady shear at a shear rate of 0.005 s^{-1}.

Further validation of the extensional melt flow characterization capabilities of the SER are provided in Figure 2-7. Here we compare our tensile stress growth data with values taken from the literature (Munstedt *et al.* 1998) for the same Lupolen 1840H polymer (denoted melt I therein) and the same melt temperature. Despite the different rheometer technologies utilized to collect the extensional data in Figure 2-7, the agreement in this transient extensional rheological data is remarkable, particularly when one considers that even factoring in the sample loading, heating, testing, clean-up, and reheating time, the tensile stress growth data in Figure 2-6 took just over an hour to generate with the SER.
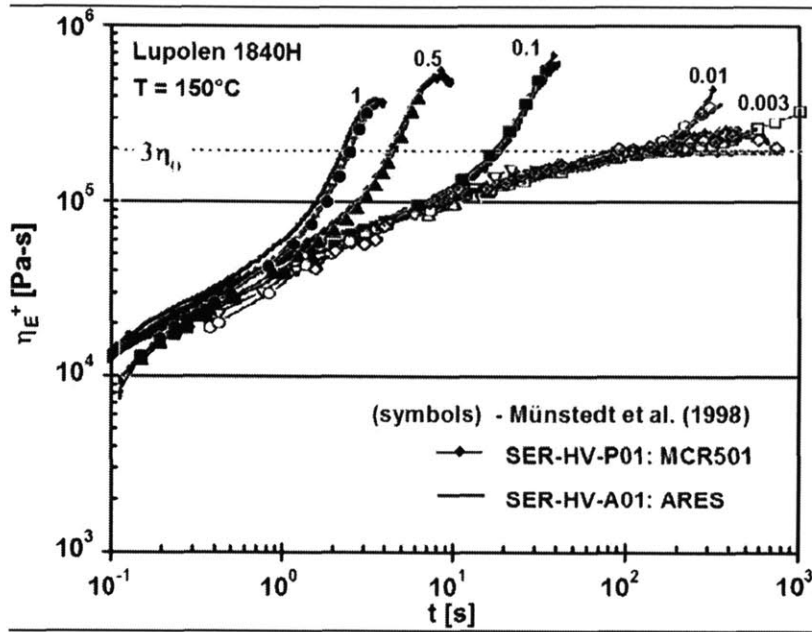
Figure 2-7. Comparison of tensile stress growth data at a melt temperature of 150 °C for Lupolen 1840H over a range of Hencky strain rates from 0.003 to 1 s⁻¹ generated with the SER on two different host platforms (solid lines) with extensional data taken from the literature (symbols with lines from (Munstedt *et al.* 1998)).

The original IUPAC A LDPE was synthesized more than three decades ago and some long term aging has resulted as a result of the absence of any stabilizer packages for free radical scavenging (Laun 2003). The present test material, Lupolen 1840H, has been proposed as an equivalent LDPE polymer material with regard to melt flow behavior and polymer macrostructure. Figure 2-8 contains a comparison of tensile stress growth data at a melt temperature of 150°C for Lupolen 1840H generated with the SER and IUPAC A results taken from the literature (Munstedt and Laun 1979). The LVE stress growth envelope for IUPAC A was calculated from the integral of a Maxwell model fit of the discrete relaxation time spectra reported in the literature (Rauschenberger and Laun 1997). This model predicts a higher extensional viscosity at short times $t \leq 0.02$ s than is observed in the Lupolen data; however, there is no extensional data available for IUPAC A at these short times to confirm or refute the model extrapolation.
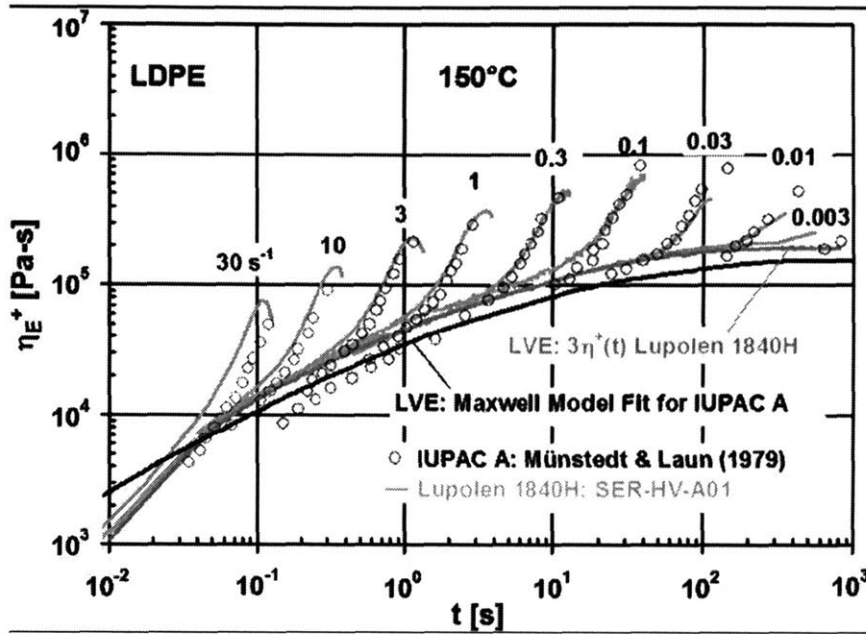
Figure 2-8. Comparison of tensile stress growth data at a melt temperature of 150 °C over a range of Hencky strain rates from 0.003 to 30 s⁻¹ for Lupolen 1840H generated with the SER (solid lines) and for IUPAC A taken from the literature (symbols from (Munstedt and Laun 1979)).

Note that although the two polymers exhibit qualitatively similar tensile stress growth behavior, there is an apparent difference in LVE stress growth behavior which is also reflected in the zero-shear viscosities of Lupolen 1840H $\left(\eta_0 = 5.9 \pm 0.3 \times 10^4 \text{ Pa s}\right)$ and IUPAC A $\left(\eta_0 = 5.2 \times 10^4 \text{ Pa s}\right)$. This difference suggests a slightly higher bulk average molecular weight for the Lupolen 1840H when compared to the IUPAC A material. Focusing on the large strain portion of the tensile stress growth curves, the data also suggest subtle differences in long-chain branching between the two polymers as witnessed by the slight variance in strain hardening behaviors, particularly at low rates of extension. This subtle difference in long-chain branching is further illustrated by the data in Figure 2-9 which provides a measure of the "steady uniaxial extensional viscosity" behavior of the two polymers. Following earlier work, we evaluate this steady state value from the peak of the tensile stress growth curves as a function of Hencky strain rate shown in Figure 2-6, such that $\eta_E(\dot{\varepsilon}_H) = \max\left[\eta_E^+(\dot{\varepsilon}_H, t)\right]$. Although an extensional viscosity can still be computed beyond this point using the measured tensile force, the imposed

54

deformation rate and the (assumed) exponential variation in the cross-sectional area, our stress relaxation experiments (see Sec. III F for details) coupled with theoretical and numerical stability considerations (Hassager *et al.* 1998; McKinley and Hassager 1999) suggest that beyond the maximum the elongating polymeric strip is in fact unstable to free surface perturbations that grow and result in necking of the sample, followed by complete rupture. The actual cross-sectional area and the local deformation rate in the neck will thus not be the same as the nominal imposed values. We therefore do not use the measured data beyond the maximum value of the transient extensional viscosity for representing the true steady-state extensional viscosity function.
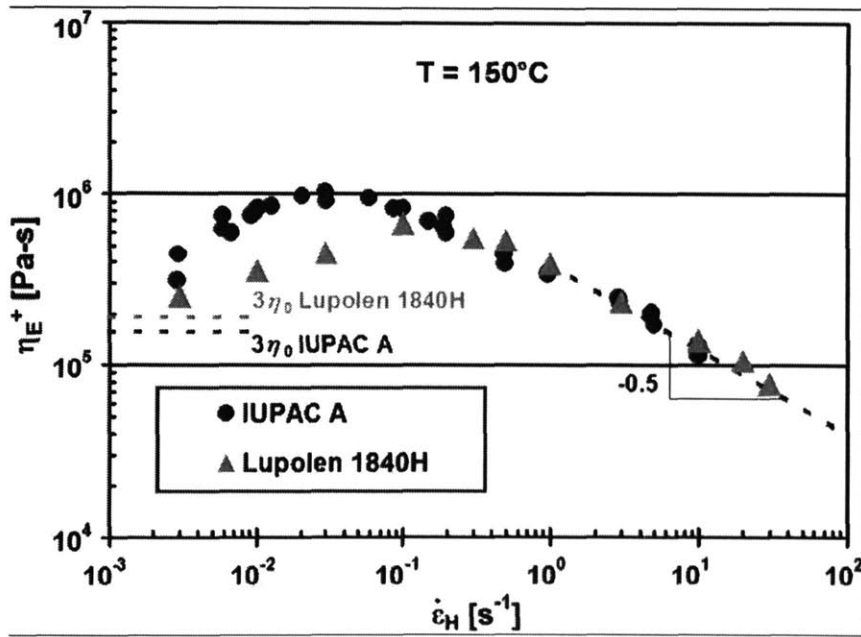
Figure 2-9. Comparison of the steady-state extensional viscosity behavior as a function of Hencky strain rate at a melt temperature of 150 °C for Lupolen 1840H generated with the SER (triangles) and for IUPAC A taken from the literature (circles from (Munstedt and Laun 1979)).

Although the deviation from the limiting zero-deformation rate behavior in Figure 2-9 appears to begin at approximately the same deformation rate for both materials, the Lupolen 1840H exhibits significantly less extensional thickening than the IUPAC A at low to moderate extension rates. This behavior is consistent with the presence of a reduced number of long-chain branches and a proportionally larger number of long linear chains. This observation is also

supported by the number of methyl groups per 1000 carbon atoms (CH₃/1000C) that has been reported in the literature for each polymer; 23 for Lupolen 1840H (Gabriel *et al.* 1998) and 30 for IUPAC A (Laun and Schuch 1989).

Using the SER fixture we were able to obtain tensile stress growth curves up to Hencky strain rates of $\dot{\varepsilon}_H = 30$ s⁻¹. The associated values of the "steady extensional viscosity" (as represented by the maximum in the transient extensional viscosity) at high deformation rates show extension thinning with an asymptotic slope close to $\eta_E \sim \dot{\varepsilon}_H^{-1/2}$. We discuss these observations further in Section 2.4.

2.3.5. Tensile creep under constant stress

By controlling the imposed torque on the SER-HV-P01 it is also possible to impose a constant tensile stress on samples of the Lupolen material. As Münstedt *et al.* ((Munstedt *et al.* 1998) note, tensile creep experiments typically approach steady state conditions more rapidly and the steady uniaxial viscosity can thus be extracted from tensile creep data over a wide range of imposed stresses. In Figure 2-10 we show a representative comparison of the shear creep compliance $J(t)/3$ for Lupolen 1840H measured using an AR2000 (TA Instruments) rheometer at constant shear stresses of $\tau_0 = 10$, 100, and 1000 Pa with the tensile creep compliance

$$D(t) = \varepsilon_H(t)/\sigma_0$$ measured using the MCR501 in controlled torque mode. Good agreement between the data is obtained at all times $0.3 \le t \le 300$ s. At short times $t \le 0.1$ s, damped inertioelastic oscillations are observed in the torsional data as a result of the moment of inertia of the instrument (Arigo and McKinley 1997). In Figure 2-11 we replot the measured Hencky strain $\varepsilon_H(t)$ at a constant tensile stress of $\sigma_0 = 1000$ Pa on a linear scale and compare it with the equivalent data reported by Münstedt *et al* (Munstedt *et al.* 1998). Numerical differentiation of the Hencky strain gives the strain rate in the sample which asymptotes to a value of $\dot{\varepsilon}_H = d\varepsilon_H/dt = 0.045 \pm 0.005$ s⁻¹ after times of 300 s. The imposed tensile stress and measured deformation rate can then be used to evaluate a steady elongational viscosity which we show in Figure 2-12 as a function of the imposed tensile stress.
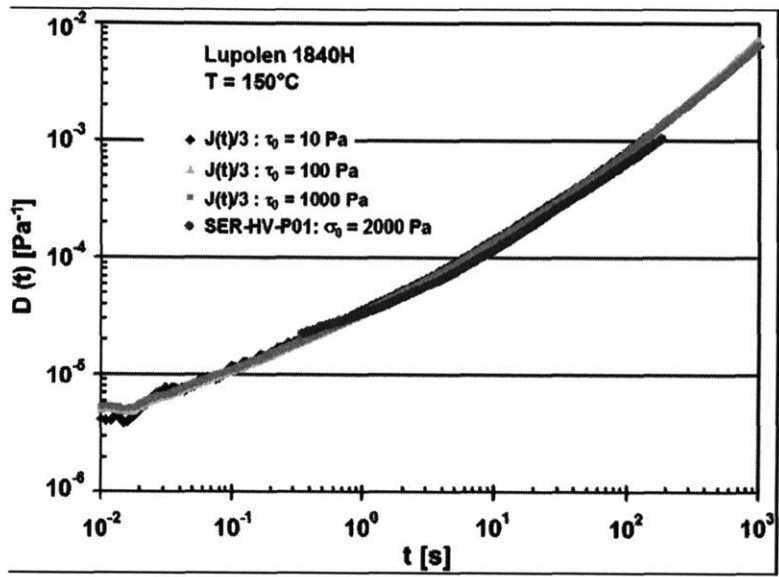
Figure 2-10. Comparison of shear creep compliance measurements for Lupolen 1840H from BASF at three stresses (150 °C) with tensile creep compliance measurements generated with the SER on a MCR501 host platform.
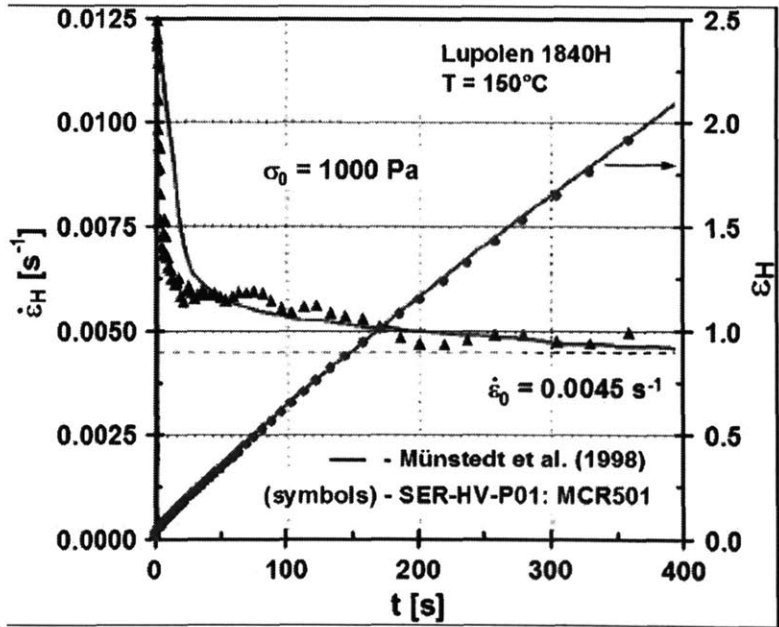
Figure 2-11. Comparison of tensile creep compliance data at a melt temperature of 150 °C for Lupolen 1840H at a tensile creep stress of 1000 Pa generated with the SER (symbols) with tensile creep compliance data taken from the literature (solid lines from Münstedt *et al.* (Munstedt *et al.* 1998)).
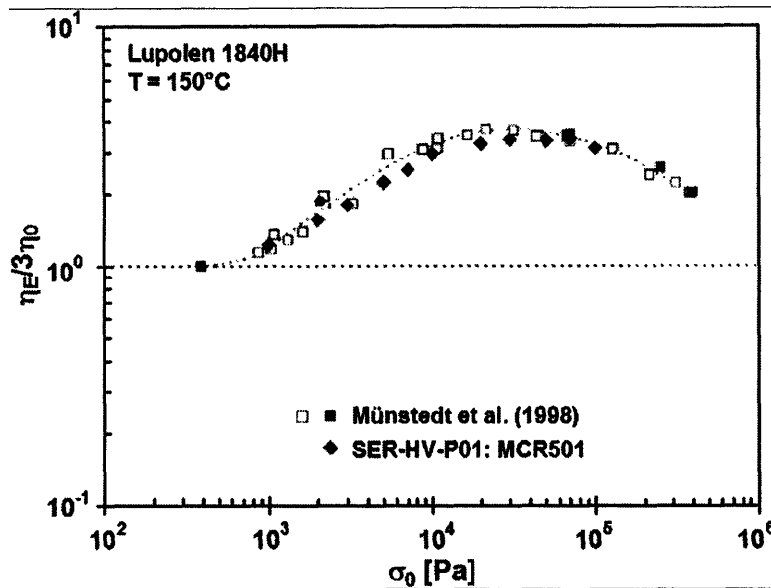
Figure 2-12. Comparison of steady-state extensional viscosity η_E (scaled with $3\eta_0$) as a function of the imposed tensile creep stress at a melt temperature of 150 °C for Lupolen 1840H generated with the SER (diamond symbols) with data taken from the literature (square symbols from Münstedt *et al.* (Munstedt *et al.* 1998)).

We obtain excellent agreement with the data of Münstedt *et al.*(Munstedt *et al.* 1998) for tensile stresses $10^3 \leq \sigma_0 \leq 10^5$ Pa .

2.3.6. Stress relaxation following cessation of stretching

The small moving mass of the SER fixture and the obviation of the need to impose an exponential increasing endplate velocity, as in a filament stretching rheometer, allows one to perform tensile stress relaxation experiments following elongation using the SER fixture. Cessation of steady extension rate experiments were performed on the Lupolen 1840H at a melt temperature of 150 °C, an applied Hencky strain rate of 0.5 Pa s^{-1}, and cessation times of $t_0 = 1,2,3,4,5$, and 6 s , respectively. The results of these experiments are shown in Figure 2-13. Included with the cessation data is the tensile growth curve for an uninterrupted strain rate test at

the same Hencky strain rate of 0.5 s^{-1}. Also depicted in Figure 2-13 is the LVE prediction of tensile stress growth and decay following the cessation of flow at a time, $t_0 = 1$ s (corresponding to a Hencky strain $\varepsilon_H = 0.5$) calculated from the following expressions:
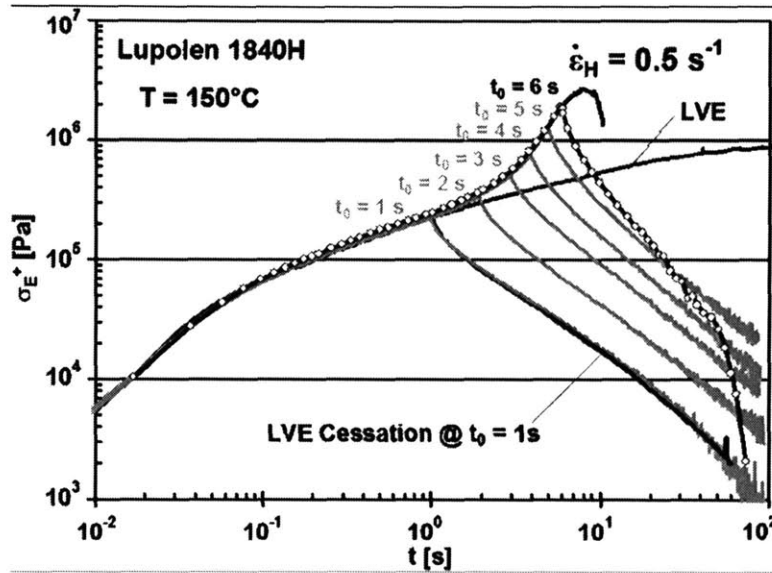
Figure 2-13. Cessation of steady extension rate experiments at a melt temperature of 150 °C for Lupolen 1840H at a Hencky strain rate of 0.5 s^{-1} and cessation times, t_0, (from bottom to top) of 1, 2, 3, 4, 5, and 6 s.

$$\text{for } t \leq t_0 \quad \eta_E^+(t) = 3 \int_0^t G(t)dt \tag{2-6}$$

$$\text{for } t > t_0 \quad \eta_E^-(t) = 3 \int_{t-t_0}^t G(t)dt \tag{2-7}$$

where $G(t)$ is the linear viscoelastic shear relaxation modulus. The superposition between the LVE stress growth and decay predictions and the SER tensile data for cessation of flow at $t_0 = 1$ s is noteworthy. In addition, the superposition of all the tensile stress growth data in Figure 2-13 provides a measure of the excellent experimental reproducibility that can be achieved with the SER.

The final stress relaxation curve shown in Figure 2-13, corresponding to the cessation of extension at a time of $t_0 = 60$ s $\left(\varepsilon_H = 3\right)$, exhibits an unexpectedly rapid decay in the tensile stress at long times. Inspection of the melt sample showed that it exhibited a subtle ductile necking phenomenon; the stretched sample continued to become progressively thinner in the region between the opposing rollers, while elastically unloading and recoiling near each roller. By contrast, all other samples remained homogeneous and continuous on the time scale of the experiments shown. Using the SER-HV-P01 fixture on the MCR501 we are also able to perform similar tensile stress relaxation experiments at short times and very high deformation rates as shown in Figure 2-14. We observe very similar behavior to that shown in Figure 2-13. Homogeneous relaxation is observed following stretching up to a maximum strain of $\varepsilon_H = (10)(0.25) = 2.5$; however, for larger initial imposed stretches a more rapid stress unloading and sample nonuniformity results.
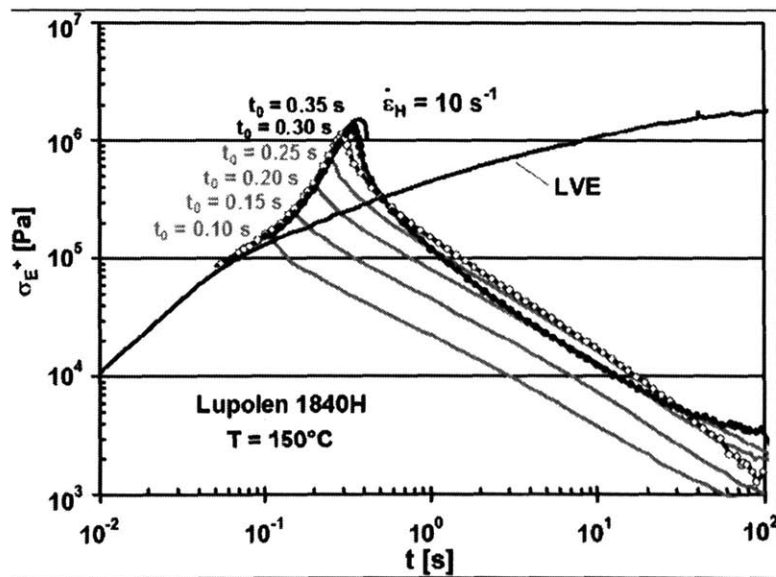
Figure 2-14. Cessation of steady extension rate experiments at a melt temperature of 150 °C for Lupolen 1840H at a Hencky strain rate of 10 s^{-1} and cessation times, t_0, (from bottom to top) of 0.10, 0.15, 0.20, 0.25, 0.30, and 0.35 s.

The onset of this necking instability and ultimate failure of the sample can be interpreted within the framework of the Considère criterion (Malkin and Petrie 1997; McKinley and Hassager 1999). In the rapid stretching limit corresponding to large Deborah numbers De $\gg 1$,

dissipative losses in a viscoelastic material become negligible. The Considère criterion can then be expressed in the following form; for uniform elongation of a sample to be possible, the engineering stress $F(t)/A_0$ must be monotonically increasing. This expression can also be re-expressed as requiring that the extensional viscosity must be sufficiently strain-hardening that it increases at least exponentially with the Hencky strain; corresponding to $d\ln\eta_E^+/d\varepsilon \geq 1$ (McKinley and Hassager 1999). A closer inspection of the transient extensional viscosity data in Figure 2-6, Figure 2-13, and Figure 2-14 shows that indeed necking failure in the sample occurs very shortly after the transient extensional viscosity ceases to strain-harden exponentially fast.

For a viscoelastic material, the rate of necking following onset of instability is of course more complex than described by the purely elastic Considère criterion (Joshi and Denn 2004). In particular the growth rate of the necking disturbance in the sample profile will be dependent on exactly how the tensile stress evolves with deformation rate and Hencky strain in the material (McKinley 2005). This can be seen more clearly in Figure 2-15 in which we replot the experimental measurements in terms of the *engineering stress*

$$\frac{F(t)}{A_0} \equiv \eta_E^+ \dot{\varepsilon} \exp(-\varepsilon_H) \tag{2-8}$$

The dimensionless times (or Hencky strains $\varepsilon_H = \dot{\varepsilon}t_0$) at which the stress relaxation experiments in Figure 2-13 and Figure 2-14 were commenced are also indicated by the large open circles. It is clear that the onset of necking instability is connected with the rapid decrease in the engineering stress at high strains: beyond a Hencky strain $\varepsilon_H \approx 3$ the stress decreases rapidly at either value of the imposed strain rates and it is energetically cheaper for the portions of the sample away from the end-rollers to neck down and rupture. Similar responses have been seen in numerical simulations of filament stretching experiments at high De using both integral and differential viscoelastic constitutive equations (Hassager *et al.* 1998; Yao *et al.* 1998) . These simulations also show that the rate of elastic unloading and necking failure is mediated by the presence and magnitude of any "solvent" contributions to the total stress arising from a true Newtonian solvent, a plasticizer, or unentangled oligomer.
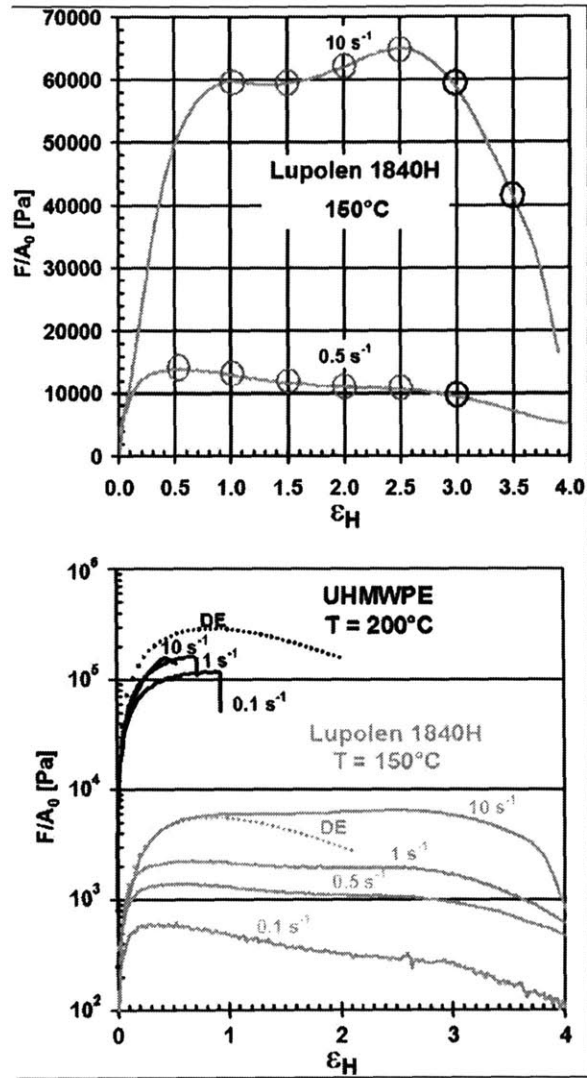
Figure 2-15. Evolution of the engineering tensile stress with Hencky strain over a range of Hencky strain rates: (a) data for Lupolen 1840H at a melt temperature of 150 °C at Hencky strain rates of 0.5 and 10 s⁻¹. The large open circles indicate the Hencky strains at which the stress relaxation experiments were performed. (b) Comparison with data for UHMWPE at a melt temperature of 200 °C. The broken lines show the predictions of the Doi–Edwards theory in the rapid stretching limit (see Equation 2-9).

To explore the predictions of the Considère criterion further it is desirable to perform tests in the rapid stretching limit (corresponding to $De \gg 1$) with highly entangled linear polymers. We have thus performed some preliminary experiments with an ultrahigh molecular weight (UHMWPE) polyethylene sample. The UHMWPE has a molecular weight in excess of

10^6 g/mol and the mechanical properties at room temperature have been characterized by (Pavoor 2003). As a consequence of the low entanglement molecular weight of polyethylene (M_e<828 g/mol), UHMWPE is a very highly entangled and stiff rubbery material even at test temperatures of 200 °C. Few measurements of the melt rheological properties have been published. Okamoto *et al.* (Okamoto *et al.* 1998) have studied the transient extensional rheology of LDPE/UHMWPE blends and demonstrate that strain hardening is still observed and that the stress-optical rule remains valid in the blends up to high extension; however, they only consider blends containing from 1% to 10% UHMWPE. Recently Wang *et al.* (Wang *et al.* 2003) reported measurements of the linear viscoelastic properties of 100% UHMWPE (in addition to Kaolin-filled samples) and documented the onset of slip-related instabilities in capillary extrusion.

In Figure 2-15b we show measurements of the engineering stress of an UHMWPE sample at T=200 °C over a range of imposed stretch rates. Very large tensile stresses are achieved at small strains; however, the samples show a rapid rupture-like failure at Hencky strains of less than unity. In contrast to the measurements with the LDPE melt (also shown in Figure 2-15b for comparative purposes), very little strain-rate sensitivity can be detected in the tensile stresses measured in the UHMWPE samples indicating the approach to the "rapid-stretching" elastic limit (De $\rightarrow \infty$). Finally, we also show in Figure 2-15b the predictions of the Doi–Edwards theory (broken lines). In the rapid-stretching limit, the engineering stress for the Doi–Edwards model is given by the following expression (McKinley and Hassager 1999):

$$\frac{F(t)}{A_0} = \frac{5G_N^0}{2\lambda(\lambda^3-1)}\left[2\lambda^3+1-3\lambda^3\frac{\tan^{-1}\left(\sqrt{\lambda^3-1}\right)}{\sqrt{\lambda^3-1}}\right] \tag{2-9}$$

where the axial stretch is $\lambda = \exp(\varepsilon_H)$ and G_N^0 is the Plateau modulus of the melt. The engineering stress passes through a maximum value of approximately 1.11 G_N^0 at a Hencky strain of $\varepsilon_{H,\max} = 0.86$.

For comparison of this theoretical prediction with the UHMWPE sample we use the accepted literature value of the plateau modulus for polyethylene; $G_N^0 = 2.6 \times 10^6$ Pa (Larson

1999). For the Lupolen melt which contains a broad distribution of linear and branched chains this is not an appropriate value. Instead we experimentally determine the Plateau modulus using the relationship $d\eta^+/dt\big|_{t=0} = G_N^0$ that can be derived from linear viscoelastic theory for small deformation rates. From the linear viscoelastic envelope in Figure 2-6 we thus obtain $G_N^0 = (5.0 \pm 0.1) \times 10^4$ Pa. In the case of the UHMWPE sample, the Doi–Edwards model provides a reasonably accurate upper bound to the experimental data and rupture is always observed at critical strains $\varepsilon_{crit} \leq \varepsilon_{H,max}$. For the Lupolen samples, the Doi–Edwards model provides a quantitative description of the initial stress growth in the material; however, the additional strain hardening resulting from the branched molecules results in a significant increase in the engineering stress at higher strains and also in the resulting strain to failure.

Finally, we show in Figure 2-16 the experimental data for the UHMWPE material plotted in terms of the transient extensional viscosity, computed using Equation 2-8. Because the engineering stress is bounded and almost rate independent, the evolution in the transient extensional viscosity is then dominated by the exponential decay in the cross-sectional area. As noted by Okamoto (Okamoto *et al.* 1998), the transient extensional viscosity can be described approximately by a polynomial $\eta_E^+ \sim t^n$. For the present UHMWPE, the data in Figure 2-11 suggests that $n<0.8$. The extensional viscosity increases monotonically without bound until the point of rupture and it is not possible to attain a steady extensional viscosity in this material for any deformation rate.
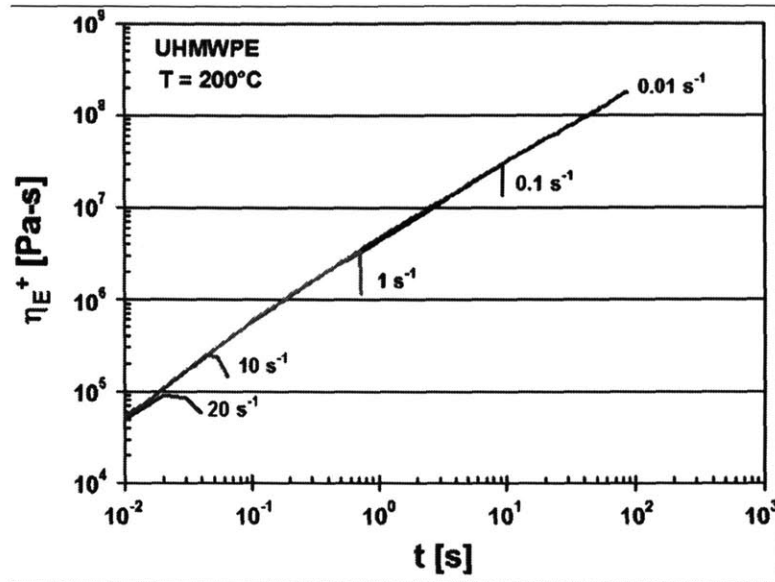
Figure 2-16. The transient extensional viscosity of an UHMWPE melt tested in the SER. The extensional viscosity continues to grow without bound at all extension rates until onset of necking instability and the sample ruptures.

2.4. Conclusions

In this chapter we have demonstrated that the SER Universal Testing Platform enables accurate and reproducible measurements of the transient extensional functions of viscoelastic samples such as polymer melts. We have performed tensile step strain, stress growth, tensile creep, and stress relaxation experiments using both a linear low density polyethylene (Dow Affinity PL 1880) and a low density polyethylene sample (Lupolen 1840H). Comparisons with published data for both materials show very good agreement over a wide range of imposed strain rates. Additional testing experience (Sentmanat 2004) shows that the SER test fixture can readily be used with stiffer materials such as elastomers and rubbers and also with lower viscosity materials; provided the zero-shear rate viscosity at test temperature is bigger than approximately $\eta_0 \geq 10^4$ Pa s.

The transient tensile stress growth experiments coupled with subsequent stress relaxation experiments following cessation of stretching have shown that the LDPE samples become unstable to necking perturbations beyond a critical Hencky strain. The driving mechanism for

65

this necking can be represented more clearly by examining the engineering stress that develops in the sample during stretching as shown in Figure 2-15. Earlier calculations (Hassager *et al.* 1998; McKinley and Hassager 1999) of the Considère criterion with the Doi–Edwards model and also with the Pom–Pom model of McLeish and Larson (McLeish and Larson 1998) have shown that it is the presence of long chain branching in the Lupolen samples that provides the plateau in the engineering stress at intermediate strains $1 \leq \varepsilon_H \leq 3$ and retards the onset of sample rupture. In the rapid stretching limit, the portion of the chain backbone between branches deforms affinely, and the branches act as true crosslinks until the process of branch-point withdrawal commences. This stabilizing process is absent in well-entangled linear melts, and analytic computation of the extensional stress for the Doi–Edwards model (McKinley and Hassager 1999) suggests that the engineering stress passes through a single maximum and then decays exponentially. The material becomes unstable to further elongation at moderate Hencky strains of less than unity. This situation was anticipated by Doi and Edwards (Doi and Edwards 1978) is supported by our observations of stress growth and rupture in UHMWPE. Such tensile stress growth measurements have also been used in materials selection considerations (Pearson and Connelly 1982).

Our transient elongational measurements with LLDPE grades show much less strain hardening than LDPE(Meissner and Hostettler 1994; Munstedt *et al.* 1998). They also exhibit lower elastic recoverable strain and may also develop inhomogeneities at smaller strains. The rate of ductile necking in these materials, however, is much less rapid than the elastic rupture we observed in the UHMWPE samples due to the viscous contributions to the stress. In such situations the Considère criterion does not provide a good measure of the strain to failure. Linear stability calculations (Hutchinson and Obrecht 1977) and numerical simulations of filament stretching experiments (Hassager *et al.* 1998; Yao *et al.* 1998) show that these viscous contributions to the total tensile stress can have a significant impact on the ductile necking rate and the total strain required to achieve complete sample failure.

We are able to obtain curves of the steady state elongational viscosities for the LDPE samples either by imposing controlled extension rates or by tensile creep experiments at constant extensional stress. To be consistent with previous experimental measurements using low density

polyethylenes, we have taken the maximum value of the measured transient extensional viscosity curve as the "steady state" value of the ideal uniaxial extensional viscosity at that strain rate. Recent measurements in other LDPE grades suggest that this maximum value may in fact represent an overshoot in the tensile stress growth with the steady-state extensional viscosity being as much as a factor of two lower (Rasmussen *et al.* 2005). The measurements shown in Figure 2-9 suggest that $\eta_E(\dot{\varepsilon}_H) \sim \dot{\varepsilon}_H^{-0.5}$ at high deformation rates. A similar power law decay at high strain rates was observed by (Bach *et al.* 2003) using a monodisperse polystyrene melt. Of course, the polystyrene data does not show the initial increase in the extensional viscosity observed in Figure 2-9 due to the absence of long chain branching.

The origins of this power-law decay in the extensional viscosity are not completely resolved. Reptation-based models such as the Doi–Edwards and Pom–Pom models predict a saturation in the tensile stress (occurring, respectively, when the chains reach full orientation or when branch-point withdrawal commences). The corresponding steady state extensional viscosity then decreases as $\dot{\varepsilon}_H^{-1}$. By contrast, dumbbell-based viscoelastic constitutive models incorporating finite chain extensibility and anisotropic drag do predict the initial extensional thickening (resulting from chain stretching) followed by power-law thinning at a rate $\dot{\varepsilon}_H^{-1/2}$ as a result of molecular alignment and anisotropic frictional drag on the elongated chain (Wiest 1989). The physical mechanisms that would lead to anisotropic drag on highly elongated polymer chains are expected to be valid whether or not the material is entangled under equilibrium conditions. Such a viewpoint is supported by filament stretching experiments in polymer solutions at high deformation rates: when the molecules are close to full stretch, measurements show that the steady-state extensional viscosity in dilute polystyrene solutions also decreases at a rate $\eta_E \sim \dot{\varepsilon}_H^{-1/2}$ (McKinley and Sridhar 2002).

An alternate interpretation has been put forward recently by Marrucci and Ianniruberto (Marrucci and Ianniruberto 2004). They have considered in detail the deformed shape of the "tube" in the reptation model and the resulting interchain pressure exerted on an elongated chain by the surrounding chains. The resulting model also predicts a power-law extensional thinning with a slope of −1/2. Measurements of the transient stress growth and ultimate steady state

elongational viscosity are greatly facilitated using the SER extensional test fixture. It is hoped that subsequent experiments with other monodisperse polymer melts will enable such phenomena to be investigated in greater detail in the future.

2.5. Acknowledgements

3. QUANTITATIVE CHARACTERIZATION OF THE MORPHOLOGY OF MULTI-WALL CARBON NANOTUBE FILMS BY SMALL-ANGLE X-RAY SCATTERING

(portions of this chapter are published in the Journal of Physical Chemistry C by B.N. Wang, R.D. Bennett, E. Verploegen, A.J. Hart, R.E.Cohen, May 2007)

Films of multi-wall carbon nanotubes (MWCNTs) grown by thermal chemical vapor deposition were studied using small-angle x-ray scattering (SAXS). We assessed the extent of alignment of carbon nanotubes (CNTs) by examining relative SAXS intensities as a function of azimuthal angle. We also identified features in the SAXS patterns that correspond well to CNT diameters measured through high resolution transmission electron microscopy. For the case of thick films, corresponding to CNTs with lengths on the order of a millimeter, we were able to study the morphology of the films as a function of distance from the catalyst substrate. We examined two different films in which the morphologies of CNTs range from vertically aligned to entangled and tortuous. We determined that the alignment of CNTs as well as their average diameter can vary significantly throughout the film, demonstrating the utility of SAXS for quantitative structural analysis of CNT films, and indicating potential to reveal new information about the CNT growth process by relating variations in morphology to evolution of the catalyst and reaction conditions.

3.1. Introduction

Films of carbon nanotubes (CNTs), grown by chemical vapor deposition (CVD) processes, have shown promise for use in nanoelectronics (Snow *et al.* 2003), energy absorbing foams (Chakrapani *et al.* 2004), superhydrophobic surfaces (Lau *et al.* 2003), and power applications (Raffaelle *et al.* 2005). The bulk morphology of these films, as well as the CNT dimensions, can be tailored through careful selection of catalyst and growth conditions (Hart and Slocum 2006; Hart *et al.* 2006). Recently, control of the size, location, and areal density of multi-walled CNTs (MWCNTs) was demonstrated through the use of a novel catalyst system based on iron oxide nanoparticles templated from poly(styrene-*block*-acrylic acid) micellar thin

films (Bennett *et al.* 2004; Bennett *et al.* 2005; Bennett *et al.* 2006; Bennett *et al.* 2006; Liu *et al.* 2006). A significant amount of tortuosity and CNT entanglement can be present despite efforts to create vertically aligned films (Bennett *et al.* 2006; Zhang *et al.* 2006). This entanglement can decrease the performance in certain applications and enhance suitability in others. Therefore it is important to understand the bulk morphology of CNT films to determine the appropriate choice of applications, as well as to relate this morphology to the reaction conditions.

Scanning electron microscopy (SEM) and transmission electron microscopy (TEM) have been the methods of choice to characterize the structure and arrangement of MWCNTs that make up these films (Bennett *et al.* 2006; Hart and Slocum 2006). TEM is a powerful tool that gives direct visualization of CNT dimensions and internal structure with resolution down to the angstrom scale; however it is inherently a local measurement. To obtain average CNT diameters using TEM requires many individual measurements from multiple micrographs, making the analysis of the macroscopic films tedious. In addition it is difficult to maintain the spatial correspondence between the location of the film and the TEM sample. SEM provides a mesoscopic view of MWCNT film morphology, but subjective image analysis is required to compare order and alignment and the resolution of SEM is typically insufficient to measure CNT diameters.

Scattering methods, such as small-angle x-ray scattering (SAXS) and small-angle neutron scattering (SANS) have been useful in interrogating features on the order of 1 – 100 nm (Lu *et al.* 2003; Graveland-Bikker *et al.* 2006; Kim *et al.* 2006; Wang *et al.* 2006). Though SAXS and SANS are not direct visualization techniques, they provide the Fourier transform of real space information and have been used successfully to study the orientation of single-wall CNT (SWCNT) bundles (Wei *et al.* 2002; Bendiab *et al.* 2003), the effect of sonication on the dispersion of SWCNT and MWCNT bundles (Schaefer *et al.* 2003; Brown *et al.* 2005), average diameters of individual CNTs (Burian *et al.* 2005; Hough *et al.* 2006), and the deformation of CNT-nanocomposites (Chen *et al.* 2006). Recently, Wang *et al.* demonstrated the utility of SANS as a technique to study the evolution of CNT orientation in vertically aligned MWCNTs (Wang *et al.* 2006). For a typical SAXS setup with a beam spot size on the order of a few hundred microns, the resulting data samples over millions of CNTs and can reflect a "locally

averaged" measurement of CNT morphology. Thus SAXS provides a larger length scale counterpart to electron microscopy in studying MWCNT films, while extracting information based on nanoscale characteristics.

In this chapter we provide additional validation of scattering techniques, specifically edge-on SAXS measurements in our case, for studying the bulk morphology of MWCNT films. Using SAXS we verify measurement of spatial variations in MWCNT orientation, which was first demonstrated using SANS in the work of Wang *et al.* (Wang *et al.* 2006) In addition we use SAXS to measure a locally-averaged spatial variation in CNT diameters within our films and we verify the average results using TEM imaging. We also use SAXS to study the morphological characteristics of two different MWCNT films to confirm earlier reports that changes in morphology from entangled bundles of CNTs to well aligned vertical growth can occur.(Hart and Slocum 2006) Relatively little prior effort has been directed towards studying morphological changes through the thickness of CNT films although Eres *et al.* demonstrated the utility of Raman spectroscopy in this endeavor (Eres *et al.* 2005). Because thick films of millimeter-long CNTs can be grown (Lee *et al.* 2002; Deck and Vecchio 2005; Hart and Slocum 2006), these films can be readily studied using edge-on SAXS experiments.

3.2. Experimental Methods
3.2.1. Small-angle x-ray scattering

Two different small-angle x-ray scattering systems were used. The first system (Molecular Metrology, Northampton, MA) is a simultaneous SAXS/WAXS-image plate setup which employs a Gabriel type 2-D multi-wire detector with a pixel width of 0.1315 mm. This system uses a MaxFlux® source (Osmic Inc., Auburn Hills, MI) operating at 45 kV and 0.66 mA (radiation $\lambda_{Cu-K\alpha}$ = 0.1542 nm) with three pinhole collimation. The diameter of the circular spot size for the SAXS is approximately 0.5 mm. Silver behenate (with a first order scattering vector, q = 1.076 nm^{-1} where $q = 4\pi \sin\theta/\lambda$ where 2θ is the scattering angle and λ is the wavelength) was used to calibrate the sample to detector distance, measured to be 1435.1 mm. Samples were positioned such that x-rays passed edge-on (along z-axis) through the film of CNTs, as illustrated in Figure 3-1. A second set of studies was performed at the G1 beamline station at the Cornell

High Energy Synchrotron Source (CHESS). The wavelength of the x-rays was 0.1239 nm, and the sample to detector distance was 1124.5 mm. Pinhole collimation was used to achieve a resulting beam spot that is approximately 0.1 mm in height and 0.5 mm in width (respectively the y- and z- axes). We determined that instrumental effects have minimal influence on the reported results; the width of the beam spot leads to less than 0.03 nm^{-1} loss of resolution in the scattering vector, q, while the height of the beam spot contributes less than a 0.4 degree increase to the azimuthal breadth. Data were collected using a Flicam CCD x-ray detector with a detection area of 71.45 mm^2 and a pixel width of 0.06978 mm. Both systems use motors connected to the sample fixture, allowing for fine control of the vertical positioning of the sample, relative to the incident x-ray beam, to study CNT morphology at varying distances from the substrate. We define the location of the beam spot, relative to the substrate along the y-axis, as the variable h, as noted in Figure 3-1. Data shown in this manuscript are results from synchrotron work for ease of presentation; the results from the SAXS setup and the synchrotron are comparable for all samples studied.
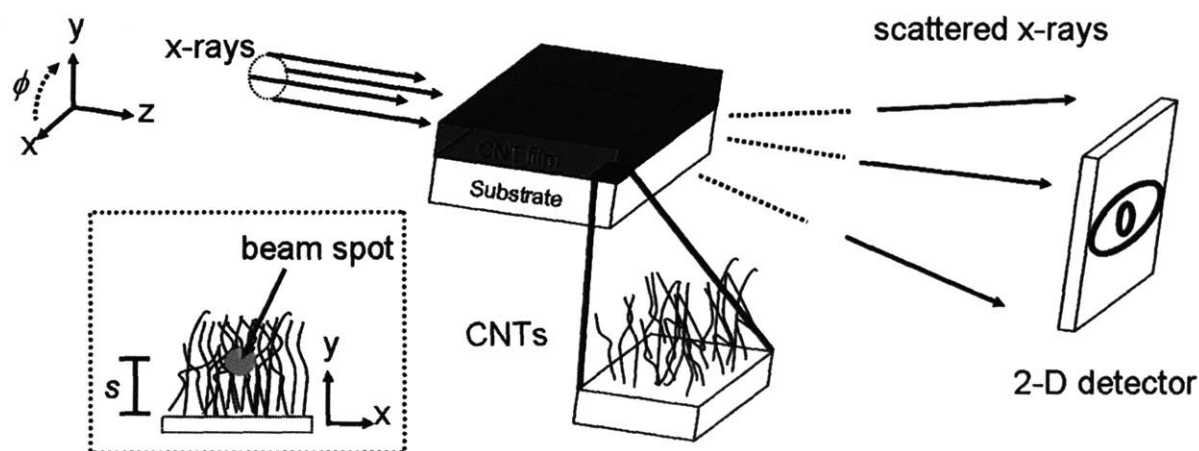
Figure 3-1. Experimental setup for SAXS. Incident x-rays travel parallel to the catalyst substrate in the z-direction. The sample is translated along the y-axis so the detection can occur at different heights (h) above the substrate.

Two-dimensional (2-D) detector images, corresponding to total x-ray impingement count, were analyzed using Polar Software (Ver 2.7.0, Stonybrook Technology and Applied Research, Inc., Stony Brook, NY). Intensities were corrected for background and offset for visual clarity. Because we assume that scattering is primarily due to the cross-section of the CNTs, perfect vertical CNT alignment (in the y-direction) would result in a SAXS pattern with intense, distinct features along the x-axis (Figure 3-1). Deviation from this expected pattern suggests less than perfect vertical alignment. In our notation the azimuthal angle $\phi = 0$ deg corresponds to the x-axis and increases in a counter-clockwise rotation.

3.2.2. Electron microscopy

High-resolution transmission electron microscopy (HRTEM) was performed on a JEOL 2010 operating at 200 kV. Specimens for HRTEM were prepared by sonicating the substrates containing CNTs in 2-propanol for 20 minutes, and then solvent-casting the CNTs onto lacey carbon films. Scanning electron microscopy (SEM) was performed on a JEOL 6320FV field-emission high-resolution microscope operating at 5 kV.

3.2.3. Carbon nanotube films

Two different samples of MWCNT films were created using different catalysts and growth conditions, which yielded CNTs of different diameters and lengths. SEM and inset HRTEM images showing local morphology and typical CNT diameters are shown in Figure 3-2. Sample 1 consisted of a 1.5 millimeter tall film of MWCNTs grown by thermal CVD of ethylene at 750 degrees Celsius, using a catalyst film of Al_2O_3 and Fe (10/1.2 nm thickness, respectively) supported on a Si substrate, with specific details provided elsewhere (Hart and Slocum 2006; Hart and Slocum 2006). Sample 2 was a 0.5 millimeter tall film of MWCNTs grown by thermal CVD of ethylene at 750 degrees Celsius, using catalytic iron oxide nanocluster arrays that were templated by a PS-b-PAA micellar film onto an Al_2O_3-coated Si substrate, with details listed elsewhere (Bennett et al. 2004; Bennett et al. 2006). Figure 3-2a is a representative SEM image of Sample 1 captured at $s = 0.2$ mm, near the substrate. The inset images are typical HRTEM

micrograph of MWCNTs, from which we obtain average CNT diameters (averaging over > 50 individual MWCNTs). CNT diameters measured for Sample 1 were 8.1 ± 0.9 nm. Figure 3-2b and Figure 3-2c illustrate the morphology of Sample 1 at $h = 0.9$ mm and $h = 1.4$ mm respectively. Figure 3-2d shows a typical SEM image of Sample 2 captured at $s = 0.4$ mm. CNT diameters measured for Sample 2 were 12 ± 2 nm. SEM qualitatively illustrates the morphology of these exemplary thick CNT films, which varies from highly aligned CNTs in Figure 3-2a, to tortuous and intertwined CNTs in Figure 3-2d.
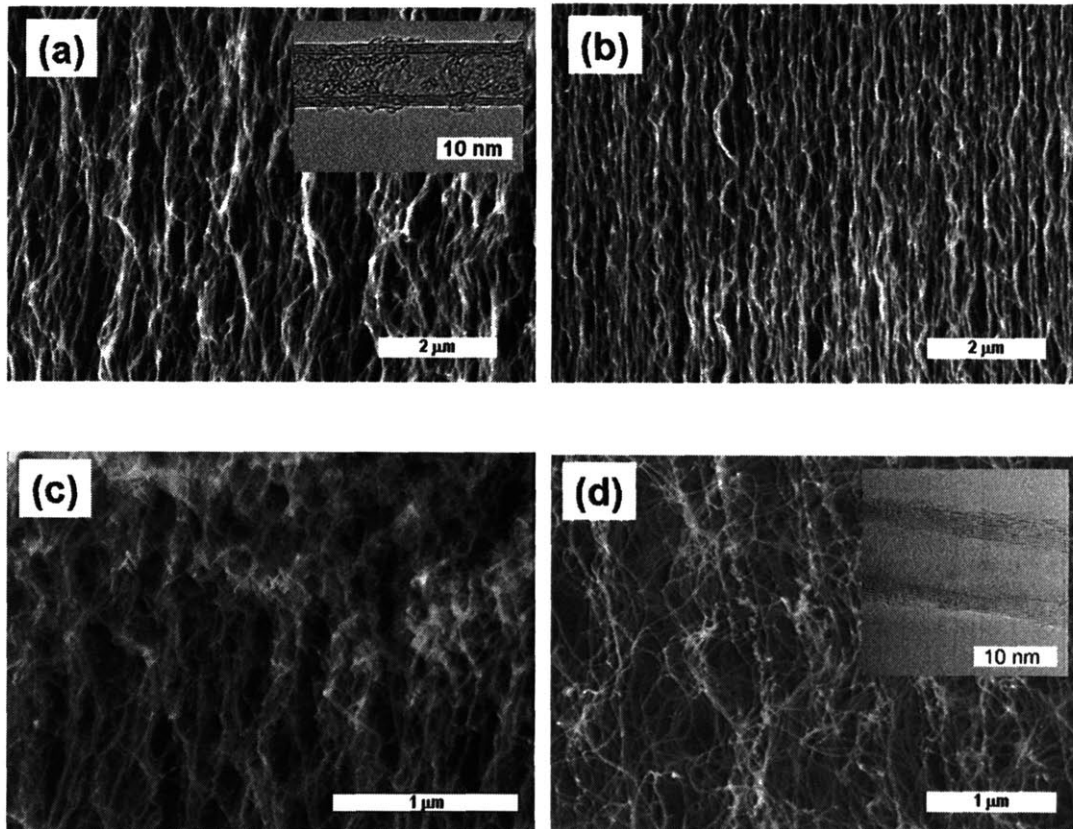
Figure 3-2. Representative SEM micrographs of MWCNT films taken edge-on. Sample 1 is shown (a) close to the substrate ($h = 0.2$ mm), (b) near the middle of the film ($h = 0.9$ mm), and (c) near the top of the film at ($h = 1.4$ mm). (d) Sample 2 is shown near the top of the film ($h = 0.4$ mm) HRTEM micrographs are shown inset reflecting typical CNT diameters.

3.3. Results and Discussion

Typical 2-D SAXS patterns are shown in Figure 3-3 for the different samples at varying distances from the substrate. Figure 3-3d shows the scattering pattern of Sample 1 close to the substrate. The pattern suggests alignment in the sample as evidenced by the distinct clouds at higher scattering angle localized near the x-axis, which we interpret to be a SAXS signature of the CNTs. We recall that scattering from the cross-section of preferentially vertical aligned CNTs in the y-direction should correspond to sharp clouds localized on the x-axis. The high intensity streak along $\phi = 90$ deg is due to a reflection off of the silicon substrate. An apparent evolution in morphology occurs as we increase h, as shown by the pattern in Figure 3-3c, where the scattering along the x-axis intensifies. This suggests that orientation could be increasing with h near the top of the film the scattering pattern shows a reduction in intensity as seen in Figure 3-3a. Similar patterns are shown for Sample 2 in Figure 3-3e, f, g and h. The SAXS pattern for Sample 2 suggests some orientation but we do not observe the distinctly resolved peaks exhibited by Sample 1.

Figure 3-4 and Figure 3-5 contain azimuthally integrated SAXS intensities versus scattering vector q extracted from the 2-D SAXS patterns; the intensities were obtained as conical slices (+/- 10 degrees) around different azimuthal angles ($\phi = 90$ deg and $\phi = 180$ deg) in the x-y plane of the detector. Figure 3-4a is the result of scattering along the x-axis for Sample 1. We observe a feature in the range of $q \sim 1.0$ nm^{-1}, which in accord with past work(Wei *et al.* 2002; Schaefer *et al.* 2003), we interpret to correspond to the characteristic outer diameter of the CNTs. As we increase h, there appears to be a shift in the feature to lower scattering angles which implies that the object responsible for the scattering increase in size with distance from the substrate. Furthermore the peak becomes less resolved with increasing h, ultimately resulting in a diffuse shoulder. Figure 3-4b shows scattering along the y-axis for Sample 1. It is evident that scattering along the y-axis exhibits a similar signature in the region of $q \sim 1.0$ nm^{-1}, though with diminished intensity and increased noise.
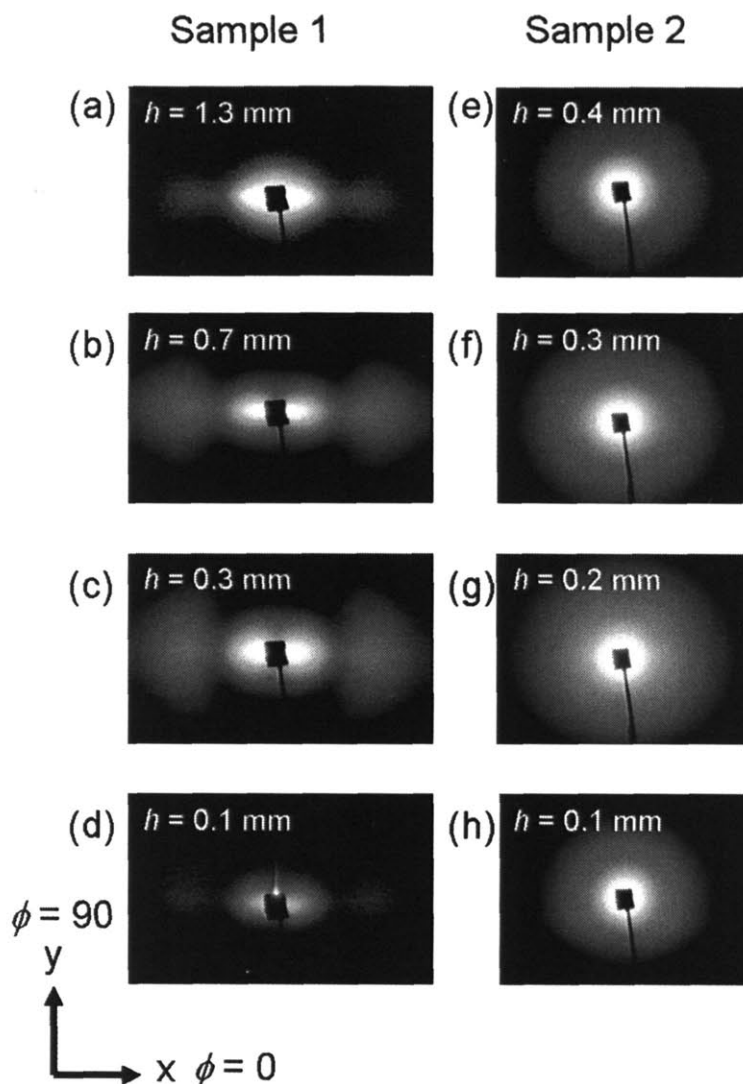
Figure 3-3. Representative 2-D SAXS patterns of MWCNT films at different values of *h*.

Examining the data in Figure 3-4a and Figure 3-4b we make inferences regarding the morphology of Sample 1. Close to the substrate to near the center of the film, there is vertical alignment, as shown by the intense, distinct peaks along the x-axis. Near the top of the film the alignment seems to degrade suggested by the peaks becoming less resolved.

The results from Sample 2, as shown in Figure 3-5, show behavior slightly different from the results shown for Sample 1. Near the substrate, we observe the presence of shoulder-like signatures in the range of $q = 0.6 - 0.8$ nm^{-1}, both in Figure 3-5a for the x-axis and Figure 3-5b

for the y-axis. Because the resolution of the shoulders and the intensities are low and comparable for both axes, the results suggest little preferential orientation in Sample 2. As we increase h the shoulder shifts to lower scattering angles in the same manner as Sample 1, though upon initial observation it appears that the shoulder actually shifts to higher scattering angles. This results from broadening of the shoulder due to the increased polydispersity of CNT diameters at higher values of h. From these results we infer that the morphology of Sample 2 is in general more tortuous than Sample 1 which is readily observed in the SEM micrograph of Figure 3-2   c.

Figure 3-6a and Figure 3-6b show azimuthal scans of 2-D SAXS patterns obtained from Sample 1 and Sample 2, respectively, at $q = 0.96$ nm^{-1} and $q = 0.62$ nm^{-1}, respectively. The presence of peaks at $\phi = 0$ deg and $\phi = 180$ deg correspond to vertical alignment of the CNTs. We note that there are different intensity values between the regions near $\phi = 90$ deg and $\phi = 270$ deg for measurements taken near the substrate, a result that we attribute to the presence of the x-ray opaque catalyst substrate below the CNT film. As we increase h, this difference disappears.
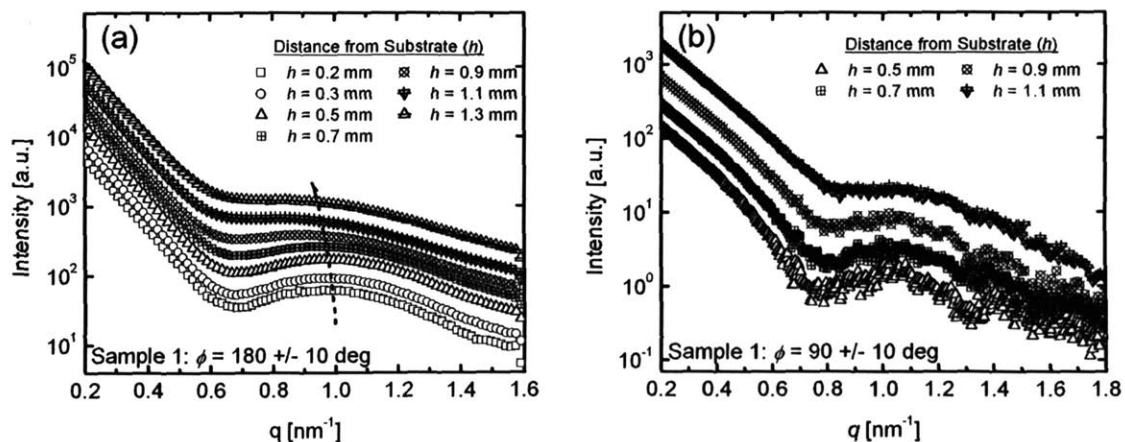
Figure 3-4. Azimuthally integrated SAXS intensities as a function of scattering vector for Sample 1 obtained by integrating over +/- 10 degree conical slices around (a) $\phi = 180$ deg **and (b)** $\phi = 90$ deg. **Distances noted in the legend correspond to vertical distance from the substrate (h). A peak lies near** $q \sim 1.0$ nm^{-1} **that shifts to lower scattering angles with increasing h (shown by the arrow).**
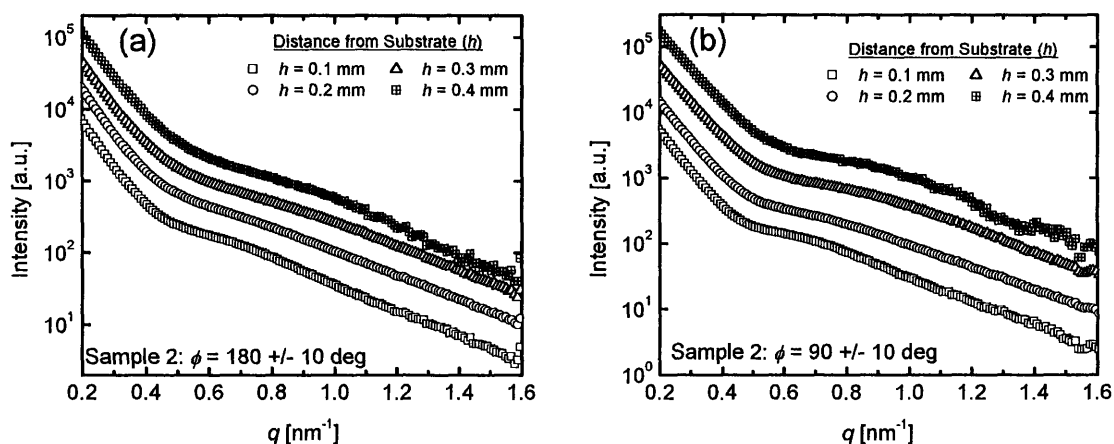
Figure 3-5. Azimuthally integrated SAXS intensities as a function of scattering vector for Sample 2 along the (a) $\phi = 180$ deg and (b) $\phi = 90$ deg.
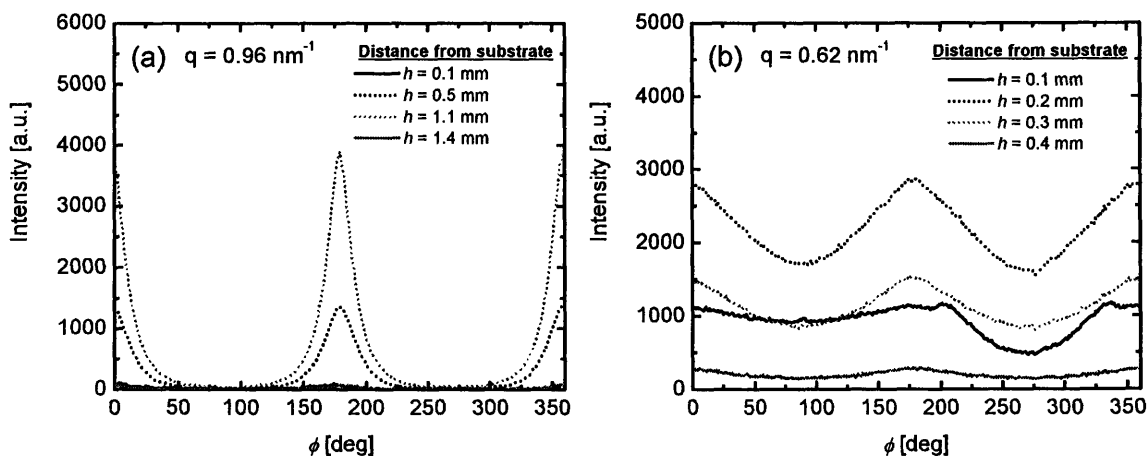
Figure 3-6. Azimuthal scans at varying distances from the substrate at $q = 0.96$ nm^{-1} for (a) Sample 1 and at $q = 0.62$ nm^{-1} for (b) Sample 2. $\phi = 0$ deg corresponds to the x-axis and increasing ϕ corresponds to a counter clockwise rotation. Peaks at 0 deg and 180 deg suggest preferential vertical alignment. The diminished intensity in the region of $\phi = 270$ deg close to the substrate, observed in (b) is due to obstruction of scattered x-rays by the substrate.

We extend our analysis of orientation by examining the Hermans orientation parameter, which can be defined for axially oriented systems as: (Alexander 1969; Finnigan *et al.* 2005):

$$f = \frac{1}{2}\left(3\left\langle\cos^2\phi\right\rangle - 1\right)$$

(3-1)

The factor in brackets represents the mean-square cosine of the azimuthal angle, calculated from the following equation:

$$\left\langle\cos^2\phi\right\rangle = \frac{\int_0^{\pi/2} I(\phi)\sin\phi\cos^2\phi\, d\phi}{\int_0^{\pi/2} I(\phi)\sin\phi\, d\phi}$$

(3-2)

Figure 3-7 reports f for the results of this analysis at varying distances from the substrate. The limiting values of $f = 1$, $f = 0$, and $f = -1/2$ correspond to perfect vertical alignment, random orientation, and perfect horizontal alignment respectively. From Figure 3-7 we observe quantitatively that Sample 1 shows substantially more vertical alignment than Sample 2, which shows essentially no preferred CNT orientation. In addition, the orientation in Sample 1 seems to be greatest in the middle of the film and less at the bottom and top of the film. The increase in alignment from the bottom of the film to the center of the film is in good correspondence with the SEM micrographs of Figure 3-2a and Figure 3-2b. Overall our analysis supports and confirms the previous assessment by Wang *et al.* (Wang *et al.* 2006) that spatially resolved SAXS data and the formalism of equation 3-1 and equation 3-2 allow for a clean and quantitative representation of morphological differences among various CNT film samples.
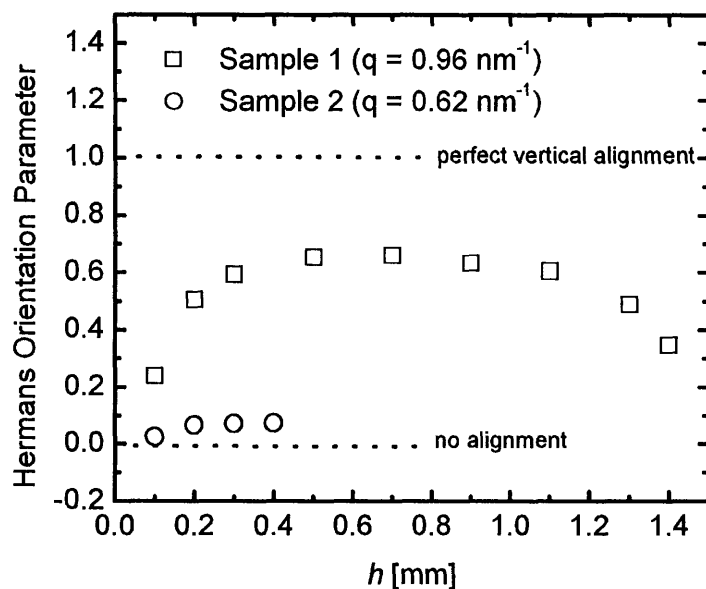
Figure 3-7. Hermans orientation parameter (*f*) as a function of distance from substrate (*h*). This quantitative description of alignment corresponds well to the qualitative representations provided by the SEM micrographs shown in Figure 3-2.

In addition to quantifying the orientation of the CNTs, we extract values for CNT diameters from the SAXS patterns. SAXS intensities can be expressed as:

$$I(q) = AF(q)S(q) \tag{3-3}$$

where $F(q)$ is the intra-particle form factor, $S(q)$ is the inter-particle structure factor, and A is an adjustable constant that accounts for instrumental and other experimental factors. The form factor for a rod-like particle can be expressed as (Lindner and Zemb 2002; Freiberger and Glatter 2006):

$$F(q) = \frac{L\pi}{q} I_C(q) \tag{3-4}$$

where L is the length of a CNT, $I_C(q)$ is the cross-section scattering function of a cylinder, and q

is the scattering vector. $I_C(q)$ can be expressed as the following integral:

$$I_C(q) = \frac{\int\limits_0^\infty P(R) f^2(q,R) dR}{\int\limits_0^\infty P(R) dR} \tag{3-5}$$

where $P(R)$ is the distribution function of cylinder radii and the specific f for a homogeneous

circular cylinder is:

$$f(q,R_o) = \Delta\rho R_0 \pi \frac{2 J_1(q R_o)}{q R_0} \tag{3-6}$$

J_1 is the spherical Bessel function of the first kind, $\Delta\rho$ is the difference in scattering density

distribution, and $R_o = \sqrt{2} R_{MWCNT}$, where R_{MWCNT} is the geometric radius of a CNT. We also

examined the data using form factors for hollow cylinders and concentric shells of cylinders as

suggested in the literature (Lindner and Zemb 2002; Lu et al. 2003) but did not observe

significantly better fits for typical values for CNT dimensions. We choose to include a Gaussian

distribution to account for polydispersity in CNT radii (Berney et al. 1982):

$$P(R_0) = \exp\left[\frac{-(R_0 - \langle R_0 \rangle)^2}{2\sigma_{R_0}{}^2}\right]$$

(3-7)

where $\langle R_0 \rangle$ and $\sigma_{R_0}{}^2$ are the mean and variance of R_0, respectively. The values for $\langle R_0 \rangle$ and $\sigma_{R_0}{}^2$ are selected such that the logarithmic root-mean-square error between the model and experimental data is minimized in the region of the CNT signature as described by:

$$error = \sqrt{\sum_{q=0.5}^{1.2}\left(\log I_{\text{expt}}(q) - \log I_{\text{model}}(q, \langle R_0 \rangle, \sigma_{R_0})\right)^2}$$

(3-8)

A representative illustration of this modeling procedure with the homogeneous hard cylindrical form factor (HCFF) is shown in Figure 3-8a for Sample 1 and Figure 3-8b and Figure 3-8c for Sample 2. We also include an example of the modeling procedure with a core-shell cylinder form factor (CSFF) (Inada *et al.* 2005) in Figure 3-8a, by selecting a shell thickness of 1.3 nm from HRTEM images. The numerical fit with the CSFF is inferior compared to the fit with HCFF. Furthermore CNT diameters resulting from the best fits using CSFF are slightly high compared to measurements from HRTEM. In light of these reasons, we selected the HCFF to model our data. We notice that the form factor essentially reproduces the feature, matching in peak location and breadth, but does not completely match with experimental data, even when we account for the polydispersity in CNT diameters. This is not altogether surprising, as the form factor describes only single particle scattering. The MWCNT films can be quite dense and the inter-particle interference, as represented by the structure factor $S(q)$ in equation 3, is not captured in the fit. It is challenging to define an appropriate structure factor; from the SEM images in Figure 3-2, it is evident that there exists a wide distribution of inter-particle spacing. Furthermore we show in Figure 3-8b and Figure 3-8c the subtleness necessary for accurate numerical fitting for films with wider variation in CNT diameters. It is apparent upon examination of Figure 3-8c that the aforementioned breadth of the shoulder, for Sample 2 at high values of h, is captured by a contribution of the first two peaks of the form factor. Despite the simplicity of the model, the best fit parameters extracted for CNT diameters $(d_{MWCNT} = 2(R_0 / \sqrt{2}))$ and standard deviations $(\sigma_{d_{MWCNT}} = 2(\sigma_{R_0} / \sqrt{2}))$ are comparable to those

directly measured by HRTEM. These values are illustrated and compared in Figure 3-9, demonstrating that SAXS provides an independent method of measuring average CNT diameter on a locally-averaged basis. The average CNT diameters which were measured by TEM fall near the midpoint of the spatial ranges established by the SAXS scans of each sample.
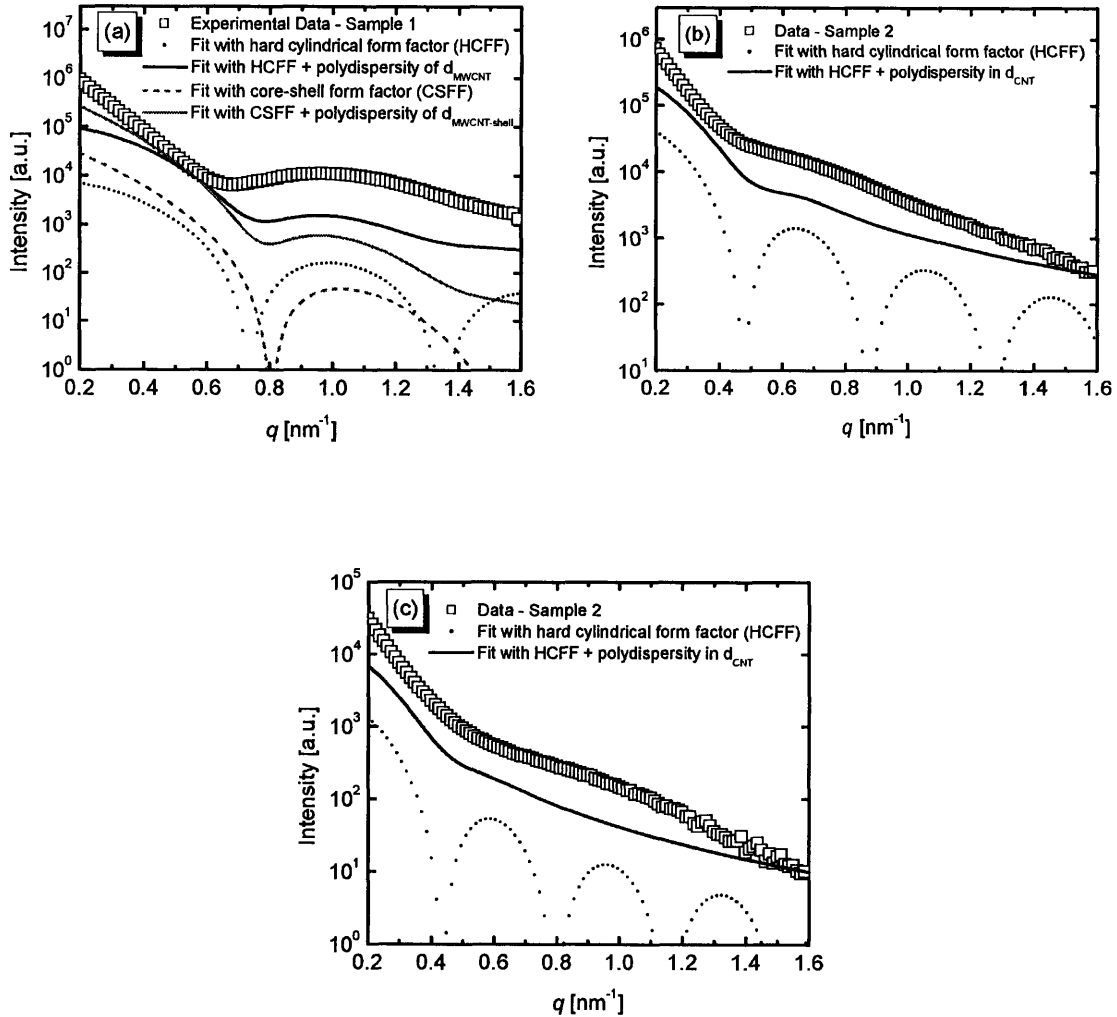
Figure 3-8. A representative example of fitting SAXS intensities to a hard cylindrical form factor model for (a) Sample 1 at $h = 0.3$ mm with $d_{MWCNT} = 7.4$ nm and $\sigma_{d_{MWCNT}} = 1.0$ nm, (b) Sample 2 at $h = 0.1$ mm with $d_{MWCNT} = 11.3$ nm and $\sigma_{d_{MWCNT}} = 2.1$ nm, and (c) Sample 2 at $h = 0.4$ mm with $d_{MWCNT} = 12.4$ nm and $\sigma_{d_{MWCNT}} = 2.5$ nm.
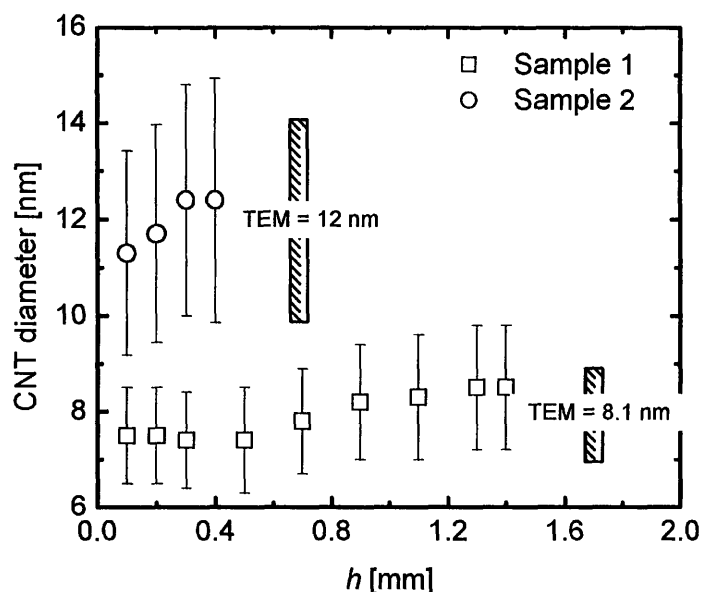
Figure 3-9. Summary of mean CNT diameters (d_{MWCNT}) and standard deviation ($\sigma_{d_{MWCNT}}$) at varying distances above the substrate (h) as measured by SAXS and compared against TEM measurements. Error bars from HRTEM are from actual measurements whereas error bars from SAXS are best fit parameters to provide minimum error between the form factor model and experimental SAXS intensities.

We now revisit the shift in the SAXS peaks noted in Figure 3-4a and Figure 3-5a. This feature appears at $q \sim 1.0$ nm^{-1} for scattering data obtained near the substrate and shifts to $q \sim 0.9$ nm^{-1} close to the top of Sample 1. This shift, quantified in Figure 3-9, suggests that the diameter of the CNTs, on average, is larger at the top of the film than near the substrate. Physically, however, there can be at least two interpretations for this observation. It is reasonable to expect that individual CNTs are physically wider at the top. It has been shown that for the catalyst system and growth conditions used for Sample 1, CNTs undergo a "base growth" mechanism and thus CNTs at the top of the film reflect conditions early in the growth process (Hart and Slocum 2006). In this case, the observed shift of the scattering data suggests that CNT diameters decrease during growth. We hypothesize that during the later stages of the growth process the catalyst loses activity and diffuses into the substrate, resulting in thinner CNTs. An additional effect is that, as poisoning continues, the density of active catalyst, and accordingly

84

density of CNT growth, decreases. Thus we observe a less aligned morphology that typically accompanies lower growth densities due to a reduced "crowding" effect, also observable in the micrographs of Figure 3-2 (Hart and Slocum 2006). Growth then terminates when the catalyst becomes fully inactive. This mechanistic picture is reflected in our SAXS measurements from Sample 1.

Recalling that SAXS is an average technique that samples a significant portion of the film volume, we offer another possible explanation for the above-mentioned trends in the data for Sample 1. Instead of individual CNTs becoming thinner near the substrate during the film growth, it is possible that there exists a larger proportion of wider CNTs near the top. This can occur if CNTs of larger initial diameter preferentially grow into longer CNTs or are initiated prior to thinner CNTs. Independent evidence, such as an extensive study using electron microscopy, will be needed to resolve this interesting issue.

3.4. Conclusions and Future Work

We have shown that scattering methods provide significant utility in studying the morphology of MWCNT films. As a counterpart to electron microscopy, SAXS obtains a measurement of CNT dimensions and orientation, averaged over millions of CNTs captured by the beam spot. Through the formalism and methodology established by Wang *et al.* (Wang *et al.* 2006), we were able to obtain a quantitative measure of CNT orientation. We examined intensities as a function of the scattering vector q to determine mean CNT diameters and their variances. The discrepancy between the SAXS data and a modeling scheme based on the intra-particle form factor for cylinders can be attributed to the high density of CNTs. Alternative systems that may provide an independent validation for the approach we have used here could include arrayed films of vertically aligned ZnO nanowires (Banerjee *et al.* 2005; Fan *et al.* 2005) or SWCNT films (Hata *et al.* 2004). Overall we have demonstrated that SAXS is a characterization tool that will aid in understanding the relationship between catalyst size, CNT diameters, growth conditions and the resulting morphology of MWCNT films.

Using the SAXS data, we characterized the morphology of two MWCNT films, fabricated under different growth and catalyst conditions. The two samples showed significantly different extents of orientation both when compared to one another, and as a function of distance from the substrate (h). We observed and quantified a change in morphology from entangled to vertically aligned growth through the thickness of a film. We also noted a widening in the average CNT diameters as h was increased. We speculate that this observation can correspond to preferential growth of wider CNTs. For film morphologies that are dictated by base-growth mechanism we include the possibility that the CNTs narrow as they grow from the substrate, with the widest portion of an individual CNT located at the top of the film.

3.5. Acknowledgements

4. CHARACTERIZING THE VARIATION IN THE MORPHOLOGY OF MANIPULATED MULTI-WALL CARBON NANOTUBE FILMS

(portions of this chapter have been submitted to the Journal of Physical Chemistry: C by B.N. Wang, R.D. Bennett, E. Verploegen, A.J. Hart, and R.E. Cohen 2007)

We used small-angle x-ray scattering (SAXS) to quantitatively characterize the morphological characteristics of pristine and mechanically manipulated multi-wall carbon nanotube (MWCNT) films. We determined that CNT diameters measured near the edges of a film were smaller compared to those measured in the interior. Uniaxially compressed MWCNT films exhibited a buckling deformation that was observable both in scanning electron microscopy (SEM) and SAXS. CNT films were also converted into cellular foams of CNTs through capillarity-induced densification. By examining spatially- and time-resolved SAXS data for the cellular foams, we identified low scattering angle features in the scattering curves that correspond to the average spacing between CNTs, demonstrating that SAXS is a useful method for monitoring the packing density of CNTs in a film. For all of the morphologies that were examined (aligned, disordered, compressed, and densified) SAXS data showed good correspondence with SEM images.

4.1. Introduction

CNT films have attracted significant interest from the engineering community because of their remarkable thermal, electrical and mechanical properties (Baughman et al. 2002; Chakrapani et al. 2004; Futaba et al. 2006; Hart and Slocum 2006) and the ease with which their morphologies can be macroscopically tailored (Lau et al. 2003; Wei et al. 2003; Hata et al. 2004; Bennett et al. 2005; Bennett et al. 2006; Bennett et al. 2006; Hart and Slocum 2006). Several groups have shown that by controlling reactor growth conditions CNT films can be grown into complex structures (Wei et al. 2002; Eres et al. 2005; Futaba et al. 2006; Hart et al. 2006). Hart et al. have shown that alignment in films of MWCNTs can be controlled by applying mechanical pressure during growth (Hart and Slocum 2006; Hart et al. 2006). Bennett et al., employing a

novel iron oxide nanoparticle based catalyst, showed that varying the density of catalyst particles, and corresponding CNT density, can give rise to a wide range of morphologies (Bennett *et al.* 2004; Bennett *et al.* 2005; Bennett *et al.* 2006). Templating techniques such as micro-contact printing have been employed in fabricating hierarchical CNT structures (Bennett *et al.* 2006; Hart and Slocum 2006; Liu *et al.* 2006). Chakrapani *et al.* converted MWCNT films into cellular foams through surface tension driven collapse of the film (Chakrapani *et al.* 2004). Kaur *et al.* have extended the work on cellular foams through the use of colloidal silica particles making "buckled" CNT films (Kaur *et al.* 2006) and Salgueriño-Maceira *et al.* have demonstrated visually appealing fractal-like structures based on similar particle templating. All of these studies relied primarily on electron microscopy for characterization of the morphology of CNT films.

In a previous paper, we showed that small angle x-ray scattering (SAXS) is useful in quantitatively studying the morphology of multi-wall carbon nanotube (MWCNT) films(Wang *et al.* 2007). SAXS provides morphological insight into both nanoscopic properties such as average CNT diameters and ensemble properties such as CNT orientation, reflecting a "locally-averaged" measurement. This arises from the mesoscopic size of the x-ray beam which is typically on the order of a few hundred microns. This dimension is simultaneously small in relation to the typical millimeter scale of films and large relative to the nanometer scale of individual CNTs. Thus the SAXS beam can probe a small region of the film to yield data that reflect information about millions of CNTs. The mesoscopic size scale of scattering techniques has been used successfully to demonstrate that the average diameter and orientation of MWCNTs can change as a function of distance from the film substrate (Wang *et al.* 2006; Wang *et al.* 2007).

In this chapter we use SAXS to study the morphologies of mechanically manipulated MWCNT films. We begin by characterizing areal variation in CNT diameters of pristine MWCNT films. We then examine the morphology of films that have been subjected to uniaxial mechanical compression. Finally we investigate the morphology of cellular foams made from capillarity-induced densification of MWCNT films and demonstrate that CNT packing density can be estimated from the SAXS data.

4.2. Experimental Methods

4.2.1. Small-Angle x-ray scattering

Small-angle x-ray studies were performed at the G1 beamline station at the Cornell High Energy Synchrotron Source (CHESS). The wavelength of the x-rays was 0.1239 nm, and the sample to detector distance was 1123 mm, calibrated with silver behenate (first order scattering vector of q of 1.076nm-1 (with $q = 4\pi \sin(\theta/\lambda)$ where 2θ is the scattering angle and λ is the wavelength). Slit collimation is used to achieve a resulting beam spot that is approximately 0.1 mm in height and 0.5 mm in width (the y- and x-axes, respectively). Data were collected using a Flicam CCD x-ray detector with a pixel width of 0.06978 mm. Additional studies were performed at the X27C beamline at the National Synchrotron Light Source (NSLS) at Brookhaven National Laboratory (BNL). The wavelength of the x-rays was 0.1371 nm and the sample to detector distance was 1789 mm. Pinhole collimation is used to achieve a beam spot approximately 0.3 mm in diameter and data were collected on a MarCCD x-ray detector with a pixel width of 0.158 mm. Both systems use motors connected to the sample fixture, which allowed fine control of the positioning of the sample, relative to the incident x-ray beam, to study the local CNT morphology at various locations in the film. We define the location of the beam spot, relative to the substrate along the y-axis, as the variable h, as noted in Figure 4-1a. Several experimental positions were used, altering the SAXS beam path through the MWCNT films, illustrated in Figure 4-1b – d.

Two-dimensional (2-D) detector images, corresponding to total x-ray impingement count, were analyzed using Polar Software (Ver 2.7.0, Stonybrook Technology and Applied Research, Inc., Stony Brook, NY). Intensities were corrected for background and offset for visual clarity. In our notation the azimuthal angle $\phi = 0$ deg corresponds to the x-axis and increases in a counter-clockwise rotation.

4.2.2. Electron Microscopy

89

Scanning electron microscopy (SEM) was performed on a JEOL 6320FV field-emission high-resolution microscope operating at 5 kV.
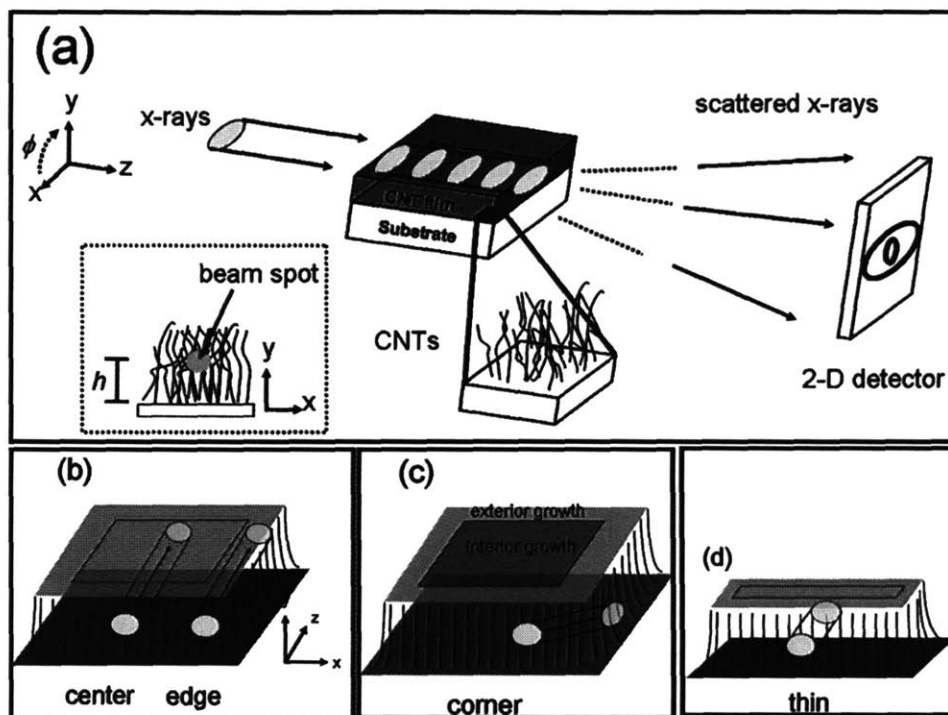
Figure 4-1. (a) General experimental setup. Diagrams showing SAXS beam path through the (b) center or edge, (c) through a corner, and (d) through the center of a thin sample.

4.2.3. Carbon nanotube films

Eight samples of MWCNT films were created using two different catalysts which yielded CNTs of different diameters and lengths. Sample 1 consisted of a film of MWCNTs grown by thermal CVD of ethylene at 750 degrees Celsius, using catalyst system 1, which consists of a film of Al_2O_3 and Fe (10 /1.2 nm thickness, respectively) supported on a Si substrate, with specific details provided elsewhere. (Hart and Slocum 2006; Hart and Slocum 2006) Sample 2 was a film of MWCNTs grown under the same reactor conditions with catalyst system 2, which consisted of a catalytic iron oxide nanocluster array that was templated by a PS-*b*-PAA block copolymer micellar film spin cast on an Al_2O_3-coated Si substrate, with details listed elsewhere (Bennett *et al.* 2004; Bennett *et al.* 2006). All other samples were prepared using catalyst system 1. Samples 3a and 3b were compositionally similar and simultaneously prepared, except that

Sample 3b is a thinner sample, illustrated in Figure 4-1. Sample 4 is a pristine MWCNT film, essentially the same as Sample 1. Sample 5 is a pristine MWCNT that was subjected to uniaxial compression; compression was achieved by placing a clean Si wafer on the film and applying pressure by hand until it was difficult to compress the film further. Sample 6 is a cellular foam; this structure was prepared from a MWCNT film which was immersed in ethanol followed by evaporation of the ethanol under ambient conditions. Samples 7 and 8 are identical to Sample 6 except that transformation into cellular foams occurred while *in-situ* SAXS data were being collected. Table 4-1 summarizes the catalyst systems and manipulations of each of the samples.

Table 4-1. Summary of samples with associated catalyst system and manipulation.

Name	Catalyst System	Manipulation
Sample 1	Al/Fe	pristine
Sample 2	Fe_2O_3	pristine
Sample 3a	Al/Fe	pristine
Sample 3b	Al/Fe	pristine – thin
Sample 4	Al/Fe	pristine
Sample 5	Al/Fe	uniaxial compression
Sample 6	Al/Fe	capillarity densification
Sample 7	Al/Fe	capillarity densification (*in-situ*)
Sample 8	Al/Fe	capillarity densification (*in-situ*)

4.3. Results and Discussion

4.3.1. Morphology of exterior versus interior growth in pristine samples

In our edge-on experimental setup [shown in Figure 4-1a] the SAXS beam passes through the entire width of the film. The resulting data reflect a combination of all individual scattering events along the beam path. Sampling different regions of the film with the SAXS beam will expose the presence of morphological variations that may be present in different regions of the film. For example, growth near the exterior versus the interior of the substrate can be examined by altering the beam path as shown in Figure 4-1b.

2-D SAXS patterns for a pristine MWCNT film, Sample 1, are shown in Figure 4-2a–c with the SAXS beam passing through the center of the film and Figure 4-2d-f for the SAXS beam traveling through the corner of the film [see Figure 4-1c]. For the case of the SAXS beam passing through the corner, we observe an azimuthal rotation of the primary scattering axis, illustrated in Figure 4-2g. This rotation is caused by CNT alignment that is not orthogonal to the substrate, even though the CNTs continue to be strongly aligned with each other. We define $\delta\phi$ as the angle between the primary scattering axis and $\phi = 0$, which is parallel to the substrate. We plot $\delta\phi$ as a function of the vertical distance from the substrate, h, in Figure 4-3a; these values of $\delta\phi$ can be used to recreate the average orientation of CNTs [Figure 4-3b] near the corner in terms of a distance from the edge, x, using Equation 4-1:

$$\cdot \qquad \Delta x = -(\Delta h)\cos\left((90 - \delta\phi)\right) \qquad\qquad (4\text{-}1)$$

where Δh is the vertical separation between SAXS measurements. We note that the relatively large values of $\delta\phi$ near the base of the tubes and the decrease in this angle with distance from the substrate results in the tops of the tubes being drawn inwards towards the interior of the film. This result is also shown clearly in the SEM image in Figure 4-3c.

Center **Corner**

(a) (d)

(b) (e)

(c) (f)

(g)

$\delta\phi$

primary scattering axis
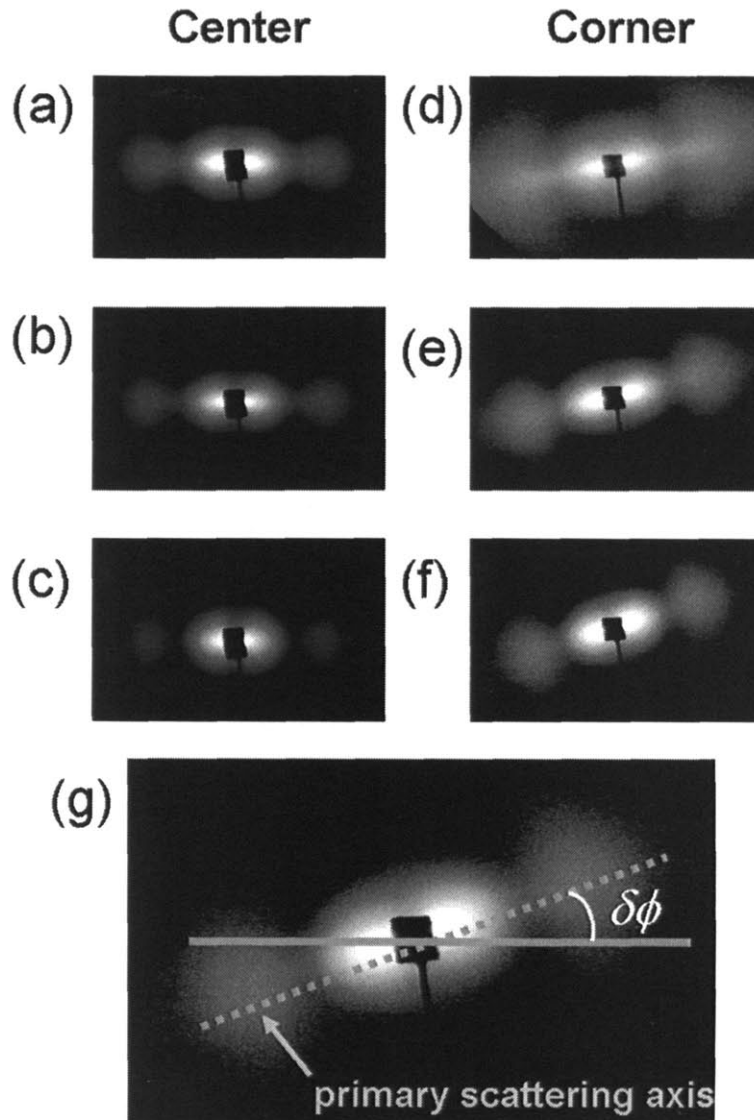
Figure 4-2. 2-D SAXS patterns for Sample 1 with the SAXS beam passing through the center of the film at (a) $h = 0.9$ mm, (b) $h = 0.5$ mm, and (c) $h = 0.3$ mm. 2-D SAXS patterns for Sample 1 with the SAXS beam passes through the corner of the film at (d) $h = 0.9$ mm, (e) $h = 0.5$ mm, and (f) $h = 0.3$ mm. (g) The primary scattering axis is defined by the dotted gray line and $\delta\phi$ is defined by the angle between the primary scattering axis and $\phi = 0$ degrees.
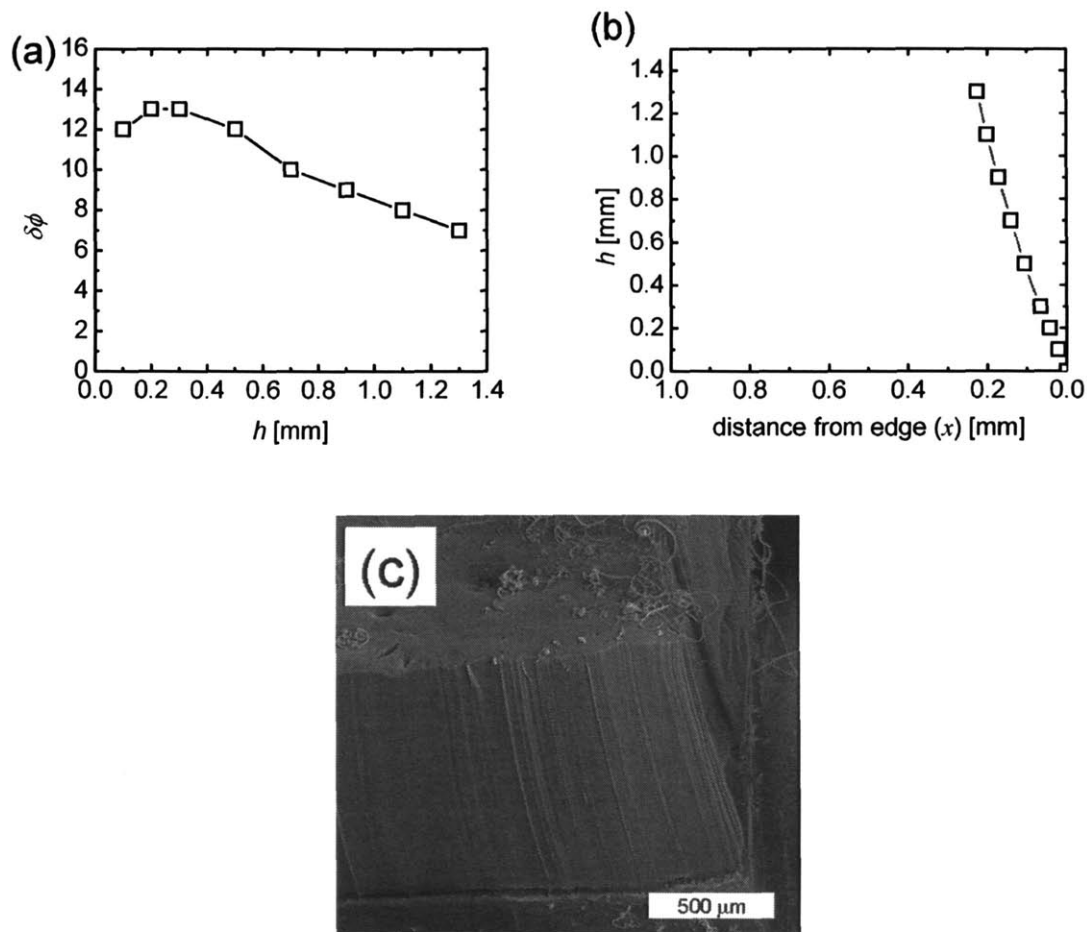
Figure 4-3. (a) $\delta\phi$ versus h shows the local orientation of CNTs near the corner, relative to the substrate. (b) The shape of the CNTs at the corner can be recreated from the values of $\delta\phi$ and h using Equation 1. (c) SEM micrograph shows good correspondence with the recreated shape of CNTs from SAXS.

From the 2-D SAXS patterns, we measure the CNT diameter and orientation for two pristine MWCNT films, using a formalism developed in our previous paper (Wang *et al.* 2007). Figure 4-4a shows the measured CNT diameters as a function of h for Sample 1 and Sample 2. For both types of CNT films, CNT diameters near the corner were 7 percent smaller than CNT diameters through the center of the film, indicating that exterior growth yields smaller diameter CNTs than interior growth. It is well known that CNT diameters tend to correlate well to catalyst diameters, so this result suggests that there is spatial inhomogeneity in the catalyst substrate at the edges. Futaba *et al.* observed smaller (ca. 3%) spatial differences in the diameters of single walled CNTs in an extensive TEM study, comparing growth near the edges, corners, and in the

interior(Futaba *et al.* 2006). Here we observe that both interior and edge areas show larger CNT diameters at larger *h*, as previously noted(Wang *et al.* 2007). The orientation measured for edge growth is strong and comparable to interior growth, which we compare in Figure 4-4b, after adjusting for the rotation of the primary scattering axis.
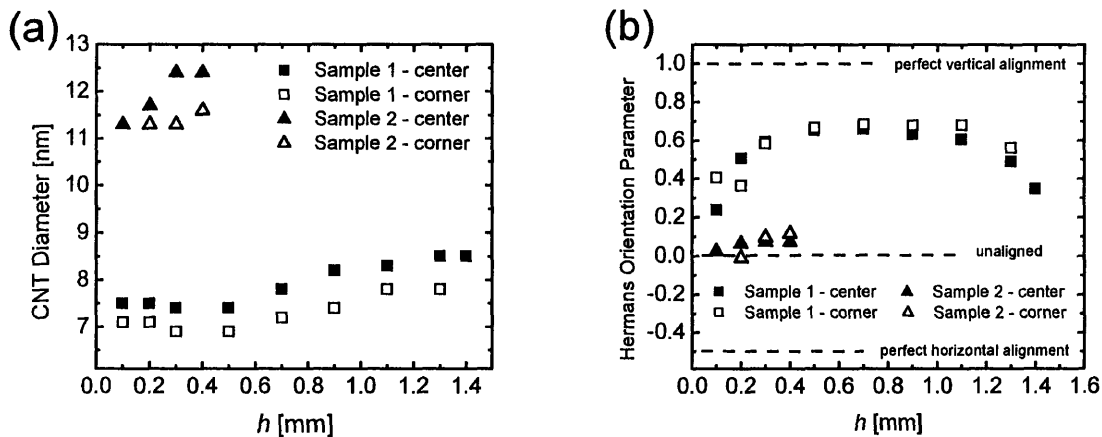
Figure 4-4. (a) CNT diameters and (b) Hermans orientation parameters obtained from SAXS intensities for Sample 1 and Sample 2 as a function of distance from the substrate (*h*).

We provide additional validation of smaller CNT diameters near the edge region. Sample 3a and Sample 3b are pristine MWCNT films that were prepared simultaneously; the only difference between the two samples is that Sample 3b is half as thin as Sample 3a [illustrated in Figure 4-1d. This has the effect of increasing the proportion of edge material in the beam path for Sample 3b. Results from CNT diameters measured from the two samples are shown in Figure 4-5a. Sample 4 is a pristine MWCNT film and we compare CNT diameters measured through the center of the film and along an edge of the film in Figure 4-5b. In both cases, we observe smaller CNT diameters in the edge region.

It is difficult to resolve differences between CNT diameters of interior and exterior growth from high resolution TEM; extraction of CNTs from different areas of the film would likely alter the native morphology. For SAXS however, samples are translated on a motorized stage and relative amounts of edge and interior growth are accessed non-destructively. We

summarize the results of these experiments in Figure 4-6 with a qualitative morphological map of a typical pristine MWCNT film.
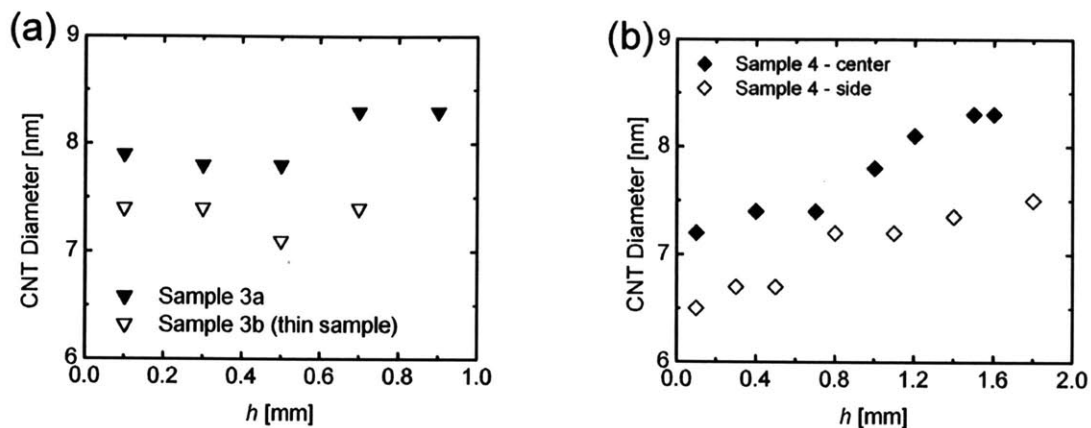
Figure 4-5. CNT diameters for (a) Sample 3a and 3b with the SAXS beam passing through the center of the films and (b) Sample 4 with the SAXS beam passing through the center and edge of the film. Sample 3b is a thin sample.
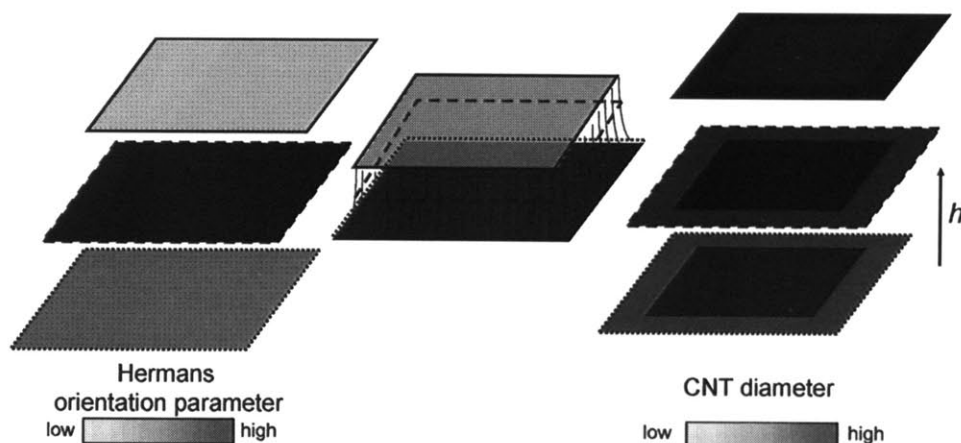
Figure 4-6. 2-D slices, illustrating qualitative spatial variation in orientation and CNT diameter of typical MWCNT films.

4.3.2. Morphology of uniaxially compressed films

We extend our morphological investigations to films that have been subjected to uniaxial compression. After compression, the thickness of Sample 5 is approximately 0.4 mm (~ 25% of

the original thickness). To make equivalent comparisons between pristine and compressed films, we define a normalized distance between detector and substrate:

$$h^* = \frac{h}{h_0} \qquad\qquad (4\text{-}2)$$

where h_0 is the full thickness of the pristine or deformed film. Figure 4-7a shows an illustration of the film before and after compression. SEM images detailing representative local morphology at the edges of Sample 5 at different values of h^* are shown in Figure 4-7b –d. The morphology of compressed Sample 5 is significantly different from that of the pristine precursor. At low values of h^* [see Figure 4-7c and d] there is noticeable alignment CNTs appear to have responded to the compressive deformation by buckling. At higher values of h^* [see Figure 4-7b] the film is morphology is much more randomized with no evidence of any vertical orientation.
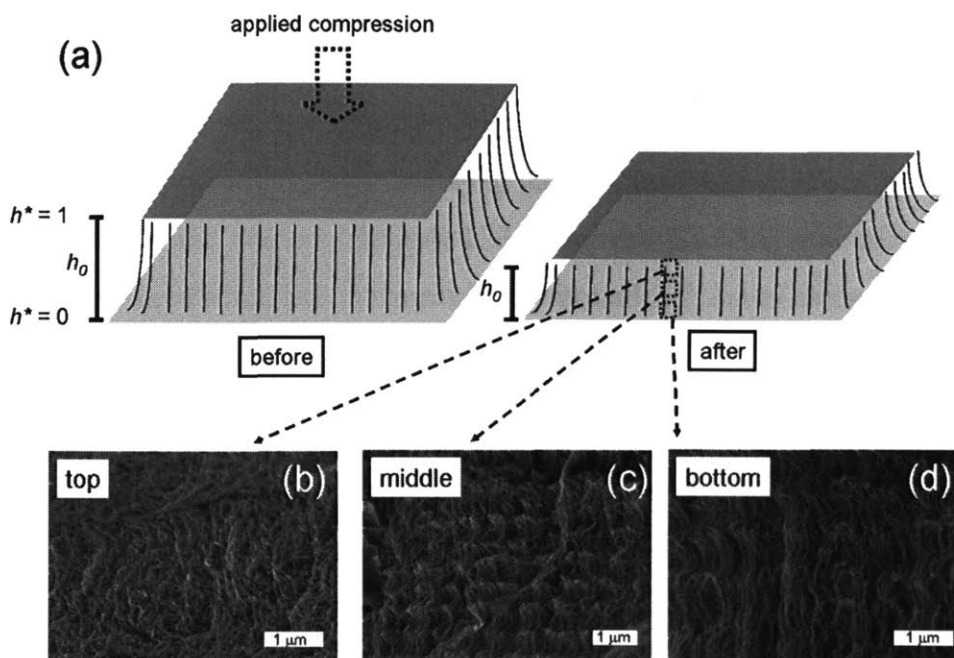
Figure 4-7. (a) Illustration of MWCNT film before and after uniaxial compression. SEM micrographs of compressed Sample 5 are shown at (b) at $h^* = 0.8$, (c) at $h^* = 0.5$, and (d) $h^* = 0.2$

2-D SAXS patterns for Sample 1 and Sample 5, shown in Figure 4-8a –d, reveal the presence of extensive horizontal orientation in the uniaxially compressed film. Figure 4-8e shows azimuthal variation in intensities at $q = 0.96$ nm^{-1}. It is noteworthy that the scattering intensity in the regions near $\phi = 0$ and $\phi = 180$ degrees for Sample 5 at $h^* = 0.5$ is non-zero which is indicative of vertical alignment. The simultaneous vertical and horizontal alignment suggests that uniaxially compressed CNT films deform primarily by buckling. Cao *et al.* have previously observed similar wave-like buckling in compressed MWCNT films (Cao *et al.* 2005). The Hermans orientation parameter is plotted in Figure 4-8f as a function of normalized height.

Figure 4-9a shows scattering intensities as a function of the scattering angle q. The compressed Sample 5 shows a peak at $q \sim 1.0$ nm^{-1} that is significantly broadened compared with undeformed Sample 1. We believe this broadening results from a greater polydispersity in CNT diameter in the detection region; the larger diameter CNTs near the top are compressed into the same region with CNTs of smaller diameter towards the bottom of the film, and the scattering experiment captures the resulting broader overall size distribution. Figure 4-9b shows that measurements of CNT diameters at all values of h^* are essentially the same for Sample 5, and it is satisfying that these values fall approximately in the middle of the range of CNT diameters obtained on the undeformed precursor Sample 1. In summary, SAXS characterization of both the orientation and CNT diameter is robust despite the deformation induced changes in the macroscopic structure of the film.
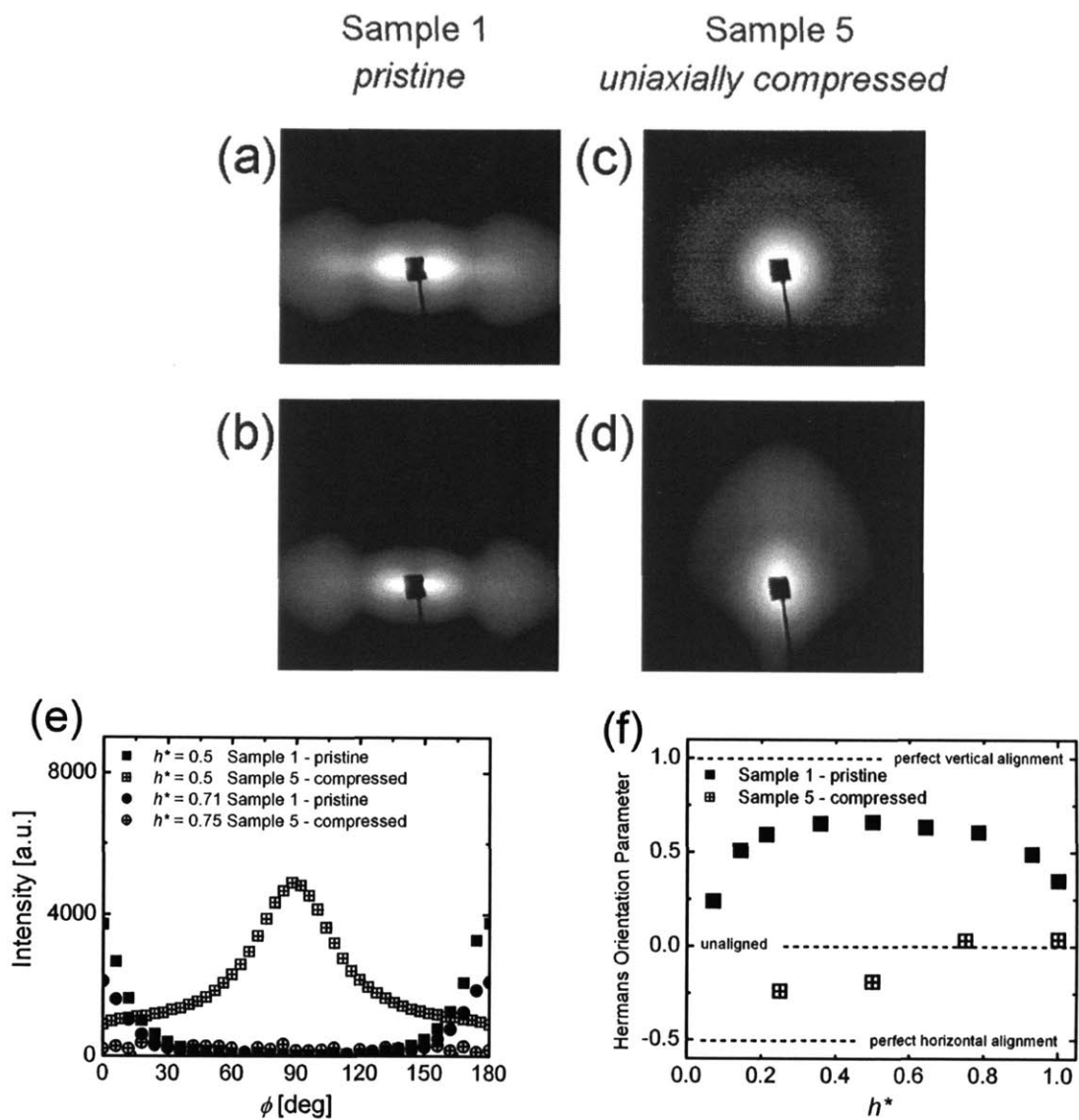
Figure 4-8. **2-D SAXS images of Sample 1 at (a)** $h^* = 0.71$, **(b)** $h^* = 0.5$ **and Sample 5 at (c)** $h^* = 0.75$ **and (d)** $h^* = 0.5$. **(e) Azimuthal variation in intensity of the 2-D SAXS patterns at** $q = 0.96$ nm^{-1} **(f) Hermans orientation parameter for Sample 1 and Sample 5 as a function of** h^*.
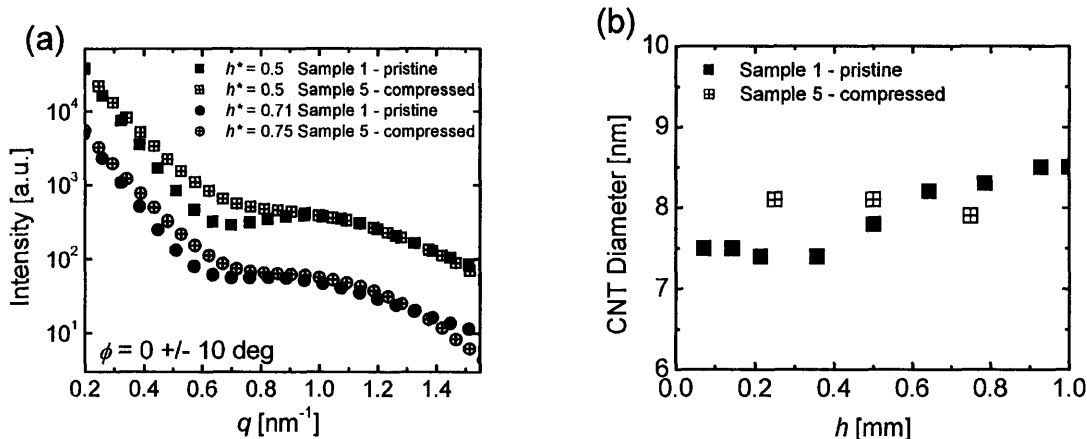
Figure 4-9. (a) SAXS intensities comparing Sample 1 and Sample 5 at comparable values of *h** and (b) corresponding measured CNT diameters

4.3.3. Morphology of cellular foams made by capillarity-induced densification

Another method of changing the morphology of CNT films is to use capillarity-induced densification. This process consists of wetting a CNT film with a liquid followed by the evaporation of the liquid to dryness at ambient conditions (Chakrapani *et al.* 2004; Fan *et al.* 2004; Futaba *et al.* 2006). During the evaporation process capillary forces bring neighboring CNTs closer together until the film is dry, resulting in a locally-densified CNT film. The CNTs are tethered to the catalyst substrate while the tips of the CNTs are unconstrained; as a result, the dried CNT film morphology consists of protruding tent-like ridges separated by flat regions of horizontally aligned CNTs as illustrated in Figure 4-10a (Chakrapani *et al.* 2004). CNTs at the top of the ridges are expected to show significant densification giving rise to a spatial variation in CNT density with *h**. This is demonstrated in the SEM micrograph of a ridge shown in Figure 4-10b.
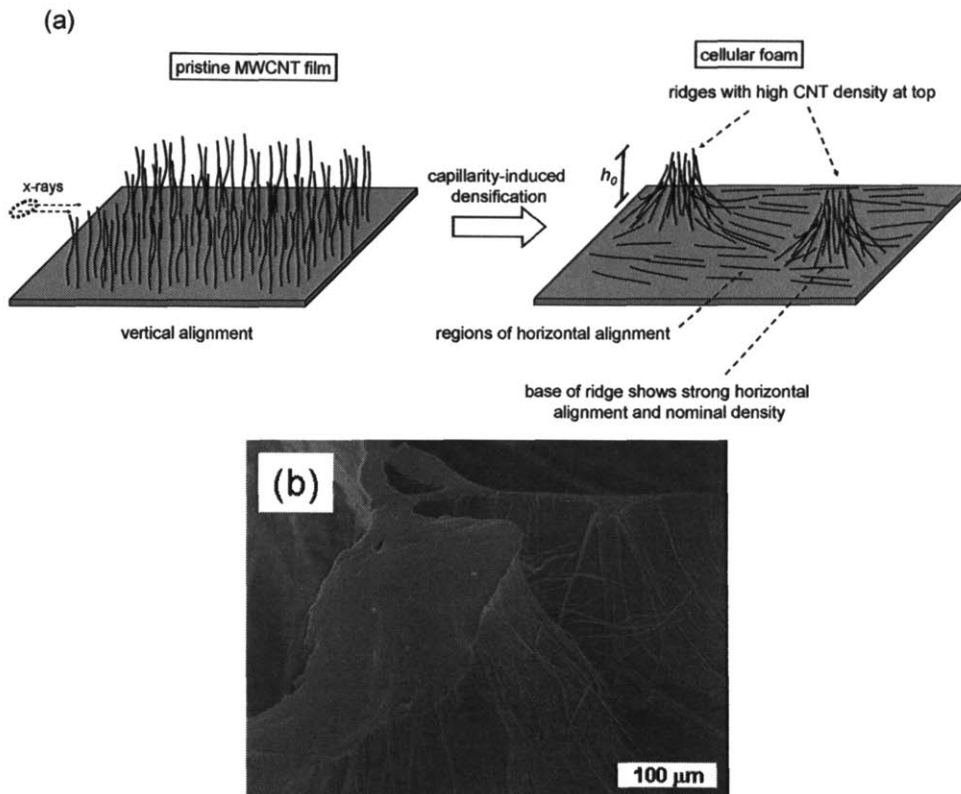
Figure 4-10. (a) Illustration of the process of capillarity-induced densification and general structure of cellular foam made from a MWCNT film. (b) SEM micrograph of a ridge from Sample 6.

2-D SAXS patterns obtained at different values of h^* are shown in Figure 4-11a–d for Sample 6 which was produced by processing a Sample 1 pristine film through an ethanol wetting/evaporation cycle. The Hermans orientation parameter is plotted in Figure 4-11e. As expected we observe some horizontal orientation near the substrate and moderate vertical alignment throughout the rest of film. Measured values for average CNT diameters in Sample 6 are 7.7 nm and approximately invariant with h^*. Figure 4-11 shows the SAXS intensities as a function of q for various values of h^* for Sample 6. We observe a noticeable and systematic increase in the intensities in the region of $q \sim 0.6$ nm^{-1}, with increasing h^*; the minimum in the scattering curve that is so apparent for pristine Sample 1 (bottom curve) disappears as h^* increase in the alcohol-treated Sample 6. We believe that this trend arises from the significantly closer spacing between neighboring CNTs at the top of the ridges in Sample 6, corresponding to an increase in packing density of CNTs.
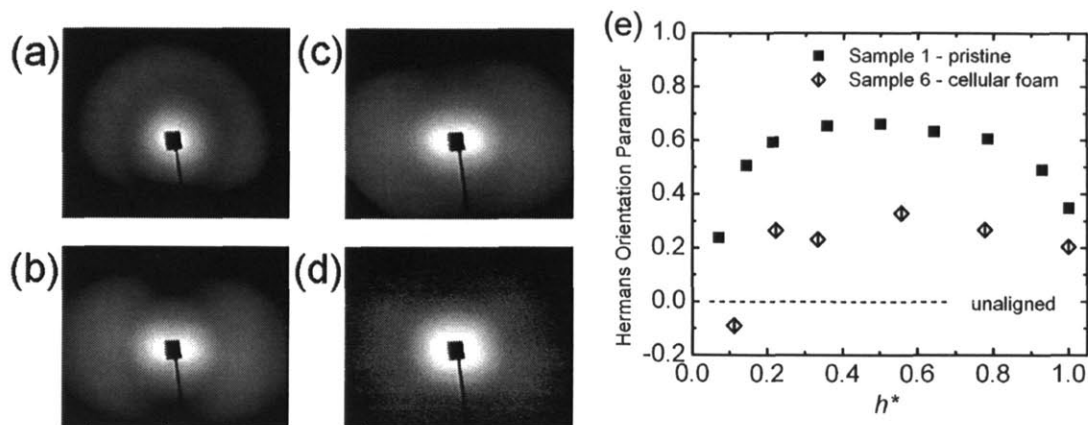
Figure 4-11. 2-D SAXS patterns for Sample 6 at (a) $h^* = 0.2$, (b) $h^* = 0.5$, (c) $h^* = 0.8$, and (d) $h^* = 1.0$. (e) Hermans orientation parameter comparing pristine Sample 1 and Sample 6, a cellular foam.
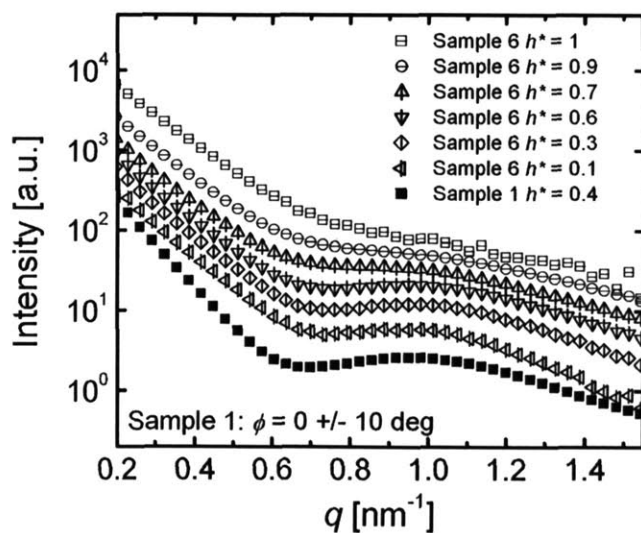
Figure 4-12. SAXS intensities of a cellular foam, Sample 6, at different values of h^*. SAXS intensity of Sample 1 at $h^* = 0.4$ included for comparison.

SAXS intensities are typically expressed as:

$$I(q) = AF(q)S(q) \tag{4-3}$$

where A is a constant which accounts for experimental considerations, $F(q)$ is the form factor for individual particle scattering, and the structure factor, $S(q)$, for scattering that results from inter-

particle interference. $S(q)$ provides information about spacing between CNTs while $F(q)$ is used in determining CNT diameters in the MWCNT films (Wang *et al.* 2007). To this point, the scattering from our CNT films could be represented adequately with the form factor $F(q)$ alone, owing to the fact that CNT-CNT separation distances in all of our pristine films are large enough to push any measurable inter-particle interference scattering to lower q, beneath the experimental range (beam stop) of our experimental setup. However, in the case of the CNT cellular foam (Sample 6), the local-density increases significantly as h^* increases, bringing inter-particle scattering into our experimental window, requiring a more complete analysis that includes a consideration of $S(q)$.

Oster and Riley developed an expression for the structure factor for cylinders aligned perfectly perpendicular to the SAXS beam, with arbitrary distances between neighbors (Oster and Riley 1952):

$$S(q) = 1 - v\pi s^2 \left(\frac{2J_1(qs)}{qs} \right) \qquad (4\text{-}4)$$

where q is the scattering angle, v is the in-plane number density of cylinders, s is the separation between cylinder centers, and J_1 is the modified spherical Bessel function of the first kind. A representative case for this mechanism of scattering is illustrated in Figure 4-13a, for a particular value of cylinder center-to-center spacing, $s = 12$ nm. In Figure 4-13b we use Equation 4 to illustrate two limiting and a few intermediate cases that are relevant to the observations we have obtained on Sample 6. At one extreme, the lower limit for separation is defined by hard contact between nearest neighbors, which results in a minimum value for s of 7.7 nm, or the average diameter of a single MWCNT in the sample. At the extreme of large separations, we use previous measurements of the areal density ($\sim 1 \times 10^{10}$ CNTs/cm^2) (Hart and Slocum 2006) in the films which leads to an estimate of a center-center spacing of ~ 80 nm. Figure 4-13b shows that for $s = 80$ nm, the primary peak of the structure factor affects the scattering intensity at very low q, well below the threshold of the beam stop, as discussed above. As the selected value of s decreases the primary peak shifts to higher q. At $s \sim 8 - 12$ nm the primary peak of the structure factor is located exactly in the region of the above mentioned minimum in the scattering curves

at $q \sim 0.6$ nm^{-1}. Thus the structure factor associated with CNT densification at the top of the ridges of the morphology of Sample 6 is the source of the additional SAXS intensity that leads to the disappearance of the shallow trough at scattering angles near $q \sim 0.6$ nm^{-1}.
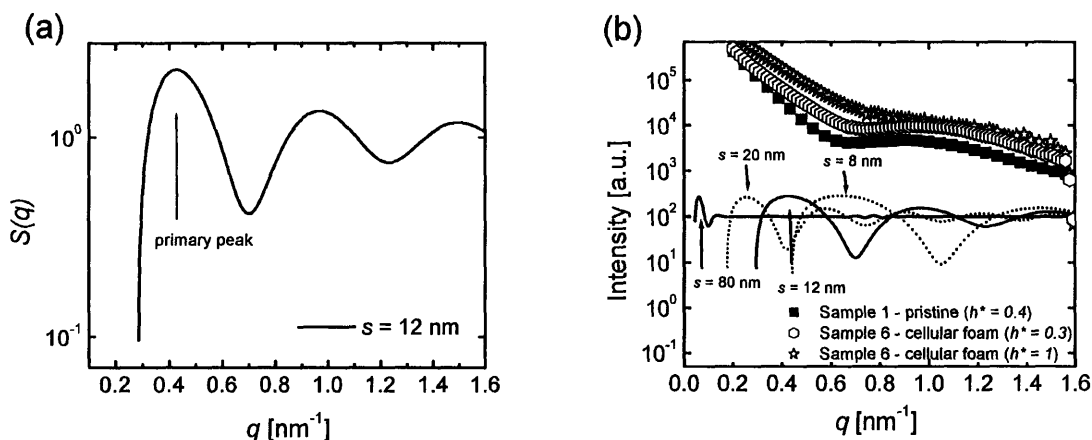
Figure 4-13. (a) Example of $S(q)$, calculated from Equation 4-4, with $s = 12$ nm. (b) Experimental SAXS intensities and $S(q)$ calculated using four selected values of s. The value of 80 nm corresponds to the typical CNT spacing for these films estimated previously while the value of 8 nm corresponds to the case at which the CNTs are in physical contact with each other.

To confirm that the increase in low q scattering with $h*$ corresponds directly to densification, we examine time-resolved SAXS intensities of the film, obtained during evaporation of the solvent *in-situ*. In this case SAXS data are collected concurrently with the local densification of the film at a fixed value of h. The densification process takes place as the ethanol evaporates from the wetted film over a time scale of about 5 minutes while the high intensity of the synchrotron radiation enables us to capture a full 2-D SAXS patterns in less than 5 seconds. Only a small reduction in h_0 occurs during evaporation of the solvent effectively keeping $h*$ constant. The SAXS intensities from Sample 7 are shown in Figure 4-14a as a function of time at $h* = 0.4$. Corresponding SAXS intensities, taken after evaporation of ethanol was complete (t > 20 minutes), for Sample 7 as a function of $h*$ are shown in Figure 4-14b. In both the time-resolved case and the height-resolved case we observe the previously discussed increase in SAXS intensities. In this manner we confirm that the systematic increase in low q intensities corresponds to increasing local areal density of the CNTs with time.
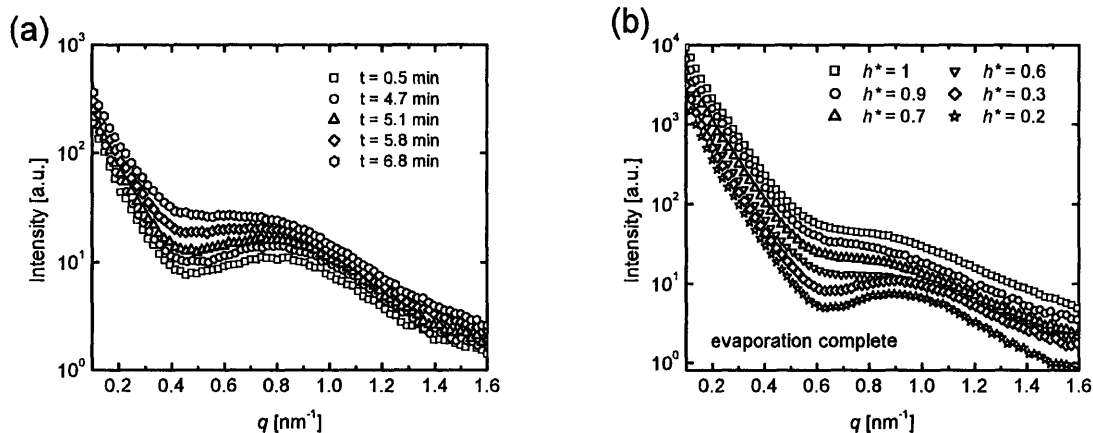
Figure 4-14. SAXS intensities of Sample 7, measured *in-situ* during the formation of a cellular foam as a function of (a) time ($h^* = 0.4$) and (b) height ($t > 20$ minutes).

From the *in-situ* SAXS data we examine the orientation of the film during the process of densification at two different values of h^*, as shown in Figure 4-15. Sample 8 was examined at $h^* \sim 0.9$ for comparison with the data obtained at $h^* = 0.4$ for Sample 7. For the experiments on Sample 8 we decreased the rate of evaporation by suspending a piece of bare Si wafer just above the film. The data at $h^* = 0.4$ indicates that the strong alignment close to the substrate is lost precipitously as evaporation proceeds. The data at $h^* = 0.9$ indicates the opposite trend, where orientation at the top of the film increases sharply. These observations are consistent with the physical picture of ridge formation with strong vertical alignment near the top and a wide distribution of orientations at the base. Our time-resolved information on CNT orientation and density confirm the prior observations of Chakrapani *et al.*, based on optical microscopy experiments, that large rearrangements in the structure of the film only occur during the latter stages of the densification process (Chakrapani *et al.* 2004).

Previous methods for measuring the areal density of CNT films or distances between neighboring MWCNTs have primarily relied on accurately determining the mass of CNTs on a substrate and the areal coverage of CNTs by extensive electron microscopy experiments (Bennett *et al.* 2006; Futaba *et al.* 2006; Hart and Slocum 2006). Futaba *et al.* have shown that attenuation of an x-ray beam through a densified film of SWNTs could yield the mass density (Futaba *et al.* 2006). However these methods require measurement of the mass density and

assumption of a homogeneous spatial distribution of CNTs. The analysis of the SAXS structure factor provides a location-specific estimate of the spacing between CNTs and an alternative method for characterizing the packing density of CNTs in a film.
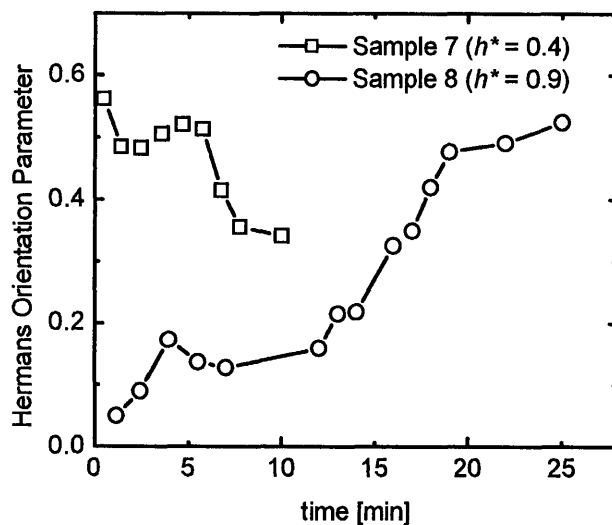
Figure 4-15. Real-time Hermans orientation parameter measured *in-situ* at different fixed values of *h**.

4.4. Conclusions

We used a SAXS methodology developed in a previous paper to study the morphology of pristine and mechanically manipulated MWCNT films. We determined that CNT diameters measured near the edges of a film were smaller compared to the CNT diameters measured in the interior. We also found that uniaxially compressed films deform by buckling, a result that was corroborated by the results of both SEM and SAXS experiments. We measured CNT diameters on a compressed film and found excellent correlation with the results from measurements on pristine films but we did not observe any variation in CNT diameter with distance from substrate for the case of the compressed film. We studied SAXS intensities from CNT cellular foams formed by capillarity-induced densification and found local densification of the structure is captured by the form of the SAXS data. Quantification of an additional low q scattering

mechanism in the densified materials was accomplished through the use of a structure factor for aligned cylinders with an 8 – 12 nm spacing between the cylinder axes. We confirmed this result by studying the morphology of densified CNT films with SAXS *in-situ.*

Overall we demonstrated that SAXS can provide quantitative, spatially-resolved information on deformation-induced structural alterations in CNT films. We anticipate that future investigations of the mechanical characteristics of MWCNT films under various manipulations will take advantage of synchrotron SAXS to provide complementary information that might be inaccessible in traditional microscopy studies of these materials.

4.5. Acknowledgements

5. EXTENSIONAL RHEOLOGY OF PMMA/METHACRYL-POSS COMPOSITES

The shear rheology of PMMA blended with methacryl functionalized polyhedral oligomeric silsesquioxane (mPOSS) nanoparticles has been well characterized by Kopesky *et al.* (Kopesky *et al.* 2005). We extend the previous work by examining the extensional rheology of blends of mPOSS with two different molecular weight PMMAs. For the case of a uniform dispersion of mPOSS in the PMMA matrix, we demonstrate that data from low-strain rate transient uniaxial extension matches well with linear viscoelastic (LV) data and high-strain data at high Deborah numbers give rise to plasticization of the PMMA matrix. For blends beyond the mPOSS-PMMA miscibility limit, the presence of a percolated network of phase-separated mPOSS gives rise to a large enhancement in the extensional viscosity of the blends, significantly larger than expected from LV data. Stress relaxation following cessation of extension experiments demonstrated accelerated relaxation of stress in PMMA due to the presence of mPOSS, and a long relaxation time plateau due to the presence of the secondary mPOSS-rich phase. We use WAXS in attempts to determine changes in the morphology and miscibility of mPOSS in PMMA during extension, but the results were inconclusive.

5.1. Introduction

Polyhedral oligomeric silsequioxanes (POSS) molecules have attracted recent interest as nanoscopic fillers for commercially relevant materials such as poly(methyl methacrylate) (PMMA) (Kopesky *et al.* 2004; Kopesky *et al.* 2005; Kopesky *et al.* 2006; Kopesky *et al.* 2006), poly(vinyl chloride) (PVC) (Soong *et al.* 2006), and polyethylene (PE) (Joshi *et al.* 2005). The corners of the silica oxide cages can be tethered to a variety of functional R- groups making the incorporation of POSS molecules into a polymeric matrix flexible. A diverse library of chemical moieties is commercially available and with the careful selection of the appropriate R-group it is straightforward to enhance or decrease interactions with the macromolecular matrix, thereby controlling the dispersion of the POSS in the matrix. Using the reactive functionalities of the R-groups, POSS can be incorporated into the polymer backbone, allowing the creation of POSS-

copolymers (Romo-Uribe *et al.* 1998; Kim *et al.* 2002; Kopesky *et al.* 2004; Liu and Zheng 2005; Turri and Levi 2005; Kim and Mather 2006; Ciolacu *et al.* 2007).

The thermal, mechanical, morphological and rheological behavior of POSS-polymer composites have been investigated thoroughly. Kopesky *et al.* (2004, 2005) and Joshi *et al.* (2005) have demonstrated that the incorporation of POSS into a homopolymer gives rise to a reduction in shear viscosity until the miscibility limit is reached and that further addition of POSS results in a secondary POSS-rich phase accompanied by an increase in shear viscosity, η, or the storage modulus G'. An extensive characterization of the linear viscoelastic properties of POSS-PMMA nanocomposites by Kopesky *et al.* resulted in a conceptual framework for understanding the molecular-level interactions between filler and matrix (Kopesky *et al.* 2004; Kopesky *et al.* 2005; Kopesky *et al.* 2006). For the case of a non-crystallizeable methacryl functionalized POSS cage mixture (mPOSS) blended with PMMA, they demonstrated that the increase in free volume associated with addition of POSS was responsible for the plasticization of PMMA (Kopesky *et al.* 2005).

These rheological studies have provided greater guidance for processing as well as a fundamental understanding regarding the improvement of mechanical properties of POSS-PMMA nanocomposites. However common polymer processing techniques, such as injection molding and extrusion, typically expose fluids to high strain, extensional flows; thus it is useful to measure the elongational properties of POSS-PMMA composites. To date there has been little characterization of the rheology of POSS-PMMA nanocomposites in extensional field-flows in the literature. The recent development of a novel extensional viscosity testing device, the SER Universal Testing Platform (SERUTP), has greatly reduced the amount of material and the setup time required to perform extensional viscosity experiments on melts (Sentmanat 2004). The SERUTP has been shown to obtain sensitive measurements of extensional rheological material functions which show excellent agreement with existing studies of linear and highly branched polyethylenes (Sentmanat *et al.* 2005). Because the SERUTP relies on the host instrument's control, it can be used in either controlled-strain or controlled-stress modes, giving rise to a wide range of experimental modes including transient stress growth, relaxation upon step-strain, and extensional creep experiments.

In this chapter, we use the SERUTP to characterize the behavior of two PMMA-mPOSS composites in uniaxial extension. We compare the results for transient extensional stress growth functions with data generated from a relaxation spectrum obtained from linear viscoelastic properties measured from small-amplitude oscillatory shear. We explore the enhancement in extensional viscosity due to the presence of a physical network of phase-separated mPOSS. We perform stress relaxation experiments to illustrate that mPOSS accelerates the relaxation of PMMA chains even at concentrations above the miscibility limit of mPOSS in PMMA, suggestive of an increased miscibility limit under applied strain. We use wide-angle X-ray scattering to identify a broadening of the peak associated with phase-separated mPOSS. This is suggestive of increased miscibility but is not substantively conclusive.

5.2. Experimental Methods

5.2.1. Preparation of methacryl POSS – PMMA nanocomposites

Poly(methyl methacrylate) (PMMA) pellets (Atofina Chemicals – Plexiglas V920 [PMMAV920] and Plexiglas V052 [PMMAV052]) were mixed with methacryl POSS cage mixture (Hybrid Plastics) at various volume fractions. Two methods of processing were used; for low loadings of methacryl POSS, finely ground PMMAV920 pellets were mixed with methacryl POSS cage mixture and either passed through a twin-screw extruder (ThermoHaake PRISM or DACA instruments) at $T = 200^{\circ}C$ with a residence time of around five minutes, and pelletized. A second method was employed for both PMMAV920 and PMMAV052; the blends were dissolved into THF at approximately 10 wt% at room temperature and the solutions were poured into a Teflon Petri dish and allowed to evaporate for 48 hours at 110 degrees C in a vacuum oven. From both processes, samples were then compression molded in a Carver Press into either rectangular samples (18 mm long, 12.7 mm wide, 0.25 – 1 mm thick) for the SERUTP or rheology discs (25 cm in diameter and 2 mm thick) at 190 degrees Celsius. The molded samples were then allowed to dry in a vacuum oven at $T = 85^{\circ}C$ over the course of several days.

5.2.2. X-ray scattering

2-D wide-angle x-ray scattering (WAXS) patterns were obtained using the WAXS image plate feature of a small-angle x-ray scattering system (Molecular Metrology, Northampton, MA). The system uses a rotating anode source (Cu Kα λ = 0.1542 nm) operating at 45 kV and 0.66 mA. Sample to image plate distance was calibrated using a silver behenate standard (with a first order scattering vector, q = 1.076 nm^{-1} where q = $4\pi\,sin\theta/\lambda$ where 2θ is the scattering angle and λ is the wavelength) and determined to be 138.2 mm, with a pixel width of 0.1315 mm. Pinhole collimation was used to achieve a beamspot ~ 500 μm in diameter. Two-dimensional (2-D) detector images, corresponding to total x-ray impingement count, were analyzed using Polar Software (Ver 2.7.0, Stonybrook Technology and Applied Research, Inc., Stony Brook, NY). Intensities were corrected for background and offset for visual clarity.

5.2.3. Thermogravimetric Analysis (TGA)

Thermogravimetric analysis experiments were performed on a Q80 (TA Instruments). Samples between 5 -20 mg were placed in a Pt pan and equilibrated at T = 40 °C for 3 minutes. Samples were then heated at a rate of 10 °C/min to a final temperature of T = 800 °C. Representative TGA curves are shown in Figure 5-1. Final residual ash weight percentage at T = 800 °C for each sample is listed in Table 1.

5.2.4. Shear Rheology

Linear viscoelastic measurements were performed on an AR2000 stress-controlled rotational rheometer (TA Instruments). 25 mm Al parallel plates were used on above-mentioned samples with gap separations of approximately 2 mm. A range of temperatures (T = 150 - 210 °C) was used with time-temperature superposition (TTS) to generate the master curves shown in Figure 5-2 and Figure 5-3.
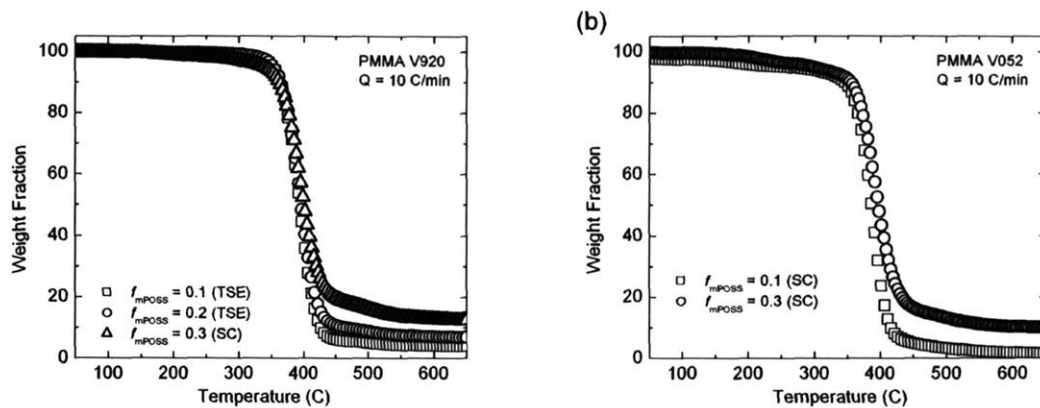
Figure 5-1. **TGA curves of mPOSS + PMMAV920 and (b) mPOSS + PMMAV052. All composites with mPOSS loadings have two plateaus beyond $T = 400\ ^oC$. We attribute the secondary decrease near $T = 450\ ^oC$ to the remaining decomposition of organics from the corner R- groups on the POSS cage. The final weight percentage, shown in Table 5-1 is reported is taken at $T = 800\ ^oC$**

Table 5-1. Weight fractions of mPOSS-PMMA nanocomposites measured by TGA

Sample Loading/ Name	Final weight fraction
$f_{mPOSS} = 0.1$ (V920 - TSE)	0.039
$f_{mPOSS} = 0.2$ (V920 - TSE)	0.069
$f_{mPOSS} = 0.3$ (V920 - SC)	0.125
$f_{mPOSS} = 0.1$ (V052 - SC)	0.014
$f_{mPOSS} = 0.3$ (V052 - SC)	0.100

5.2.5. Extensional Rheology

Extensional rheology experiments were performed on a SER Universal Testing Platform (Xpansion Instruments LLC) specifically designed for use as a detachable extensional rheometer fixture on commercially available torsional rheometer systems. The present study used the model SER-HV-A01 on both a TA/Rheometrics ARES rotation rheometer host platform in

112

controlled-strain mode. Tests were performed at $T = 170^\circ C$ for PMMAV920 system and at $T = 190^\circ C$ for the PMMAV052 system.

Linear viscoelastic envelopes (LVE) are provided concurrently with measurements of the transient extensional stress growth functions. We obtain the LVE from SAOS measurements by determining a 10-mode discrete shear relaxation spectrum, minimizing linear least squares error with experimental values for $G'(\omega)$ and $G''(\omega)$ as indicated by

$$\sum_{j=1}^{N}\left\{\left[\frac{G'(\omega_j)}{G'_j}-1\right]^2+\left[\frac{G''(\omega_j)}{G''_j}-1\right]^2\right\}^{1/2} \tag{5-1}$$

where N, is the number of data points, G'_j and G''_j are the experimental values of the storage and loss moduli respectively and $G'(\omega_j)$ and $G''(\omega_j)$ are the model values of the storage and loss moduli respectively (Bird et al. 1987). These properties are related to each relaxation time, λ_k, through

$$G'(\omega_j) = \sum_{k=1}^{10}\frac{\eta_k \lambda_k \omega_j^2}{1+(\lambda_k \omega_j)^2} \tag{5-2}$$

$$G''(\omega_j) = \sum_{k=1}^{10}\frac{\eta_k \omega_j}{1+(\lambda_k \omega_j)^2} \tag{5-3}$$

where η_k is the contribution for each relaxation time. The LVE can be calculated using η_k and ω_k using

$$\eta_E^+(t_j) = \sum_{k=1}^{10}3\eta_k \exp(-t_j/\lambda_k) \tag{5-4}$$

where $\eta_E^+(t)$ is the transient extensional stress growth function, t is time.

113
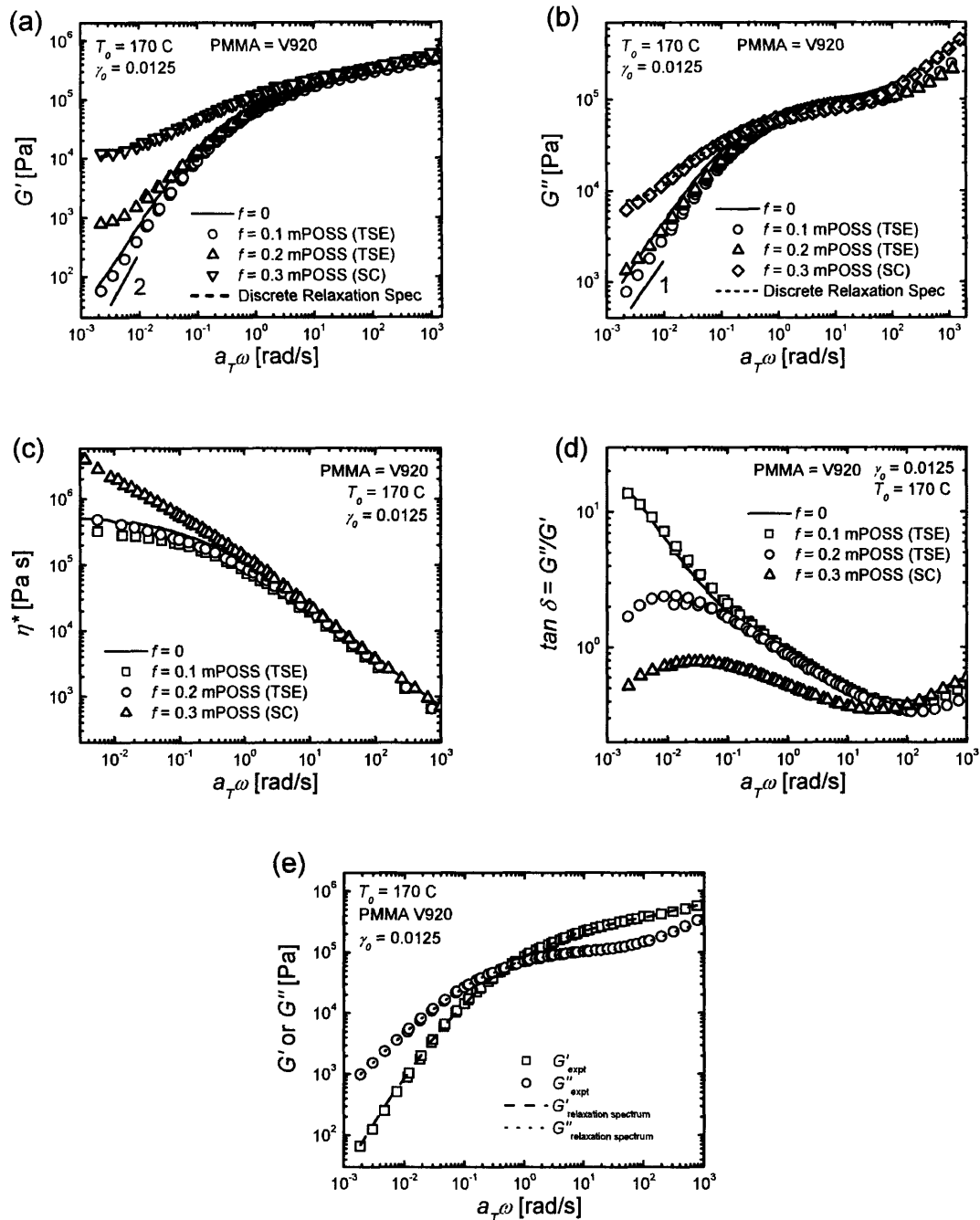
Figure 5-2. Linear viscoelastic properties of PMMA V920 + methacryl POSS (mPOSS): (a) storage modulus, G', (b) loss modulus, G'', with fit to discrete relaxation spectrum for 30% mPOSS-PMMA (c) complex viscosity, η^*, and (d) $\tan\delta$. f indicates weight fraction, TSE indicates twin-screw extrusion preparation and SC denotes solvent casting preparation. Panel (e) illustrates a best fit to discrete relaxation spectrum for PMMA V920.
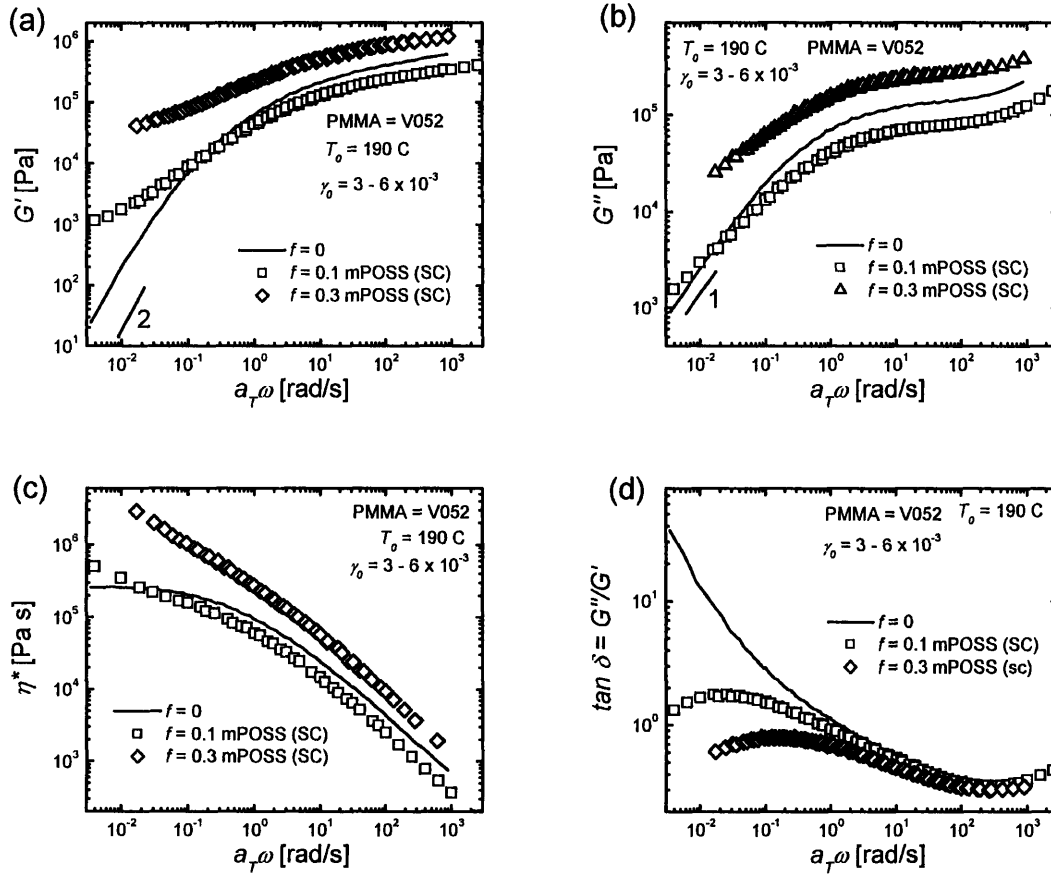
Figure 5-3. Linear viscoelastic properties of PMMAV052 + methacryl POSS (mPOSS): (a) storage modulus, G', (b) loss modulus, G'', (c) complex viscosity, η^*, and (d) $\tan \delta$. Notation is the same for Figure 5-2.

Table 5-2. Discrete relaxation spectrum parameters for PMMAV920 and PMMV052

k	λ_k [s]	PMMAV920 - η_k [Pa s]	PMMAV052 - η_k [Pa s]
1	10^{-4}	2×10^2	2×10^2
2	6×10^{-4}	1.2×10^2	1.2×10^2
3	3.6×10^{-3}	7×10^2	7×10^2
4	2.2×10^{-2}	2.1×10^3	2.5×10^3
5	0.13	1.7×10^4	2×10^4
6	0.79	7×10^4	6.8×10^4
7	4.7	2×10^5	1.2×10^5
8	28	1.7×10^5	4.9×10^4
9	170	6.8×10^4	0
10	1000	1.5×10^4	0

5.3. Results and Analysis

5.3.1. Linear viscoelastic properties from small-angle oscillatory shear (SAOS)

Data for the linear viscoelastic properties for PMMAV920-mPOSS composites are shown in Figure 5-2. We observe, in Figure 5-2a, the presence of a low frequency enhancement in G' with increasing incorporation of methacryl-POSS. At $f = 0.3$, we observe a distinct plateau which deviates significantly from the expected terminal slope of -2. Kopesky et al. (Kopesky et al. 2005) attributed this observation to thermally induced cross-linking of the vinyl moieties of the pendant methacryl groups between neighboring POSS molecules, which results in the formation of a weak, physical network. They determined that the limit of miscibility for the mixture of mPOSS cage mixture in PMMAV920 to be approximately 10 - 20% wt./wt. Beyond the miscibility limit, the mPOSS partitions into two phases: a homogeneous phase of molecularly dispersed mPOSS in the PMMA matrix and mPOSS-rich pools which have phase-separated from the bulk. The presence of the network of partially cross-linked pools can indeed give rise to an increase in G'. Figure 5-2c indicates that the complex viscosity of the sample $f = 0.3$ mPOSS, is

116

nearly an order of magnitude higher than for at $\omega = 10^{-2}$ rad/s but essentially the same as lower loadings of mPOSS or PMMA at $\omega = 10^2$ rad/s.

Following the procedure listed above, we obtain a discrete relaxation spectrum from the linear viscoelastic data to create the linear viscoelastic envelope for comparison with transient extensional stress growth measurements. An example of values for $G'(\omega)$ and $G''(\omega)$, obtained from a best-fit relaxation spectrum for PMMAV920 is shown in Figure 5-2e. The relaxation spectrum parameters are listed for both PMMA matrix materials in Table 5-2.

Data for the linear viscoelastic properties for PMMAV052-mPOSS composites are shown in Figure 5-3. Overall we observe similar behavior to the measurements of PMMAV920-mPOSS composites shown in Figure 5-2: for $f = 0.1$, we observe evidence of plasticization at low loadings and the presence of a plateau at frequencies lower than $\omega > 0.1$ rad/s. The plateau appears at a loading that is significantly lower than what is observed for the PMMAV920 mPOSS system. PMMAV052 has a higher molecular weight which results in a decreased miscibility between a polymer and a small molecule with increasing chain length. This arises from the loss in the configurational entropic contribution to the free energy of mixing as described by Flory (Flory 1953):

$$\Delta S_M^* = -k\left(n_{POSS}\ln v_{POSS} + n_{PMMA}\ln v_{PMMA}\right) \tag{5-5}$$

where k is Boltzmann's constant, n_{POSS} and n_{PMMA} are the number of POSS and PMMA molecules respectively and v_{POSS} and v_{PMMA} are the volume fractions of POSS and PMMA, respectively. As molecular weight increases, the value of n_{PMMA} decreases, ΔS_M^* decreases, and it becomes increasingly thermodynamically difficult to mix PMMA and m-POSS. At $f = 0.3$, we observe a large increase across the entire range of frequencies in the viscoelastic properties, which is a marked difference from the PMMAV920+0.3mPOSS blend which shows strong enhancement only at lower frequencies.

2

5.3.2. Transient uniaxial extension

Transient extensional viscosity growth function, $\eta_E^+(t)$, for mPOSS-PMMAV920

composites are shown in Figure 5-4 for (a) De << 1 and (b) De >> 1 where

$$\text{De} = \dot{\varepsilon}_H \tau_{PMMA} \tag{5-6}$$

and $\dot{\varepsilon}_H$ is the true Hencky strain rate and τ_{PMMA} is the longest relaxation time (typically

reptation) for PMMA. From the linear viscoelastic data in Figure 5-2, it seems reasonable to

estimate $\tau_{PMMA} \sim 3$ sec for PMMAV920 at $T = 170^\circ$ C. For the case of De << 1, exemplified by

Figure 5-4a, and loadings $f \leq 0.2$, we observe monotonically increasing curves for $\eta_E^+(t)$ with

time which appear to be invariant with loading of mPOSS. The data matches up well with the

LVE calculated from the discrete relaxation spectrum obtained from SAOS data. At a Hencky

strain of $\varepsilon_H \sim 0.1$, where the Hencky strain is defined by

$$\varepsilon_H = \dot{\varepsilon}_H t \tag{5-7}$$

the data exhibits an equilibrium value for $\eta_E^+(t) \approx 1.2 \times 10^6$ Pa s. This value is consistent with

the equilibrium value of the calculated linear viscoelastic envelope. Upon closer examination

the ordinal values of $\eta_E^+(t)$ which increase from blends $f = 0.1$ to $f = 0.2$ to $f = 0$, in good

correspondence with the ordinal increase in predictions from LV data. At a loading of $f = 0.3$

where two-phases exist concurrently, the curves for $\eta_E^+(t)$ show a significant increase over the

LVE over the entire experimental time-range. Indeed we observe the approximately order of

magnitude increase in $\eta_E^+(t)$ compared the expected value from LV data. The initial slopes of

the transient extensional viscosity growth function at $t < 0.3$ s are comparable for all the loadings.

However at subsequent time, the extensional viscosity growth for $f = 0.3$ continues to grow

geometrically while the curves for $f = 0$, 0.1, and 0.2 begin to reach an equilibrium value. At $t >$

10 s, the transient extensional viscosity growth function also appears to have reached an

equilibrium value. At $\varepsilon_H \approx 0.5$, η_E^+ for $f = 0.3$ is approximately 20 times that of the other

curves. This is slightly higher compared to the corresponding difference between the curves

from Figure 5-2c for $\eta^*_{10^{-2} \, rad/s}$ which shows an increase in value of ~ 5 at $t \approx 0.1$ s. This

comparison suggests that the presence of the mPOSS-rich secondary phase network is

responsible for the enhancement in extensional viscosities, well beyond what is predicted from

linear viscoelastic data.
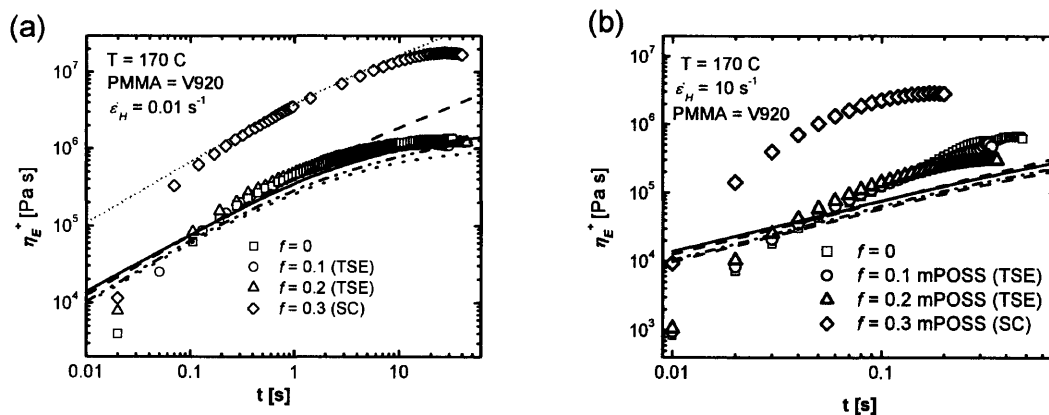
Figure 5-4. Transient extensional viscosity growth functions of mPOSS dispersed in PMMA V920 at (a) $\dot{\varepsilon}_H = 0.01$ s^{-1} (De << 1) and at (b) $\dot{\varepsilon}_H = 10$ s^{-1} (De >> 1). At low Hencky strain rates, addition of mPOSS to PMMA shows little effect. At $f = 0.3$, however, there is a large increase in η_E^+ across the entire range of time, corresponding to yield-like behavior. The increase is more pronounced at higher strains, as deformation of the physical network of phase-separated POSS pools exhibit an additional contribution to η_E^+. LVE curves, calculated from relaxation spectrum from linear viscoelastic, are shown as solid (—), dotted ($\cdots$), dash-dot-dot ($-\cdot\cdot$), and dashed lines ($---$) are for $f = 0, f = 0.1$, $f = 0.2$ and $f = 0.3$, respectively.

For the case of De >> 1, shown in Figure 5-4b, we observe slightly different behavior for

loadings beneath $f = 0.3$. The extensional viscosity growth function for $f = 0$ is higher than the

values expected from the linear viscoelastic envelope suggesting that PMMA V920 exhibits

extension induced hardening. Though PMMA consists of linear chains, rapid stretching,

corresponding to De >> 1, can give rise to strain hardening (Gramespacher and Meissner 1997).

At high Hencky strains, beyond $\varepsilon_H \approx 1$ we observe a mitigation of the hardening with increased

loading of mPOSS. This data suggests that the presence of mPOSS plasticizes the PMMA matrix at high strains. There is no correspondence between this behavior and the linear viscoelastic properties because the plasticization appears to occur well beyond the linear regime accessed by the SAOS experiments. For $f = 0.3$, we observe the large, order-of-magnitude enhancement in extensional viscosity that is also observed in the low rate data of Figure 5-4a.

The results for extensional viscosity growth functions at $T = 190^o$ C for mPOSS blended with PMMAV052 are shown in Figure 5-5. The higher temperature is used for PMMAV052 because of the higher molecular weight, and corresponding longer relaxation times and larger viscosities. In general, the curves show similar behavior to the results for PMMAV920, shown in Figure 5-4; however, as previously mentioned, the lower miscibility of mPOSS in PMMAV052 results in phase separation at loadings of $f = 0.1$. Thus for De $\ll 1$, as shown in Figure 5-5a, we do not observe the overlap in extensional viscosity growth curves at low loadings for PMMAV920; instead we observe a slight enhancement in the extensional viscosity for mPOSS in PMMAV052 at $f = 0.1$. The larger enhancement observed for $f = 0.3$, is expected because of the large volume fraction of mPOSS-rich secondary phase.

For $\dot{\varepsilon}_H = 1 \text{ s}^{-1}$, or De ~ 1, we observe evidence of plasticization across the entire range of times for $f = 0.1$. This is consistent with the results from examination of the complex viscosity at $\omega = 1 \text{ rad/s}$, as shown in Figure 5-3c. There is slight plasticization due to the presence of mPOSS at low loadings, which corresponds well with the results from SAOS, in Figure 5-3, followed by a large jump in the extensional viscosity for $f = 0.3$. In summary it is apparent that below the limit of miscibility, mPOSS plasticizes PMMA and the results correspond quite well with LV data, and the presence of a secondary phase gives rise to a dramatic increase in the extensional viscosity.
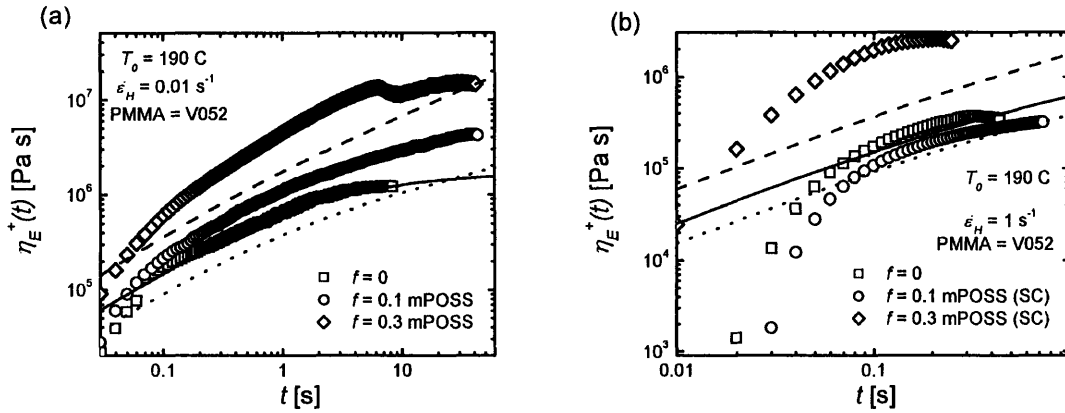
Figure 5-5. Transient extensional viscosity growth functions of mPOSS in PMMAV052 at (a) $\dot{\varepsilon}_H = 0.01 \text{ s}^{-1}$ (De $\ll$ 1) and at (b) $\dot{\varepsilon}_H = 1 \text{ s}^{-1}$ (De $\sim$ 1). Lines drawn represent LVE predictions from SAOS data and calculated discrete relaxation spectrum. Solid (—), dotted (·····), and dashed lines (- - -) are for $f = 0$, $f = 0.1$, and $f = 0.3$, respectively.

5.3.3. Relaxation following cessation of extension

The normalized stress relaxation function following cessation of extension of mPOSS-PMMA composites are shown in Figure 5-6a and Figure 5-6b for PMMAV920 and PMMAV052, respectively. PMMAV920-mPOSS samples were extended at $\dot{\varepsilon}_H = 1 \text{ s}^{-1}$ for $t =$ 0.3 s ($\varepsilon_H = 0.3$) at $T = 170^{\circ}$ C and PMMAV052-mPOSS samples were extended at $\dot{\varepsilon}_H = 0.1 \text{ s}^{-1}$ for $t = 1$ s ($\varepsilon_H = 0.1$) at $T = 190^{\circ}$ C , before the motor was fixed and the evolution of the torque was monitored. The results in Figure 5-6a illustrates how the presence of mPOSS plasticizes PMMAV920 at low loadings, and accelerates the relaxation of the stress of the polymer chains at low times. The inset graphs are magnifications of relaxation at small times. For the case of $f =$ 0.2, the stress relaxation curve appears to plateau beyond $t > 70$ s. Because a loading of $f = 0.2$ corresponds to a loading which begins to exhibit a secondary mPOSS-rich phase, we expect that the plateau corresponds to the contribution of stress from the deformation of the weak network of the secondary phase. From the linear viscoelastic data in Figure 5-2, the time scale related to the secondary phase is > 1000 s. This is more evident in Figure 5-6b for the case of $f = 0.3$ where there is a substantial contribution from the network formed by the secondary phase; the plateau in

the relaxation function reflects an elastic response with relatively little viscous dissipation. However, examining the data at very short times, including the data for $f = 0.3$, it appears that increasing amounts of mPOSS in the matrix monotonically accelerates the relaxation of polymeric chains. The inset graph shows that the stress relaxation function for $f = 0.3$ is steeper than for the functions for $f = 0.1$ and $f = 0$, at $t < 1$ s.
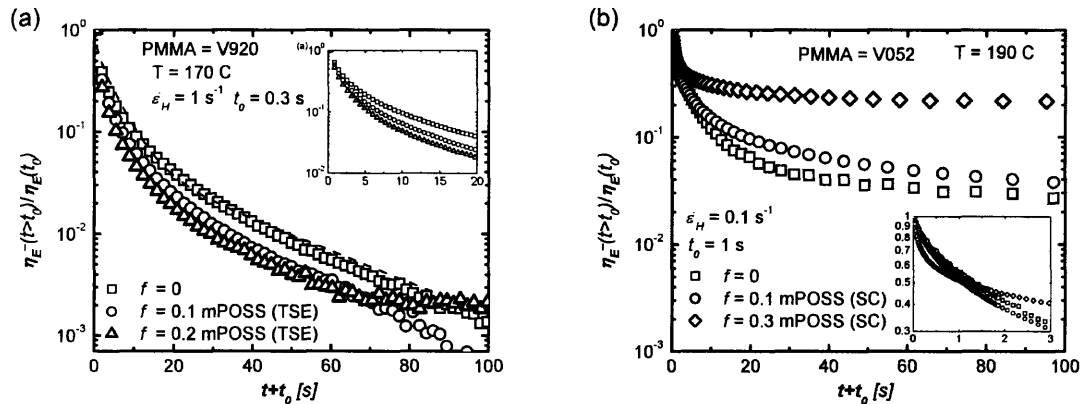
Figure 5-6. Stress relaxation functions following cessation of extension for (a) mPOSS in PMMA V920 at $T = 170^o$ C and (b) mPOSS in PMMA V052 at $T = 190^o$ C

It is an unexpected result that mPOSS accelerates relaxation of the matrix at loadings beyond the miscibility limit. Kopesky *et al.* showed that plasticization of PMMA by mPOSS was due to an increase in fractional free volume with increasing concentrations of mPOSS. (Kopesky *et al.* 2005) However their data indicated that the increase in fractional free volume ceased to increase beyond the miscibility limit of $\phi > 0.1 - 0.2$ for the same matrix of PMMA V920. Thus their data does not indicate the possibility for further accelerated relaxation beyond the miscibility limit.

It has been shown that flow can alter the miscibility of a two-component system (Silberberg and Kuhn 1952; Mazich and Carr 1983). Mazich and Carr demonstrated that control of the first normal stress difference of a blend of polystyrene and poly (vinyl methyl ether) in benzene under shear flow resulted in an increase in the lower critical solution temperature and a corresponding increase in the single-phase domain of the phase diagram. They attributed the increased miscibility to the contribution of additional strain energy from flow to enhancing the

free energy of the system. Though our system is different and involves a concentrated melt with a low loading of a small molecule solute, a similar concept prevails: additional strain energy may increase the solubility limit of mPOSS in PMMA. It is possible that the additional rapid relaxation following cessation of uniaxial extension for $f = 0.3$ mPOSS in V052 can be due to strain-induced increase in the miscibility limit of mPOSS in PMMA.

5.3.4. Wide-angle X-ray scattering

To confirm the hypothesis that there is a flow-induced increase in the miscibility of mPOSS-PMMA nanocomposites following extension, we compare WAXS intensities between extended and unextended regions of a sample. Kopesky *et al.* utilized WAXS to determine the presence of the mPOSS-rich phase in mixtures of mPOSS and PMMAV920. mPOSS is available as a non-crystallizable "cage-mixture" consisting of eight-, ten, and twelve-cornered POSS cages. Addition of mPOSS, beyond a limit of about 10% wt. into a matrix of PMMAV920, resulted in the appearance of several X-ray signatures in WAXS, which was consistent with the expected 'lattice' spacing between neighboring mPOSS cages in the mPOSS-rich phase. Further addition of mPOSS increased the intensity of the WAXS peak which, combined with their observations that the glass transition and fractional free volume measurements showed no further change, indicated that further addition of mPOSS partitioned to the secondary phase.

An example of extensional rheology sample after uniaxial extension is shown in Figure 5-7a, illustrating the "extended" and "no extension" regions where WAXS data are obtained from. Figure 5-7b illustrates a visual 'whitening' that occurs in the extended region above loadings of $f = 0.1$, suggestive of a change in the underlying morphology. WAXS patterns obtained from the two different regions are shown in Figure 5-8 for PMMAV920-mPOSS and PMMAV052-mPOSS as a function of loading. In general, WAXS patterns from the extended regions exhibit a slight broadening in the peak at $2\theta \approx 6.5^{\circ}$ and a slight decrease in the peak intensity, but overall the change in intensities is not significant. So though WAXS does not

provide a conclusively sensitive demonstration for the increased miscibility of mPOSS in PMMA during extension, it does provide some indication of its possibility.
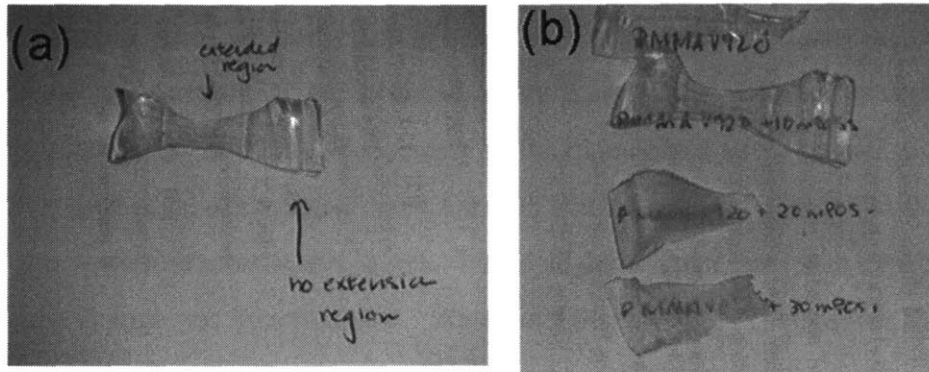
Figure 5-7. Extensional rheology samples uniaxial extension. (a) WAXS patterns from extended [center] and unextended regions [edge] of the sample are compared. (b) Samples with mPOSS loadings above 20% wt./wt. show visual opacity in the extended region, but remain relatively transparent in the unextended region.
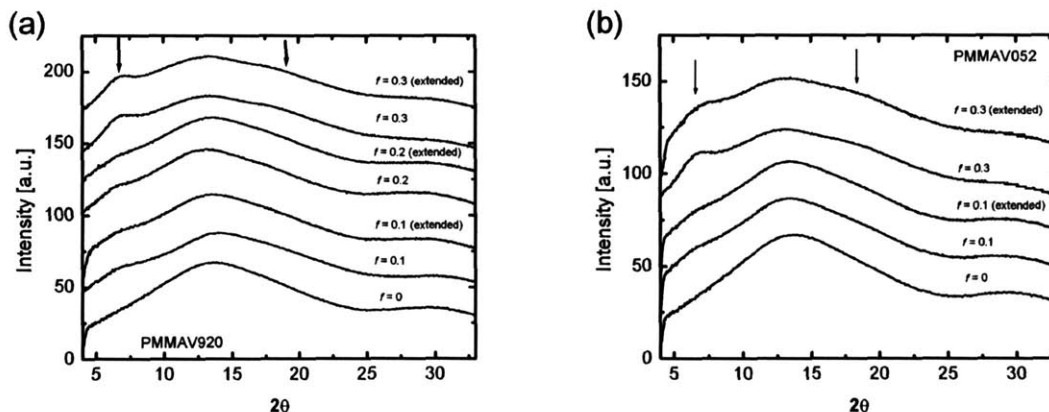
Figure 5-8. WAXS intensities from extended and unexteded regions for (a) PMMAV920-mPOSS and (b) PMMAV052-mPOSS.

5.4. Conclusions

We examined the rheological properties of two different molecular weight PMMAs blended with methacryl POSS in uniaxial extensional flow. We compared the results to linear viscoelastic measurements obtained from small amplitude oscillatory shear. The higher molecular weight PMMAV052 exhibited a lower miscibility with mPOSS as expected from the

free energy of mixing. For blends of homogeneous dispersions of mPOSS in PMMA, transient extensional stress growth at De << 1 of homogeneous mPOSS dispersed in PMMA showed little change with increased loadings, as expected from data from SAOS. For De >> 1, mPOSS acted to decrease the magnitude of strain-hardening in PMMA, effectively plasticizing the matrix at high strains. For blends containing a percolated network associated with the secondary mPOSS-rich phase, we observed significant enhancement in the extensional stress growth functions across the entire time-scale of the experiment for both PMMAV920 and PMMAV052 systems, compared to the linear viscoelastic envelopes. While slight enhancement was expected from the magnitude of the change was unanticipated. We expect that the large change was the result of "extensional hardening" due to the presence of the secondary phase

Relaxation of stress following cessation of extension experiments demonstrated that mPOSS accelerates the relaxation behavior of the PMMA matrix, in good correspondence with the work of Kopesky *et al.* who elucidated the fact that mPOSS generates additional free volume. For loadings which significantly exceed the miscibility limit of mPOSS and PMMA, we observed an accelerated initial relaxation for the PMMA, followed by a long relaxation time plateau that is attributed to the gel-like network of the secondary phase. We hypothesize that the faster relaxation is attributed to a flow induced increase in the miscibility of mPOSS in PMMA, which would result in an increase in fractional free volume. We attempted to use WAXS to determine the presence of the enhanced miscibility and observed that the peak related to the inter-particle spacing between aggregated amorphous mPOSS broadened and diminished slightly. Though the results from WAXS were not particularly conclusive, they were indicative of the possibility of flow-induced increase in the miscibility limit of mPOSS in a PMMA matrix. Further morphological analysis, perhaps using TEM or computer simulations, would be useful to determine the origin of the accelerated relaxation. Other rheological methods, including large amplitude oscillatory shear may provide an additional clarification of this effect.

5.5. Acknowledgements

125

6. EFFECT OF VOLUME FRACTION AND ASPECT RATIO ON THE RHEOLOGY OF PMMA-CLAY NANOCOMPOSITES FORMED BY EMULSION POLYMERIZATION

We examine the rheological properties of two different clay-filled PMMA nanocomposites synthesized by emulsion polymerization. Using WAXS, TEM and a formalism developed by Sheng *et al.* (2004), we determine the aspect ratio and volume fraction of the clay nanocomposites. We measure both the linear viscoelastic properties of the blends in small-amplitude oscillatory shear and study large-strain melt behavior by examining the extensional rheology. Using previously developed theories for both classical and percolated networks of high aspect ratio fillers, we demonstrate how our measurements of aspect ratio and volume fraction from morphological characterizations correspond well with experimental rheology data. Results from the uniaxial extensional rheology experiments indicated enhancement in extensional viscosity, due to increased loadings of clay, which corresponded well with Batchelor's theory at low strains. However the effect disappears at high strains with increased alignment of the clay platelets. Data from relaxation upon cessation of extension experiments indicate that clay platelets retard relaxation behavior, but are related to a process different from randomization by rotational diffusion.

6.1. Introduction

The dispersion of layered silicates, such as clay, into a polymeric matrix, results in the formation of nanocomposites with enhanced mechanical, barrier, and thermal properties (Jash and Wilkie 2005). Industrial applications that benefit from these improvements are already available. These advantages arise from the small nanoscopic dimension of exfoliated clay platelets. Indeed it is the large surface area to volume ratios and large aspect ratios that provide for the lower critical concentration, compared to classic fillers, for these improved properties to manifest (Manias *et al.* 2001).

The native morphology of polymer-clay composites typically consists of a coexistence of large agglomerates and exfoliated platelets (Vermogen *et al.* 2005) and the formation of a

homogeneous dispersion of clay platelets in polymer can be difficult. Several processing and synthesis methods have been explored with the goal of achieving a fully exfoliated morphology, by enhancing dispersion of a clay-polymer composite through mechanical breakup of tactoids by twin-screw extrusion or sonication (Okamoto *et al.* 1998; Tanoue *et al.* 2004; Zhao *et al.* 2005), enhancing clay-matrix interactions through the use of surfactants (Hoffman *et al.* 2000), or solution blending (Jeon *et al.* 2003; Jeon *et al.* 2004). The development of *in situ* emulsion polymerization and heterocoagulation polymerization methods (Huang and Brittain 2001; Xu *et al.* 2004) have greatly improved the dispersion of PMMA-clay nanocomposites.

Quantitative determination of the extent of dispersion is a challenge in of itself. The *de facto* techniques used to measure dispersion are transmission electron microscopy (TEM) and wide-angle x-ray scattering (WAXS). TEM provides a direct visualization of the morphology of the composite and it is straightforward to observe the presence of large, unexfoliated, tactoids (Vermogen *et al.* 2005). However TEM is a local technique with the field of view typically limited to a few hundred nanometers. Signatures from WAXS patterns correspond to both average separation between clay platelets (d_{clay}) and average tactoid size (t) using Bragg's Law and Scherrer's Equation, respectively. However imprecise measurements of peak breadth make it challenging to obtain exact values for t. Rheological methods have also been explored as a technique to quantify dispersion (Hoffman *et al.* 2000; Tanoue *et al.* 2004). Several studies of the shear rheology of clay-polystyrene (Tanoue *et al.* 2004; Zhao *et al.* 2005), clay-polypropylene (Okamoto *et al.* 2001; Koo *et al.* 2005; Vermogen *et al.* 2005), clay-poly(vinyl acetate) copolymer nanocomposites have indicated that a decrease in the scaling of G' in the terminal region, as well as transitions to lower cross over frequencies ω_c can be correlated to improved dispersion. Extensional rheology can be sensitive to the underlying structure but relatively few measurements of nanocomposites have been performed, including "2-D" clay fillers.

In this chapter we illustrate a framework to compare the rheology of clay filled PMMA synthesized by emulsion polymerization to theoretical predictions based on the morphological characteristics of clay filler volume fraction and aspect ratio. We begin by characterizing the morphology of two different clay filled PMMA composites to quantitatively determine average geometric properties of the filler using WAXS and TEM. We measure the rheology of the clay

composites using small-angle oscillatory shear measurements (SAOS) to examine the scaling behavior of the storage modulus, G', with volume fraction. We compare these results to the predictions of the Guth-Gold theory for classical rod-like fillers and a theory for a percolated network of high aspect ratio rods. We examine the rheology of the clay composites in transient uniaxial extension and demonstrate that enhancement due to the percolated network of clay platelets gives rise to enhancement in the extensional viscosity at low strains, consistent with Batchelor's theory for elongated rods.

6.2. Experimental Methods

6.2.1. Preparation of clay – PMMA nanocomposites

Poly (methyl methacrylate) (PMMA) - clay nanocomposites were synthesized using an emulsion polymerization technique, with details listed elsewhere (Huang and Brittain 2001), resulting in a coarse precipitate. Two different clays [larger width and length fluorohectorite (FH) and smaller laponite (LAP)] were incorporated into PMMA providing a two limiting cases of filler dimensions. The characteristics of each clay-filled PMMA are listed in Table 6-1

Table 6-1. Summary of clay filler properties

Clay Type	Abbr.	Platelet Dimensions – thickness x width (nm)	n	d (nm)	Aspect ratio (p)	$M_{W,PMMA}$ (x10^3 g/mol)
Laponite	LAP	30 x 1	1	1.26	~ 15 - 30	32[2]
Fluorohectorite	FH	> 300 x 1	5	1.68	~ 50 - 100	240

6.2.2. Wide-angle X-ray scattering

---

[2] The molecular weight of Laponite was measured after chain cleavage by electron-beam irradiation. Prior to chain cleavage, the M_w was approximately 1.23 x 10^6 g/mol.

2-D wide-angle x-ray scattering (WAXS) patterns were obtained using the WAXS image plate feature of a small-angle x-ray scattering system (Molecular Metrology, Northampton, MA). The system uses a rotating anode source (Cu Kα λ = 0.1542 nm) operating at 45 kV and 0.66 mA. Sample to image plate distance was calibrated using a silver behenate standard (with a first order scattering vector, q = 1.076 nm^{-1} where $q = 4\pi \sin\theta/\lambda$ where 2θ is the scattering angle and λ is the wavelength) and determined to be 138.2 mm, with a pixel width of 0.1315 mm. Pinhole collimation was used to achieve a beamspot ~ 500 μm in diameter. Two-dimensional (2-D) detector images, corresponding to total x-ray impingement count, were analyzed using Polar Software (Ver 2.7.0, Stonybrook Technology and Applied Research, Inc., Stony Brook, NY). Intensities were corrected for background and offset for visual clarity.

6.2.3. Transmission electron microscopy

TEM was performed on a JEOL 2000FX at 200 kV. Samples were microtomed (MT-χ Ultramicrotome) using a diamond knife into 50 nm cross-sections.

6.2.4. Thermogravimetric Analysis (TGA)

Thermogravimetric analysis experiments were performed on a Q80 (TA Instruments). Samples between 5 -20 mg were placed in a Pt pan and equilibrated at T = 40 °C for 3 minutes. Samples were then heated at a rate of 10 °C/min to a final temperature of T = 800 °C. We specify weight percentage for clays as the residual ash weight percentage at T = 800 °C. Representative TGA curves are shown in Appendix 10.2.

6.2.5. Electron-beam irradiation induced cleavage of PMMA

Samples of PMMA-LAP were treated with 20 MRads of ionizing radiation to reduce the molecular weight of the PMMA matrix by chain scission (Kudoh *et al.* 1996; Pionteck *et al.* 2000). See Appendix 10.2 for more details.

6.2.6. Shear Rheology

Linear viscoelastic properties were determined from SAOS measurements performed on an AR2000 stress-controlled rotational rheometer (TA Instruments). 25 mm Al parallel plates were used on above-mentioned samples with gap separations of approximately 2 mm. A range of temperatures ($T = 150$ - 210 $^{\circ}C$) was used with time-temperature superposition (TTS) to generate the master curves.

6.2.7. Extensional Rheology

Extensional rheology experiments were performed on a SER Universal Testing Platform (Xpansion Instruments LLC) specifically designed for use as a detachable extensional rheometer fixture on commercially available torsional rheometer systems. The present study used the model SER-HV-A01 on both a TA/Rheometrics ARES rotation rheometer host platform in controlled-strain mode. Tests were performed at $T = 190^{\circ}C$ for PMMA-FH samples and at $T = 160^{\circ}C$ for the PMMA-LAP samples.

6.3. Results and Analysis

We use the concept of an "effective particle" developed by Sheng *et al.* (Sheng *et al.* 2004) to determine the aspect ratio, $p = t/L$, of the oblate spheroidal, clay fillers. We calculate the thickness of the particle (t) with:

$$t = (N-1)d_{(001)} + d_s \qquad (6\text{-}1)$$

where N is the number of platelets in a tactoid, $d_{(001)}$ is the inter-platelet spacing, and d_s is the thickness of a single platelet. These structural parameters are determined from TEM and WAXD.

Representative TEM images are shown in Figure 6-1a and Figure 6-1b for PMMA-LAP (3% wt./wt.) and PMMA-FH (3% wt./wt), respectively and provide a visual confirmation of L. Figure 6-1a reveals in general a well-dispersed, highly exfoliated morphology of short 30 nm laponite platelets. Several small tactoids, consisting of two or three plates are present as well. Figure 6-1b indicates the presence of >300 nm fluorohectorite platelets. Few single clay sheets are observable and, in general, the morphology is dominated by larger aggregates, typically consisting of 5 – 7 platelets.
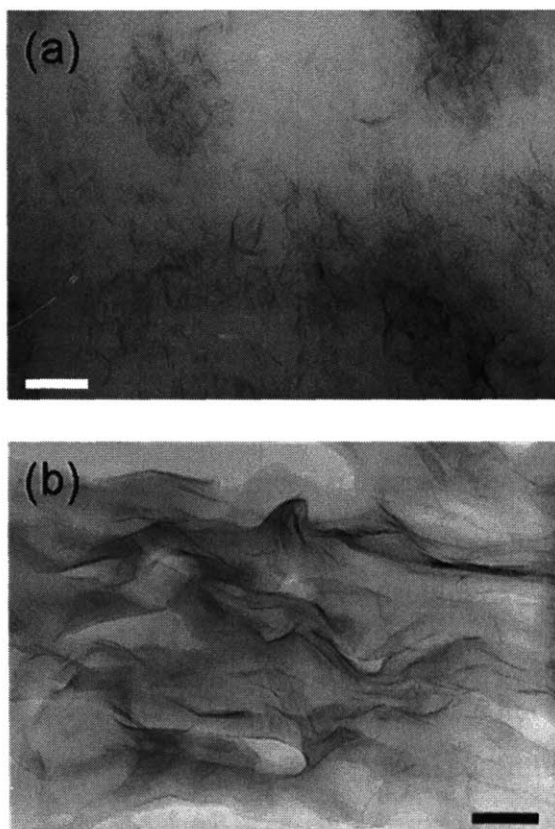
Figure 6-1. Cross-sectional TEM images of (a) PMMA-LAP and (b) PMMA-FH. Scale bars represent 100 nm.

WAXS intensities reveal information about the parameters N and $d_{(001)}$. $d_{(001)}$ is calculated from Bragg's law (Brady 2003):

$$d_{(001)} = \frac{\lambda}{2\sin\theta} \tag{6-2}$$

where λ is the wavelength of x-ray radiation and θ is the scattering angle. N can be calculated from Scherrer's equation (Alexander 1969) which gives the tactoid thickness t:

$$t = \frac{K\lambda}{\beta\cos\theta} \tag{6-3}$$

where K is a constant, usually with the value of $0.9 - 1$, and β is the breadth of the peak, measured by the full-width half-max in radians. N can then be obtained by re-arranging Equation 6-1:

$$N = \frac{(t - d_s)}{d_{001}} + 1 \tag{6-4}$$

Figure 6-2a shows representative WAXS intensities for PMMA-LAP at various loading percentages (wt./wt.). The peak centered on $2\theta = 7°$ reveals a d_{001} for the PMMA- LAP to be 1.26 nm. At low loadings, we observe only a broad increase in the intensity in this region rather than a distinct peak, which corresponds to very small tactoid size, indicating a well exfoliated morphology. Only above loadings of 4.5% wt./wt.does the hint of a peak appear. Even in the case of these higher loadings, we expect relatively few tactoids. For example, at 6.0% wt./wt., the morphology of PMMA-LAP consists of tactoids with $t = 3.6$ nm (calculated from Equation 6-3) and $N = 3$. These results, coupled with the direct visual confirmation from TEM micrographs, indicates that the PMMA-LAP is essentially exfoliated with an aspect ratio of $p_{PMMA-LAP} = 15 - 30$. Figure 6-2b shows comparable WAXD intensities for PMMA-FH, with a peak around $2\theta = 5.5°$. The resulting d_{001} for the PMMA-FH is 1.68 nm, indicating more intercalation of PMMA chains into the gallery between platelets compared to PMMA-LAP. PMMA-FH shows an exfoliated morphology at loadings of 1.5% (wt./wt.) or less. At higher loadings, as low as 3.0% (wt./wt.), tactoids with $t = 6.0$ nm and $N = 4$ are present. Using the TEM images and WAXS results, we estimate that $p_{PMMA-FH} = 50 - 100$. In both the case of PMMA-LAP and PMMA-FH, the morphologies are represented by a wide distribution of particle

aspect ratios and are functions of concentration, and we estimate that these values represent typical behavior.
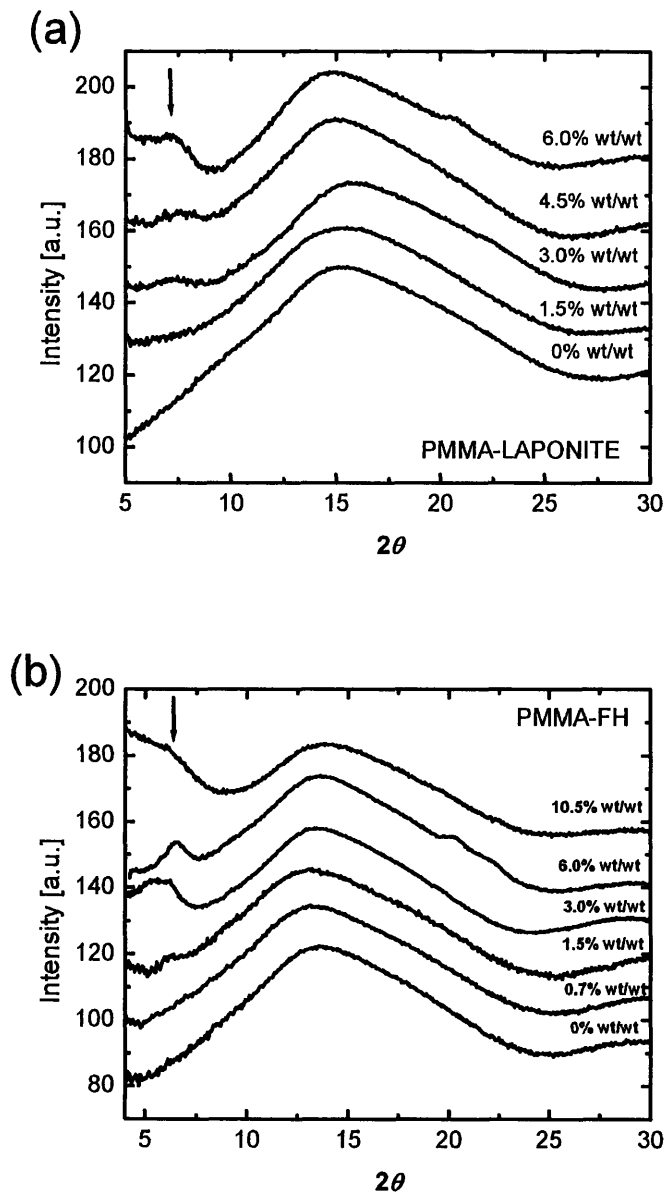
Figure 6-2. WAXS intensities for (a) PMMA-LAP and (b) PMMA-FH at various wt.% loadings. Peaks in the region of $5^{\circ} \leq 2\theta \leq 7.5^{\circ}$ correspond to d_{001} of the clays, indicated by the arrows. The broad peak in the region of $2\theta \approx 15^{\circ}$ is the signature of the amorphous PMMA.

To convert weight fractions into an appropriate volume fraction, we use an equation from the previously developed formalism by Sheng *et al.* (2004):

$$\phi_v = \left(\frac{t\rho_{PMMA}}{Nd_s\rho_{clay}} \right) f_W \qquad (6\text{-}5)$$

where f_0 is the weight percentage of clay, $\rho_{PMMA} = 1.13$ g/cm^3 (Larson 1999) and $\rho_{clay} = 2.44$ g/cm^3 (Sheng *et al.* 2004).

Frequency sweeps of the storage modulus, $G'(\omega)$, from small-angle oscillatory shear (SAOS) measurements are shown for PMMA-LAP and PMMA-FH in panels a and b from Figure 6-3, respectively. Data for PMMA-LAP was generated with time temperature superposition (TTS) because high temperatures caused degradation of the samples after electron beam irradiation (used to decrease the molecular weight of the PMMA matrix). The degradation is observable in the deviation of from the -2 scaling of $G'(\omega)$ in the terminal region and in the failure of TTS at higher temperatures (low frequencies) for the unfilled PMMA sample. Both samples show similar behavior; at low loadings (< 1% vol./vol.) of a clay filler, $G'(\omega)$ shows moderate enhancement over the entire range of frequencies,. At loadings greater than 1% vol./vol., $G'(\omega)$ increases more rapidly at low frequencies tthan at higher frequencies. Eventually this rapid enhancement in low frequency $G'(\omega)$ becomes an observable plateau, typical of the long relaxation time associated with the formation of a percolated network (Larson 1999; Jones 2002).

The formation of the percolated network can be observed in the low frequency terminal region with increased loading of clay filer. The onset of percolation typically accompanies critical-like behavior in material functions, including $G'(\omega)$, and is expressed by:

$$G'(\omega) \sim (\phi_v - \phi_p)^\mu \tag{6-6}$$

where ϕ_p is the critical volume fraction for percolation and μ is a fractal exponent that is associated with the number of bonds in bond percolation or the number of contacts in lattice percolation (Larson 1999; Jones 2002) . We examine this behavior in the inset
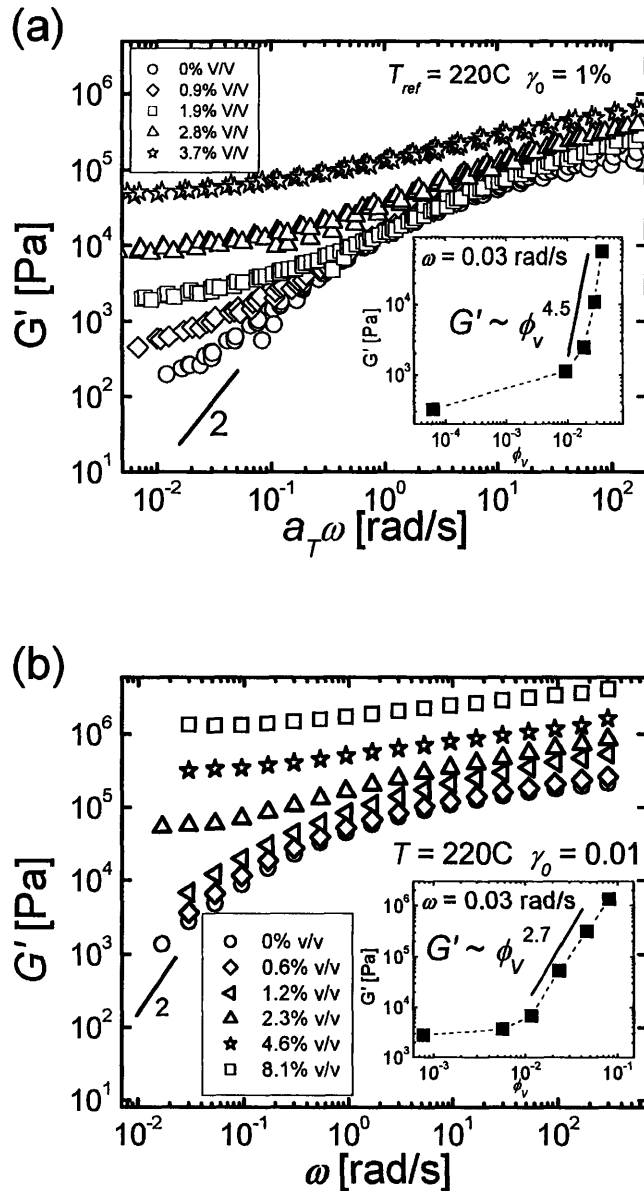
Figure 6-3. Frequency sweeps for G' for (a) PMMA-LAP, (b) PMMA-MMT and (b) PMMA-FH. Inset graphs show low frequency data at $\omega = 0.03$ rad/s (De >> 1) as a function of ϕ_v.

136

graphs of Figure 6-3. Values taken at $\omega = 0.03$ rad/s are plotted as a function of ϕ_v. This corresponds to measurements of $G'(\omega)$ at De $\ll 1$, where De is the Deborah number and defined by:

$$De = \omega\tau_p \tag{6-7}$$

where ω is the angular frequency and τ_p is the relaxation time associated with reptation in the PMMA matrix. From each of these inset curves we observe a sharp transition in the dependence of $G'(\omega)$ with ϕ_v. It has been shown that the ϕ_v corresponding to the transition can correspond to ϕ_p. $\phi_{p,LAP-PMMA}$ is greater than $\phi_{p,FH-PMMA}$, as expected from the larger aspect ratio of PMMA-FH.

The percolation thresholds for oblate spheroids (disk-like shapes) can be obtained from the simulation work of Garboczi et al. (Garboczi et al. 1995), where they used a Monte Carlo simulation to determine the purely geometric percolation threshold via conductivity measurement (e.g. hard contacts between particles). Drawing on their work and using the aspect ratios we have determined previously from WAXS and TEM, we obtain theoretical values for $\phi_{p,LAP-PMMA} \approx 0.05$ and $\phi_{p,FH-PMMA} \approx 0.02$. This is around three times higher compared to what is shown in the experimental results in Figure 6-2 but is consistent with previous observations that (Jeon et al. 2003; Jeon et al. 2004) the pure geometric percolation thresholds were calculated for overlapping particles. Additional discrepancies can be explained by the presence of a broad distribution of aspect ratios (Plantard and Papini 2002). Though there is not an exact numerical correspondence with the simulation work, we note that the ordinal values from our experiments are consistent with the predictions of Garboczi et al.

To relate p, ϕ_v, and ϕ_p to a material function such as $G'(\omega)$, Favier et al. (Favier et al. 1995) use an expression to describe the shear modulus G of a percolated structure of rods as:

$$G = \frac{(1-2\psi+\psi\phi_v)G_{PMMA}G_{clay}+(1-\phi_v)\psi G_{clay}^2}{(1-\phi_v)G_{clay}+(\phi_v-\psi)G_{PMMA}}$$ (6-8)

$$\psi = 0 \qquad \phi_v \leq \phi_p$$ (6-9)

$$\psi = \phi_v\left(\frac{\phi_v-\phi_p}{1-\phi_p}\right)^{\mu} \qquad \phi_v > \phi_p$$ (6-10)

where G_{PMMA} and G_{clay} are the shear moduli for PMMA and corresponding clay respectively.
We compare the predictions from the Favier rod-model to our experimental results in Figure 6-4,
with the model parameters shown in Table 6-2. We find that the predictions of the Favier theory
correspond well to the experimental results. We observe that the lower $\phi_{c,FH} = 8.0\times10^{-3}$ for
PMMA-FH compared to $\phi_{c,LAP} = 1.6\times10^{-2}$ for PMMA-LAP is consistent with the larger aspect
ratio of PMMA-FH. Similarly we note that the scaling constant of PMMA-FH ($\mu_{FH} = 1.2$) is
less than that of PMMA-LAP ($\mu_{LAP} = 1.4$). The larger scaling exponent may correspond to the
higher number of "contacts" in the percolated network and be indicative of the more exfoliated
morphology of PMMA-LAP in good correspondence with the analysis of the TEM micrograph of
Figure 6-1a.

Table 6-2. Model parameters for Favier theory (Favier _et al._ 1995)

Clay Type	Abbr.	ϕ_p	G_{PMMA} [Pa]	G_{PMMA} [Pa]	μ
Laponite	LAP	0.008	3500	3×10^8	1.2
Fluorohectorite	FH	0.016	1000	3×10^8	1.4

An alternate description of the effect of rod-like fillers in a surrounding matrix was
proposed by Guth (Guth 1944) in the context of carbon black filled rubber. Providing
comparable predictions from Favier's percolation theory, the Guth theory describes the effect of

rod-fillers on the modulus of composites based on the aspect ratio (p) and volume fraction (ϕ_v) as shown by:

$$G(p,\phi_v) = G_0\left[1 + 0.67\left(\frac{\phi_v}{p}\right) + 1.62\left(\frac{\phi_v}{p}\right)^2\right]$$

(6-11)

where G_0 is the modulus of the unfilled matrix. Figure 6-5 shows measurements of $G'(\omega)$ at De $\gg 1$, obtained at $\omega = 100$ rad/s for PMMA-LAP and PMMA-FH compared with predictions from the Guth-Gold equation. Using the appropriate values for p, obtained from WAXD curves and TEM micrographs, the predictions from the Guth equation match well with the experimental results at $\omega = 100$ rad/s.
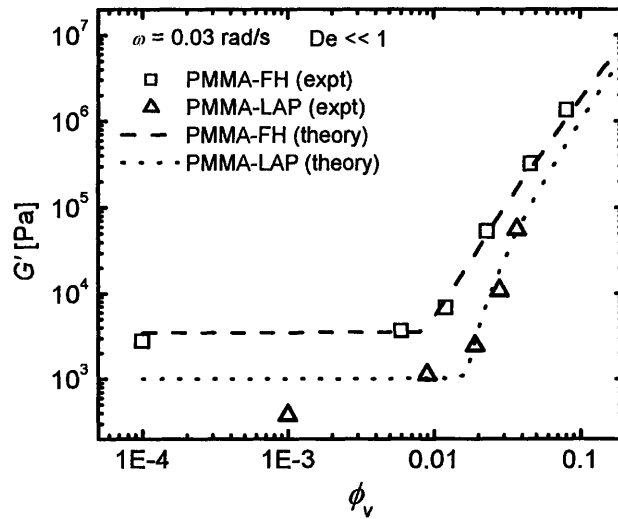
Figure 6-4. Comparison of experimental values of $G'(\omega = 0.03 \text{ rad/s})$ versus ϕ_v. Dashed and dotted lines are prediction from theory for rod fillers (Favier *et al.* 1995) from Equations 6-6, 6-7, and 6-8 for PMMA-FH and PMMA-LAP respectively.
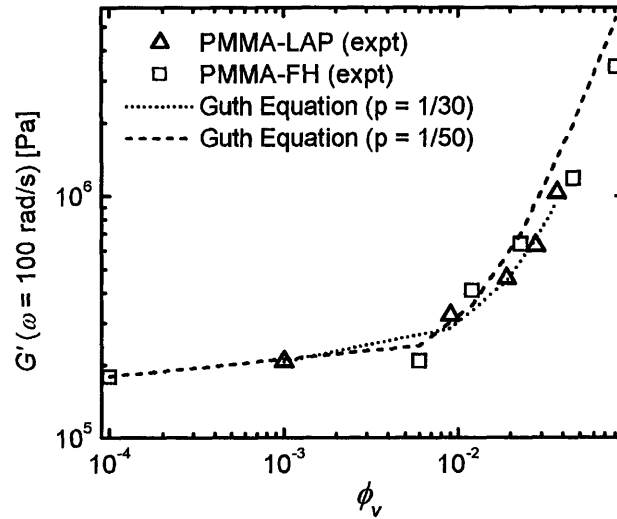
Figure 6-5. Comparison of experimental values of $G'(\omega = 100 \text{ rad/s})$ **versus** ϕ_v. **Dashed and dotted lines are predictions from the Guth Equation (see Equation 6-11) for rod-like filler (Guth 1944) for PMMA-LAP and PMMA-FH respectively. The values of** p **are obtained from TEM and WAXS measurements above.**

Whereas SAOS allows us to characterize the linear viscoelastic properties of a fluid, the typical polymeric processes expose fluids to large-strain extensional deformations which can give rise to nonlinear rheological behavior such as extensional strain hardening, due to the strong true-straining nature of the flow (Sentmanat 2004). Thus it is useful to provide a characterization of the extensional rheology of these nanocomposites. In addition, stretching flows can be extremely sensitive to the underlying molecular architecture.

The kinematics of uniaxial extension for unfilled polymeric fluids, including PMMA, result in the measurement of extensional, η_E or "Trouton" viscosities, which are related to the shear viscosity, η_s, by (Bird *et al.* 1987; Greener and Evans 1998):

$$\eta_E = 3\eta_s \tag{6-12}$$

Batchelor (Batchelor 1971; Utracki and Lara 1984; Lubansky *et al.* 2005) developed an expression which relates η_s to the volume fraction and the aspect ratio of rod-like fillers:

$$\eta_E = \eta_s \left(1 + \frac{4\phi_v (1/p)^2}{9\ln\left(\dfrac{\pi}{\phi_v}\right)} \right) \qquad (6\text{-}13)$$

which demonstrates an expected increase in the extensional viscosity with both increasing volume fractions loadings and aspect ratio.

Figure 6-6 shows the transient extensional viscosity growth functions, $\eta_E^+(t)$, for PMMA-FH at different values of Hencky strain rate ($\dot{\varepsilon}_H$) at $\phi_v = 0$ and $\phi_v = 0.023$ respectively. The linear viscoelastic envelope (LVE) for pure PMMA, calculated from a discrete relaxation spectrum obtained from the SAOS data of Figure 6-3a, is shown as a dashed line (a discussion of the relaxation spectrum is included in Chapter 5). For the sample without clay loading, as shown in Figure 6-6a, we observe very good correspondence with the LVE and good superposition of the extensional stress growth functions $\eta_E^+(t)$ with $\dot{\varepsilon}_H$ for $\dot{\varepsilon}_H \leq 1$. At $\dot{\varepsilon}_H = 3$, which corresponds to De > 1, we observe the presence of moderate extensional-hardening associated with pure PMMA. With moderate clay loadings, $\phi_v = 0.023$, as shown in Figure 6-6b, the stress growth functions exhibit a systematic increase in the extensional viscosity, across a large range of Hencky strains. However we observe no strain-hardening at De > 1. Indeed, the curves show a strain induced thinning at the higher strains at all measured values of $\dot{\varepsilon}_H$.

The origin of this apparent strain-thinning is elucidated in Figure 6-7 which shows the transient stress growth functions of PMMA-FH at two fixed values of $\dot{\varepsilon}_H$. The inset graphs show data points taken at fixed values of ε_H (fixed value of t), obtained as a function of ϕ_v and the prediction from Batchelor's equation from Equation 6-13. From Figure 6-7a, corresponding to De << 1, and at a low values of Hencky strain, $\varepsilon_H = 0.003$, we observe a strong increase in $\eta_E^+(t)$ with ϕ_v which matches well with the predictions from Batchelor's equation, as well as expectations from SAOS data. At higher strains, $\varepsilon_H = 0.3$, we note that $\eta_E^+(t)$ continues to increase with ϕ_v although the extent of increase is significantly reduced (from a factor of three to

a factor of two at $\phi_v = 0.023$). For De > 1 [Figure 6-7b] we note the increase in $\eta_E^+(t)$ at

$\varepsilon_H = 0.3$ is three at $\phi_v = 0.023$, slightly higher than the corresponding strain at De <<1.

However at $\varepsilon_H = 2$ the increase in $\eta_E^+(t)$ with filler loading is severely decreased. Indeed the transient extensional viscosity growth curves in Figure 6-7b indicate that beyond some critical Hencky strain, the extensional viscosities for PMMA loaded with different fillers appear to converge to the value of unfilled PMMA.
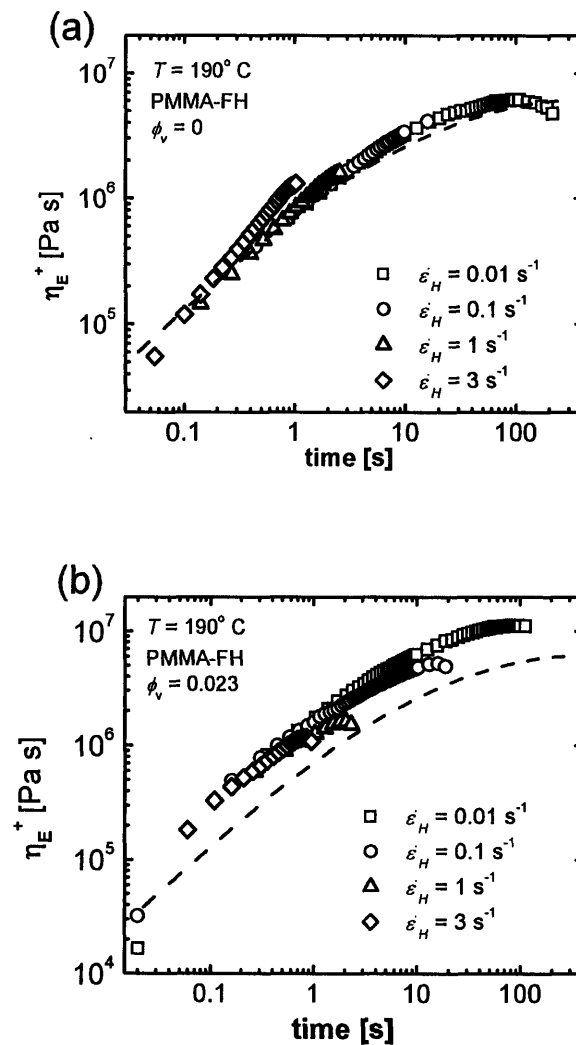
Figure 6-6. Transient extensional stress growth for PMMA-FH at (a) $\phi_v = 0$ and (b) $\phi_v = 0.023$ at various Hencky strain rates $\dot{\varepsilon}_H$. Dashed lines represent the LVE for $\phi_v = 0$, calculated form a discrete spectrum obtained from SAOS data.
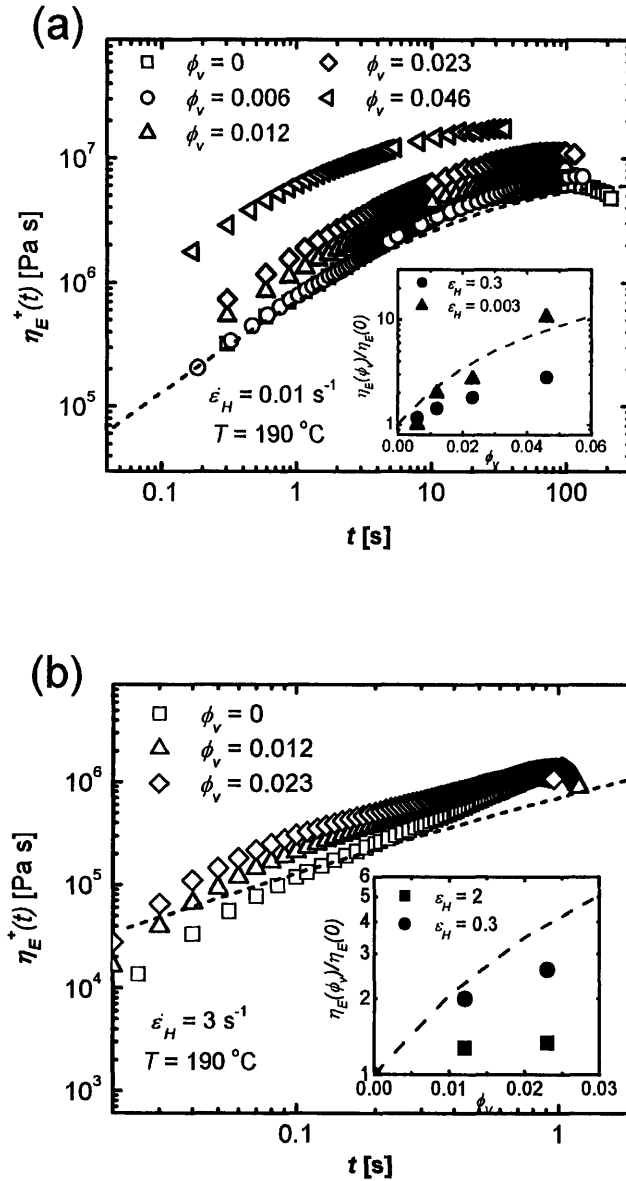
Figure 6-7. Transient extensional stress growth functions for PMMA-FH at (a)
$\dot{\varepsilon}_H = 0.01$ s^{-1} and (b) $\dot{\varepsilon}_H = 3$ s^{-1} at various volume fractions ϕ_v with dashed lines indicating
the LVE. Inset graphs are vertical slices taken at constant $\varepsilon_H = \dot{\varepsilon}_H t$ illustrating effect of
strain on reducing particle enhancement of $\eta_E^+(t)$, where the dashed line represents
predictions from Equation 6-13.

It has been shown that extensional flows can give rise to strong alignment of anisotropic
particles at Hencky strains greater than one (Okamoto *et al.* 2001; Okamoto *et al.* 2001). The

alignment of platelets results in a complex process that has a convoluted influence on the viscosity enhancement due to the filler. As particles align, there is an increased contribution to the viscous dissipation due to the rotation of the particle. However there is evidence that elongation decreases the distances between clay platelets [orthogonal to the axis of stretching] bringing neighboring platelets into contact which can aggregate into larger, lower aspect ratio fillers, resulting in diminished reinforcement by decreasing the aspect ratio of the particles . Alternatively, in the case of attractive interactions between polymer molecules with the clay platelets, elongation results in greater chain-stretching which can give rise to extensional-thickening. Because the emulsion polymerized PMMA does not contain flocculation stabilizing moieties, it is possible that alignment gives rise to aggregation of the particles. The decreasing reinforcement of the PMMA nanocomposites is consistent with this explanation. This has implications regarding the processing of clay nanocomposites, suggesting that large extensional strain, typical in film blowing or extrusion, can give decrease the extent of exfoliation.

The experimental results for transient extensional stress growth of PMMA-LAP are shown in Figure 6-8. The dashed lines are again calculated LVEs for PMMA. The PMMA-LAP system exhibits qualitatively comparable behavior as the PMMA-FH composites. Figure 6-8a shows reasonable overlap between transient stress growth functions at low Hencky strains; however the strain-thinning behavior associated with alignment of the clay particles begins at $\varepsilon_H = 0.1$. This is less than what is observed in the PMMA-FH data of Figure 6-6b and expected because of the shorter platelet length of laponite. We also observe a considerable enhancement in extensional viscosities with even relatively low loadings of Laponite. The inset graph of Figure 6-8b, illustrates the relative extensional viscosities, at low Hencky strains ($\varepsilon_H = 0.01$). Even though the predictions of Batchelor's equation, shown in Equation 6-13, qualitatively match the increase in relative viscosity, the theory appears to under predict the magnitude of the enhancement. This could originate from the highly exfoliated nature of the PMMA-LAP composites and the formation of a highly percolated network of tactoids. Despite this, Batchelor's equation provides an adequate description for the effect of aspect ratio and volume fraction of clays on the enhancement of transient extensional viscosities at low Hencky strains.
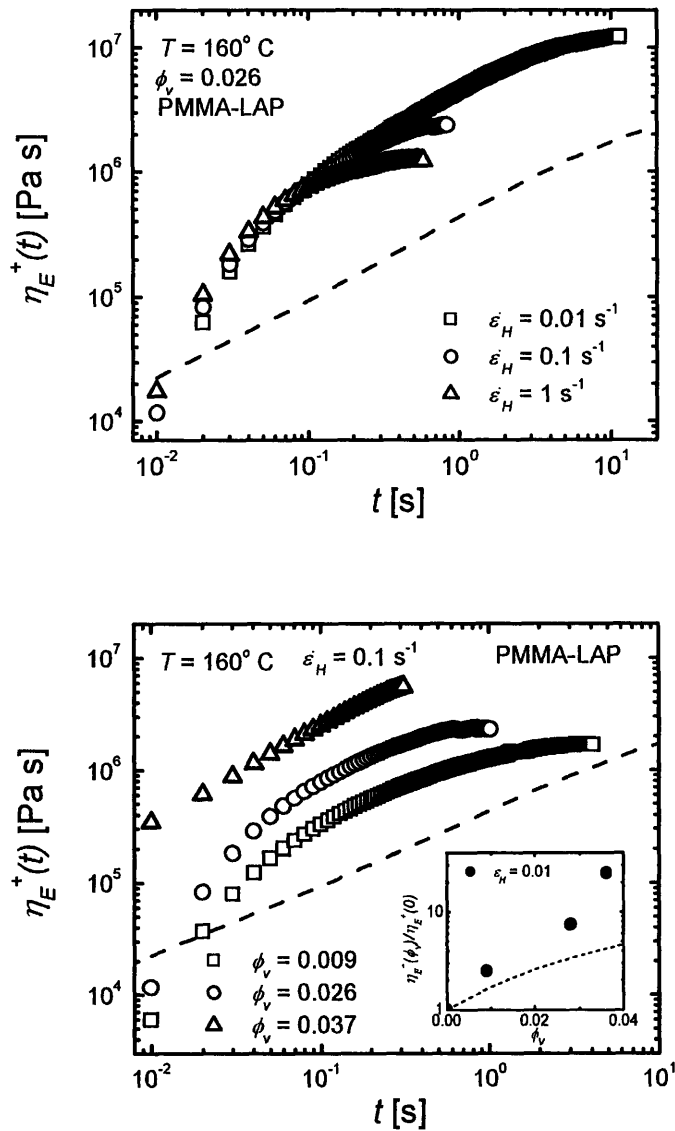
Figure 6-8. Transient extensional stress growth functions for PMMA-LAP as a function of (above) Hencky strain rate, $\dot{\varepsilon}_H$, and (below) volume fraction, ϕ_v. Dashed lines represent LVE of PMMA. Inset graph in panel below shows relative viscosity as a function of ϕ_v at low Hencky strain, with the dashed line representing the predictions of Equation 6-13.

Lastly we examine the results of relaxation of stress following cessation of extension for PMMA-LAP, shown in Figure 6-9. Following extension at $\dot{\varepsilon}_H = 0.1$ s^{-1} for one second, the strain is fixed and the evolution of stress is monitored. We observe ~ 80% of the stress relaxed

within $t < 10$ s as PMMA chains return to their equilibrium coils. At $t > 10$ s, relaxation is systematically retarded until an constant exponential decay is reached at $t > 100$ s. In the semi-log plot, relaxation time, $\tau_{relaxation}$, can be calculated from:

$$\tau_{relaxation} = -(t_2 - t_1)\ln\left(\frac{\eta_r^-(t_2)}{\eta_r^-(t_1)}\right)$$

(6-14)

where t_2 and t_1 are two times separated by a linear decrease in the graph (denoted in Figure 6-9 by the dashed lines). From Equation 6-14 we calculate the relaxation times shown in Table 6-3. Though it is clear that the trend is monotonically increasing, it is also nonlinear, where a dramatic increase in $\tau_{relaxation}$ occurs between $\phi_v = 0.028$ and $\phi_v = 0.036$. We expect an additional relaxation time once the particles are no longer being aligned by the flow-field, due to the randomization of the alignment of particles, brought about by Brownian rotation. Larson (Larson 1999) defines a dilute solution relaxation time, for oblate spheroids such as clay platelets as:

$$\tau_{rot} = \frac{1}{6D_{r0}} = \frac{2k_BT}{9\eta_s d^3}$$

(6-15)

where k_B is Boltzmann's constant and d is the length of a clay sheet. We estimate $\tau_{rot} \sim 3500$ s for Laponite, using $d = 30$ nm, $\eta_s \sim 1 \times 10^6$ Pa s, and $T = 160°C$. τ_{rot} is significantly longer than the measured relaxation times from the stress relaxation experiments. Furthermore Equation 6-15 is the dilute solution rotation time which neglects the potential interactions between particles. Thus there is an observable increase in the relaxation time at long times due to the presence of increasing amounts of clay, though it is significantly faster than the realignment of particles due to Brownian rotation.
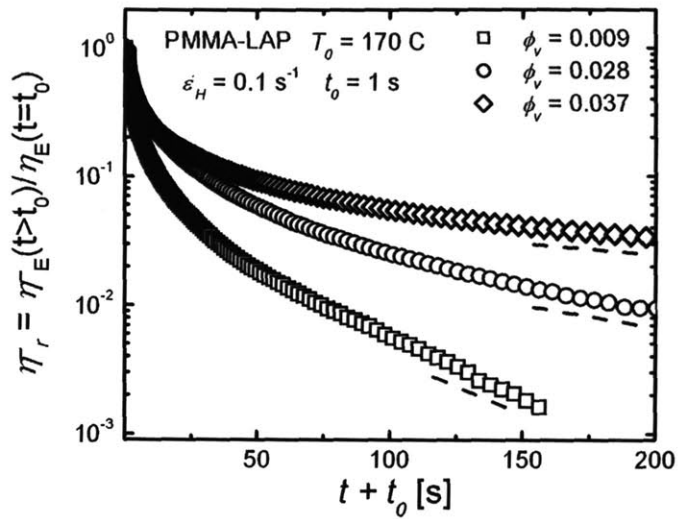
Figure 6-9. Stress relaxation functions following cessation of uniaxial extension for PMMA-LAP nanocomposites.

Table 6-3. Relaxation times ($\tau_{relaxation}$) for PMMA-LAP as a function of ϕ_v of clay.

ϕ_v	$\tau_{relaxation}$ [s]
0.009	45
0.028	95
0.037	269

6.4. Conclusions

In summary, we provided a fundamental characterization of the shear and extensional rheology of clay-filled PMMA. We characterized two PMMA-clay nanocomposites using morphological techniques such as WAXS and TEM in conjunction with a formalism for "effective particles" from Sheng *et al.* to determine the aspect ratio and corresponding volume fractions of the clay fillers. We examined the linear viscoelastic properties, using small-amplitude oscillatory shear experiments, and demonstrated that the values of the storage modulus matched well with theoretical models based on volume fraction and aspect ratio, using both

Guth-Gold's equation for rod-like fillers and the percolation model of Favier *et al.* We examined the extensional rheology of the clay-filled nanocomposites and observed enhancement with increasing volume fraction of the clay. Results from PMMA-FH corresponded well with Batchelor's theory for elongated rods, but PMMA-LAP showed a small additional enhancement, likely due to the substantially exfoliated morphology and resulting physical contacts between plates. The effect of the enhancement diminished at Hencky strains of $\varepsilon_H \sim 0.1$ for PMMA-LAP and $\varepsilon_H \sim 0.3$ for PMMA-FH which suggested that the decrease in extensional viscosity corresponded with alignment of the platelets. Relaxation of stress experiments illustrate a long time-scale process that monotonically increases with volume fraction, but is significantly faster than relaxation of the polymer chains and significantly shorter than the rotational diffusion of the particles. Overall we demonstrate that comparisons between experimental rheological measurements and theories for high aspect ratio rod-like fillers may help elucidate the morphology of PMMA-clay nanocomposites synthesized by emulsion polymerization.

6.5. Acknowledgements

7. SUMMARY OF THESIS CONTRIBUTIONS

The primary goal of this thesis was to develop the combination of rheological and morphological techniques which would contribute to building structure-property relationships in hierarchically nano-structured materials, assembled from "0-D", "1-D", and "2-D" nanoparticles. Rheology was a specific focus because of the emphasis on polymeric materials in this thesis and its relevancy to processing.

Chapter two provided an introduction to extensional rheology methods using a novel extensional rheology fixture. We presented a validation of the new device, the SERUTP, using three different polyethylenes (PEs), which compared results to existing data and provided a diverse menu of experimental modes that would be heavily utilized in the experiments of chapters five and six. Experimental results from the SERUTP showed excellent agreement with literature data of the same materials. In addition an experimental verification of theoretical considerations of the Considere criterion for stability in extensional flow is provided.

Chapter three provided a framework for the use of small-angle x-ray scattering (SAXS) to determine the orientation and diameters of "1-D" multiwall carbon nanotube (MWCNT) films. Through a comparison with standard morphological characterization by scanning electron microscopy (SEM) and high-resolution transmission electron microscopy (HRTEM), we observed quantitative results from SAXS for two different films which showed good agreement with SEM and HRTEM. In addition, SAXS data was shown to have the additional benefit of maintaining spatial correspondence with location within the film, demonstrating that variation in orientation and CNT diameter occurred through the thickness of the film. This direct measurement provided new insight into the evolution of the catalyst substrate during growth.

Chapter four described extensions to the techniques developed in chapter three. We used SAXS to elucidate additional spatial variation in pristine films and monitored changes in morphology of films subjected to mechanical manipulations. Uniaxially compressed MWCNT films were shown to respond through a buckling deformation, observable in both SAXS and SEM. Changes in the SAXS signature of MWCNT films, converted to cellular foams by

capillarity induced densification, corresponded to a change in the inter-CNT spacing between neighboring CNTs. Using the formalism of a structure factor, we illustrated how these SAXS signatures can provide an estimate of the packing between neighboring CNTs We used *in situ* SAXS measurements during capillarity induced densification of films in real-time, and illustrated the sharp change in alignment and packing density with time. Overall, Chapters three and four developed the notion of a flexible SAXS technique which is capable of elucidating additional morphological information about CNT films as a counterpart to electron microscsopy.

Chapter five provided a characterization of the extensional rheological properties of "0-D" nanocomposites formed from blending methacryl functionalized polyhedral oligomeric silsesquioxane [mPOSS], a silica-oxide cage with organic functional groups tethered to the corners, and two different poly(methyl methacrylate) [PMMA] matrices. The blends showed the presence of a secondary mPOSS-rich phase above critical volume fractions. Under uniaxial extensional deformations, transient stress growth functions showed good correspondence with linear viscoelastic data, but exhibited remarkable enhancement in the extensional viscosity when the miscibility limit of mPOSS in PMMA was exceeded. Relaxation of the polymeric matrix was accelerated, observed in the relaxation of stress following cessation of extension. This chapter provided the first characterization of POSS nanocomposites in extension and provided greater guidance forprocessing.

Chapter six contained a fundamental investigation of the effect of volume fraction and aspect ratio of clay on the rheology of "2-D" clay-PMMA nanocomposites synthesized by emulsion polymerization. The experimental measurements of the storage modulus from shear rheology of the two clay systems showed excellent correspondence with the predictions of the Guth-Gold equation for rod-fillers and percolation theory based on rods. Transient extensional stress growth experiments indicated that enhancement of extensional viscosity with increased loading of clay matched well with the predictions of Batchelor's theory for elongated rods. Measurements at high Hencky strains showed that alignment of clay platelets resulted in a steady loss of the enhancement due to clay. The onset of this loss occurred at lower strains for the shorter, lower aspect ratio, PMMA-LAP nanocomposite. Stress relaxation following cessation of extension of PMMA-LAP was increasingly retarded with increasing amounts of clay, but

significantly less than expected for a relaxation process based on the randomization of the platelet alignment by rotational diffusion. In summary we demonstrated an experimental validation that the rheology of clay-filled polymer systems can correspond to various theoretical developments for high-aspect ratio rod-like fillers.

Overall this thesis provided a comprehensive menu of characterization techniques and illustrations useful for studying hierarchically nanostructured materials based on "0-D", "1-D", and "2-D" nanoparticles. The effects of morphological characteristics, including size, aspect ratio, alignment, volume fraction, shape, and spatial density have been considered.

8. FUTURE WORK

The breadth of this thesis invites several diverse pathways for future work along the lines of characterization with a long-term goal of building structure-property relationships. A straight forward extension of the "0-D" and "2-D" filler case could include the incorporation of the mPOSS and clay particles into a larger macroscopic hierarchical structure. This can be done through forced assembly via multilayer coextrusion , when incorporated particles can be confined to alternating layers. With the use of a polymer pair, such as polycarbonate and PMMA, mPOSS can be loaded into the PMMA layer as a multifunctional additive to modify viscosity, impart thermal and radiative stability (Sulaiman *et al.* 2006), and perhaps enhance the cooperative yielding of PC/PMMA multilayers (Kerns *et al.* 1999; Kerns *et al.* 2000). Two extrusion streams of PMMA, with one stream containing the mPOSS, can be multilayered together to localize regions of mPOSS-PMMA, creating lamellae of PMMA alternating with mPOSS-PMMA where the normalized concentration of mPOSS changes from one to zero and back again through the thickness of the film. The resulting material would likely have strange rheological properties, both in extension and shear (Saito and Macosko 2002; Zhao and Macosko 2002; Cole *et al.* 2003; Adhikari and Goveas 2004), and would benefit from morphological characterization to determine the true underlying influence of the structure.

Further extensional rheological characterization of mPOSS and clay composites should be pursued. Extensional rheology should provide exteremely sensitive measurements of POSS-PMMA copolymer, blended with POSS, to go with the proposed "sticky-reptation" model proposed by Kopesky et al (2004). There should be some focus on increasing the aspect ratio of clay fillers by creating an even more exfoliated morphology to provide additional experimental comparisons to the mentioned theories. To validate the origin of the loss of enhancement in highly aligned clay-PMMA composites, the incorporation of anti-flocculating components should be included. Extensional rheology should be performed on composites with enhanced Interactions between the matrix and clay to determine if further enhancement can be achieved.

For the case of the "1-D" nanoparticle, the use of SAXS to characterize the areal density, CNT diameter, orientation and shape of MWCNT films, using synchrotron radiation, should

invite a wide range of characterizations. The initial extension would be the application of the technique to other macroscopic films of cylindrical nano-structures, such as singlewall carbon nanotubes (Futaba *et al.* 2006; Futaba *et al.* 2006) or zinc oxide nanowires (Banerjee *et al.* 2005; Fan *et al.* 2005). The simultaneous measurement of quantitative mechanical properties (e.g. compressive modulus, yield stresses, shear modulus) with *in situ* SAXS characterization could provide additional information about the locally-averaged bulk properties of CNT films compared to existing measurement using nanoindentation (Qi *et al.* 2003).

The recent interest in forming CNT-polymer nanocomposites from pristine and patterned films of preferentially oriented MWCNTs could benefit from rheological characterization both in shear and in extension (Garcia *et al.* 2007). For the case of non-crosslinked polymers, the rheology of the resulting fluids would likely exhibit strong nonlinear responses to strain. The local confinement of polymeric chains by surrounding MWCNTs could change the morphological properties of the film, by influencing the alignment or crystallinity of chains near the CNT walls , inviting a foray into wide angle X-ray scattering (WAXS) characterizations of the composites. Furthermore rheological characterization could provide further information about the time-resolved dynamics of capillarity induced densified films.

9. REFERENCES

Adhikari, N. P. and J. L. Goveas (2004). "Effects of slip on the viscosity of polymer melts." Journal of Polymer Science: Part B: Polymer Physics **42**: 1888-1904.

Alexander, L. E. (1969). X-ray diffraction methods in polymer science. New York, John Wiley & Sons, Inc.

Alfrey Jr., T. and W. J. Schrenk (1980). "Multipolymer systems." Science **208**: 813-818.

Anna, S. L., G. H. McKinley, D. A. Nguyen, T. Sridhar, S. J. Muller, J. Y. Huang and D. F. James (2001). "An inter-laboratory comparison of measurements from filament-stretching rheometers using common test fluids." Journal of Rheology **45**: 83 - 114.

Arigo, M. T. and G. H. McKinley (1997). "The effects of viscoelasticity on the transient motion of a sphere in a shear-thinning fluid." Journal of Rheology **41**: 103 - 128.

Artyukhin, A. B., M. Stadermann, R. W. Friddle, P. Stroeve, O. Bakajin and A. Noy (2006). "Controlled electrostatic gating of carbon nanotube FET devices." Nano Letters **6**(9): 2080 - 2085.

Bach, A., K. Almdal, H. K. Rasmussen and O. Hassager (2003). "Elongational viscosity of narrow molar mass distribution polystyrene." Macromolecules **36**: 5174 - 5179.

Bach, A., H. K. Rasmussen and O. Hassager (2003). "Extensional viscosity for polymer melts measured in the filament stretching rheometer." Journal of Rheology **47**: 429 - 441.

Banerjee, D., J. Rybzynski, J. Y. Huang, D. Z. Wang, K. Kempa and Z. F. Ren (2005). "Large hexagonal arrays of aligned ZnO nanorods." Applied Physics A: Material Science and Processing **80**: 749 - 752.

Barroso, V. C. and J. M. Maia (2002). "Evaluation by means of stress relaxation (after a step strain) experiments of the viscoelastic behavior of polymer melts in uniaxial extension." Rheologica Acta **41**: 257 - 264.

Batchelor, G. K. (1971). "The stress generated in a non-dilute suspension of elongated particles by pure straining motion." Journal of Fluid Mechanics **48**: 813-829.

Bates, F. S., R. E. Cohen and C. V. Berney (1982). "Small-Angle Neutron Scattering Determination of Macrolattice Structure in a Polystyrene-Polybutadiene Diblock Copolymer." Macromolecules **15**: 589-592.

Baughman, R. H., A. A. Zakhidov and W. A. de Heer (2002). "Carbon nanotubes - the route toward applications." Science **297**: 787 - 792.

Bendiab, N., R. Almairac, J. L. Sauvajol, S. Rols and E. Elkaim (2003). "Orientation of single-walled carbon nanotubes by uniaxial pressure." Journal of Applied Physics 93(3): 1769 - 1773.

Bennett, R. D., A. J. Hart and R. E. Cohen (2006). "Controlling the morphology of carbon nanotube films by varying the areal density of catalyst nanoclusters using block copolymer micellar thin films." Advanced Materials 18(17): 2274.

Bennett, R. D., A. J. Hart, A. C. Miller, P. T. Hammond, D. J. Irvine and R. E. Cohen (2006). "Creating Patterned Carbon Nanotube Catalysts through the Microcontact Printing of Block Copolymer Micellar Thin Films." Langmuir 22(20): 8273 - 8276.

Bennett, R. D., A. C. Miller, N. T. Kohen, P. T. Hammond, D. J. Irvine and R. E. Cohen (2005). "Strategies for controlling the planar arrangement of block copolymer micelles and inorganic nanoclusters." Macromolecules 38: 10728 - 10735.

Bennett, R. D., G. Y. Xiong, Z. F. Ren and R. E. Cohen (2004). "Using block copolymer micellar thin films as templates for the production of catalysts for carbon nanotube growth." Chemistry of Materials 16: 5589 - 5595.

Berney, C. V., R. E. Cohen and F. S. Bates (1982). "Sphere sizes in diblock copolymers: discrepancy between electron microscopy and small-angle scattering results." Polymer 23: 1222 - 1226.

Bird, R. B., R. C. Armstrong and O. Hassager (1987). Dynamics of Polymeric Liquids. Volume 1: Fluid Mechanics, Wiley Interscience.

Bizet, S., J. Galy and J.-F. Gerard (2006). "Molecular dynamics simulation of organic-inorganic copolymers based on methacryl-POSS and methyl methacrylate." Polymer 47: 8219-8227.

Brady, R. F., Ed. (2003). Comprehensive Desk Reference of Polymer Characterization and Analysis. Oxford, Oxford University Press.

Brown, J. M., D. P. Anderson, R. S. Justice, K. Lafdi, M. Belfor, K. L. Strong and D. W. Schaefer (2005). "Hierarchical morphology of carbon single-walled nanotubes during sonication in an aliphatic diamine." Polymer 46: 10854 - 10865.

Burian, A., J. C. Dore, A. C. Hannon and V. Honkimaki (2005). "Complementary studies of structural characteristics for carbon materials with x-rays and neutrson." Journal of Alloys and Compounds 401: 18-23.

Cao, A., P. L. Dickrell, W. G. Sawyer, M. N. Ghasemi-Nejhad and P. M. Ajayan (2005). "Super-compressible foamlike carbon nanotube films." Science 310: 1307 - 1310.

Chakrapani, N., B. Wei, A. Carrillo, P. M. Ajayan and R. S. Kane (2004). "Capillarity-driven assembly of two-dimensional celluar carbon nanotube foams." Proceedings of the National Academy of Sciences 101(12): 4009 - 4012.

Chen, W.-C., Y. Chang and J.-P. Hsu (1999). "Theoretical analysis on a multilayer coextrusion process for preparing gradient-index polymer optical fibers." Journal of Physical Chemistry B 103(7584 - 7590).

Chen, X., C. Burger, D. Fang, I. Sics, X. Wang, W. He, R. H. Somani, K. Yoon, B. S. Hsiao and B. Chu (2006). "In-situ x-ray deformation study of fluourinated multiwalled carbon nanotube and fluorinated ethylene-propylene nanocomposite fibers." Macromolecules 39: 5427 - 5437.

Ciolacu, F. C. L., N. R. Choudury, N. Dutta and E. Kosior (2007). "Molecular level stabilitzation of poly(ethylene terphthalate) with nanostructured open cage trisilanolisobutyl-poss." Macromolecules 40: 265-272.

Cole, P. J., R. F. Cook and C. W. Macosko (2003). "Adhesion between immiscible polymers correlated with interfacial entanglemetns." Macromolecules 36: 2808-2815.

Connelly, R. W., L. J. Garfield and G. H. Pearson (1979). "Local stretch history of fixed-end-constant-length-polymer-melt stretching experiment." Journal of Rheology 23: 651 - 662.

Deck, C. P. and K. S. Vecchio (2005). "Growth of well-aligned carbon nanotube structures in successive layers." Journal of Physical Chemistry B 109: 12353 - 12357.

Delaby, I., B. Ernst and R. Muller (1995). "Drop deformation during elongational flow in blends of viscoelastic fluids. Small deformation theory and comparison with experimental results." Rheologica Acta 34(6): 525 - 533.

Doi, M. and S. F. Edwards (1978). "Dynamics of concentrated polymer systems. IV. Rheological properties." Journal of the Chemical Society, Faraday Transactions 2 75: 38 - 54.

Dooley, J., K. S. Hyun and K. Hughes (1998). "An experimental study on the effect of polymer viscoelasticity on layer rearrangement in coextruded structures." Polymer Engineering and Science 38(7): 1060-1071.

Eres, G., A. A. Kinkhabwala, H. Cui, D. B. Geohegan, A. A. Puretzky and D. H. Lowndes (2005). "Molecular beam-controlled nucleation and growth of vertically aligned single-wall carbon nanotube arrays." Journal of Physical Chemistry B 109: 16684 - 16694.

Fan, H. J., W. Lee, R. Scholz, A. Dadgar, A. Krost, K. Nielsch and M. Zacharias (2005). "Arrays of vertically aligned and hexagonally arranged ZnO nanowires: a new template-directed approach." Nanotechnology 16: 913-917.

Fan, J.-G., D. Dyer, G. Zhang and Y.-P. Zhao (2004). "Nanocarpet effect: Pattern formation during the wetting of vertically aligned nanorod arrays." Nano Letters 4(11): 2133 - 2138.

Favier, V., H. Chanzy and J. Y. Cavaille (1995). "Polymer Nanocomposites Reinforced by Cellulose Whiskers." Macromolecules 28: 6365 - 6367.

Finnigan, B., K. Jack, K. Campbell, P. Halley, R. Truss, P. Casey, D. Cookson, S. King and D. Martin (2005). "Segmented polyurethane nanocomposites: impact of controlled particle size nanofillers on the morphological response to uniaxial deformation." Macromolecules 38: 7386-7396.

Flory, P. J. (1953). Principles of Polymer Chemistry. Ithaca, Cornell University Press.

Freiberger, N. and O. Glatter (2006). "Small-angle scattering from hexagonal liquid crystals." Journal of Physical Chemistry B 110: 14719 - 14727.

Furakawa, H. (1989). "Sliding along the interface of strongly segregated polymer melts." Physical Review A 40(11): 6403 - 6406.

Futaba, D. N., K. Hata, T. Namai, T. Yamada, K. Mizuno, Y. Hayamizu, M. Yumura and S. Iijima (2006). "84% Catalyst activity of water-assisted growth of single walled carbon nanotube forest characterization by a statistical and macroscopic approach." Journal of Physical Chemistry B 110: 8035 - 8038.

Futaba, D. N., K. Hata, T. Yamada, T. Hiraoka, Y. Hayamizu, Y. Kakudate, O. Tanaike, H. Hatori, M. Yumura and S. Iijima (2006). "Shape-engineerable and highly densely packed single-walled carbon nanotubes and their application as super-capacitor electrodes." Nature Materials 5: 987 - 994.

Gabriel, C., J. Kaschta and H. Munstedt (1998). "Influence of molecular structure on rheological properties of polyethylenes. I. Creep recovery measurements in shear." Rheologica Acta 37: 7-20.

Garboczi, E., K. Snyder, J. Douglas and M. Thorpe (1995). "Geometrical percolation threshold of overlapping ellipsoids." Physical Review E 52: 819 - 828.

Garcia, E. J., A. J. Hart, B. L. Wardle and A. H. Slocum (2007). "Wetting and fabrication of aligned CNT-polymer composites by a capillarity-driven method." Nanotechnology 2007: accepted.

Goveas, J. and G. H. Fredrickson (1998). "Apparent slip at a polymer-polymer interface." The European Physical Journal B 2: 79 - 92.

Graebling, D., R. Muller and J. F. Palieme (1993). "Linear viscoelastic behavior of some incompatible polymer blends in the melt. Interpretation of data with a model of emulsion of viscoelastic liquids." Macromolecules 26: 320 - 329.

Gramespacher, H. and J. Meissner (1992). "Interfacial tension between polymer melts measured by shear oscillations of their blends." Journal of Rheology 36(6): 1127-1141.

Gramespacher, H. and J. Meissner (1995). "Reversal of recovery direction during creep recovery of polymer blends." Journal of Rheology 39(1): 151- 161.

Gramespacher, H. and J. Meissner (1997). "Melt elongation and recovery of polymer blends, morphology, and influence of interfacial tension." Journal of Rheology 41(1): 27 - 44.

Graveland-Bikker, J. F., G. Fritz, O. Glatter and C. G. de Kruif (2006). "Growth and structure of a-lactalbumin nanotubes." Journal of Applied Crystallography 39: 180 - 184.

Greener, J. and J. R. G. Evans (1998). "Uniaxial elongational flow of particle-filled polymer melts." Journal of Rheology 42(3): 697 - 709.

Guinier, A. and G. Fournet (1955). Small-angle scattering of x-rays. New York, John Wiley & Sons.

Guth, E. (1944). "Theory of Filler Reinforcement." Journal of Applied Physics 15: 20 - 25.

Hachmann, P. and J. Meissner (2003). "Rheometer for equibiaxial and planar elongations of polymer melts." Journal of Rheology 47: 989-1010.

Han, C. D., Y. J. Kim and H. B. Chin (1982). "Rheological investigation of interfacial instability in two-layer flat-film coextrusion." Polymer Engineering Reviews 4(3): 178-200.

Handge, U. A. and P. Potschke (2004). "Interplay of rheology and morphology in melt elongation and subsequent recovery of polystyrene/poly(methyl methacrylate) blends." Journal of Rheology 48(5): 1103 - 1122.

Hart, A. J. and A. H. Slocum (2006). "Force output, control of film structure, and microscale shape transfer by carbon nanotube growth under mechanical pressure." Nano Letters 6(6): 1254-1260.

Hart, A. J. and A. H. Slocum (2006). "Rapid growth and flow-mediated nucleation of millimeter-scale aligned carbon nanotube structures from a thin-film catalyst." Journal of Physical Chemistry B 110: 8250-8257.

Hart, A. J., A. H. Slocum and L. Royer (2006). "Growth of conformal single-walled carbon nanotube films from Mo/Fe/Al2O3 deposited by electron beam evaporation." Carbon 44(348 - 359).

Hassager, O., M. I. Kolte and M. Renardy (1998). "Failure and nonfailure of fluid filaments in extension." Journal of Non-Newtonian Fluid Mechanics 76(137 - 152).

Hata, K., D. N. Futaba, K. Mizuno, T. Namai, M. Yumura and S. Iijima (2004). "Water-assisted highly efficient synthesis of impurity-free single-walled carbon nanotubes." Science 306: 1362 - 1364.

Helfand, E. and A. M. Sapse (1975). "Theory of unsymmetric polymer-polymer interfaces." Journal of Chemical Physics 62(4): 1327 - 1331.

Helfand, E. and Y. Tagami (1972). "Theory of the interface between immiscible polymers, II." Journal of Chemical Physics 56(7): 3592 - 3601.

Hernandez, J. J., M. C. Garcia-Gutierrez, A. Nogales, D. R. Rueda and T. A. Ezquerra (2006). "Small-angle X-ray scattering of single-wall carbon nanotubes dispersed in molten poly(ethylene terphthalate)." Composites Science and Technology 66: 2629-2632.

Hinch, E. J., O. J. Harris and J. M. Rallison (1992). "The instability mechanism for two elastic liquids being co-extruded." Journal of Non-Newtonian Fluid Mechanics 43: 311-324.

Hoffman, B., J. Kressler, G. Stoppelmann, C. Friedrich and G.-M. Kim (2000). "Rheology of nanocomposites based on layered silicates and polyamide-12." Colloid and Polymer Science 278: 629-636.

Hough, L. A., M. F. Islam, B. Hammouda, A. G. Yodh and P. A. Heiney (2006). "Structure of semidilute single-wall carbon nanotube suspenstions and gels." Nano Letters 6(2): 313-317.

Huang, X. and W. J. Brittain (2001). "Synthesis and characterization of PMMA nanocomposites by suspension and emulsion polymerization." Macromolecules 34: 3255-3260.

Hutchinson, J. W. and H. Obrecht (1977). Tensile instabilities in strain-rate dependent materials. Fracture 1977 (ICF4), Waterloo.

Ikkala, O. and G. ten Brinke (2002). "Functional materials based on self-assembly of polymeric supramolecules." Science 295: 2407-2409.

Inada, T., H. Masunaga, S. Kawasaki, M. Yamada, K. Kobori and K. Sakurai (2005). "Small-angle x-ray scattering from multi-walled carbon nanotubes (CNTs) dispersed in polymeric matrix." Chemistry Letteres 34(4): 524 - 525.

James, D. F. and K. Walters (1993). A critical appraisal of available methods for the measurement of extensional
properties of mobile systems. Techniques in Rheological Measurement. A. A. Collyer. London, Elsevier: 33-53.

Jarus, D., A. Hiltner and E. Baer (2002). "Barrier properties of polypropylene/polyamide blends produced by microlayer coextrusion." Polymer 43: 2401-2408.

Jash, P. and C. A. Wilkie (2005). "Effects of surfactants on the thermal and fire properties of poly(methyl methacrylate)/clay nanocomposites." Polymer Degradation and Stability 88: 401 - 406.

Jeon, H. S., J. K. Rameshwaram and G. Kim (2004). "Structure-property relationships in exfoliated polyisoprene/clay nanocomposites." Journal of Polymer Science: Part B: Polymer Physics 42: 1000 - 1009.

Jeon, H. S., J. K. Rameshwaram, G. Kim and D. H. Weinkauf (2003). "Characterization of polyisoprene-clay nanocomposites prepared by solution blending." Polymer 44: 5749 - 5758.

Jones, R. A. L. (2002). Soft Condensed Matter, Oxford University Press.

Joshi, M., B. S. Butola, G. Simon and N. Kukaleva (2005). "Rheological and Viscoelastic Behavior of HDPE/Octamethyl-POSS Nanocomposites." Macromolecules 39: 1839-1849.

Joshi, Y. M. and M. M. Denn (2004). Failure and recovery of entangled polymer melts in elongational flow. Rheology Reviews 2004. D. M. Binding and K. Walters. Aberystwyth.

Kaur, S., P. M. Ajayan and R. S. Kane (2006). "Design and characterization of three-dimensional carbon nanotube foams." Journal of Physical Chemistry B 110: 21377 - 21380.

Kerns, J., A. Hsieh, A. Hiltner and E. Baer (1999). "Mechanical behavior of polymer microlayers." Macromolecular Symposia 147: 15-25.

Kerns, J., A. Hsieh, A. Hiltner and E. Baer (2000). "Comparison of irreversible deformation and yielding in microlayers of polycarbonate with poly(methylmethacrylate) and poly(styrene-co-acrylonitrile)." Journal of Applied Polymer Science 77: 1545-1557.

Kim, B.-S. and P. T. Mather (2006). "Morphology, microstructure, and rheology of amphiphilic telechelics incorporating polyhedral oligosilsesquioxane." Macromolecules 39: 9253 - 9260.

Kim, H., R. E. Cohen, P. T. Hammond and D. J. Irvine (2006). "LIve lymphocyte arrays for biosensing." Advanced Functional Materials 16(10): 1313-1323.

Kim, K.-M., K. Adachi and Y. Chujo (2002). "Polymer hybrids of functionalized silsesquioxanes and organic polymers utilizing the sol-gel reaction of tetramethoxysilane." Polymer 43: 1171-1175.

Kim, T.-H., S.-M. Choi and S. R. Kline (2006). "Polymerized rodlike nanoparticles with controlled surface charge density." Langmuir 22: 2844 - 2850.

Koo, C. M., J. H. Kim, K. H. Wang and I. J. Chung (2005). "Melt-extensional properties and orientation behaviors of polypropylene-layered silicate nanocomposites." Journal of Polymer Science: Part B: Polymer Physics 43: 158 -167.

Kopesky, E. T., S. G. Boyes, N. Treat, R. E. Cohen and G. H. McKinley (2006). "Thermorheological properties near the glass transition of oligomeric poly(methyl methacrylate) blended with acrylic polyhedral oligomeric silsesquioxane nanocages." Rheologica Acta 45: 971 - 981.

Kopesky, E. T., R. E. Cohen and G. H. McKinley (2006). "Toughened poly(methyl methacrylate) nanocomposites by incorporating polyhedral oligomeric silsesquioxanes." Polymer 47: 299 - 309.

Kopesky, E. T., T. S. Haddad, R. E. Cohen and G. H. McKinley (2004). "Thermomechanical Properties of Poly(methyl methacrylate)s Containing Tethered and Untethered Polyhedral Oligomeric Silsesquioxanes." Macromolecules 37: 8992 - 9004.

Kopesky, E. T., T. S. Haddad, G. H. McKinley and R. E. Cohen (2005). "Miscibility and viscoelastic properties of acrylic polyhedral oligomeric silsequioxane-poly(methyl methacrylate) blends." Polymer 46: 4743-4752.

Kraft, M., J. Meissner and J. Kaschta (1999). "Linear viscoelastic characterization of polymer melts with long relaxation times." Macromolecules 32: 751 - 757.

Kudoh, H., T. Sasuga and T. Seguchi (1996). "High energy ion irradiation effects on mechanical properties of polymeric materials." Radiation Physics and Chemistry 48(5): 545-548.

Kwon, O. and D. A. Zumbrunnen (2001). "Progressive morphology development to produce multilayer films and interpenetratign blends by chaotic mixing." Journal of Applied Polymer Science 82: 1569-1579.

Kymakis, E. and G. A. J. Amaratunga (2002). "Single-wall carbon nanotube/conjugated polymer photovoltaic devices." Applied Physics Letters 80(1): 112-114.

Larson, R. G. (1992). "Instabilities in viscoelastic flows." Rheologica Acta 31: 213-263.

Larson, R. G. (1999). The Structure and Rheology of Complex Fluids. New York, Oxford University Press.

Lau, K. K. S., J. Bico, K. B. K. Teo, M. Chhowalla, G. A. J. Amaratunga, W. I. Milne, G. H. McKinley and K. K. Gleason (2003). "Superhydrophobic Carbon Nanotube Forests." Nano Letters 3(12): 1701 - 1705.

Laun, H. M. (2003).

Laun, H. M. and H. Munstedt (1979). "Comparison of the elongational behavior of a polyethylene melt at constant
stress and constant strain rate." Rheologica Acta **15**: 517 - 524.

Laun, H. M. and H. Schuch (1989). "Transient elongational viscosities and drawability of polymer melts." Journal of Rheology **33**: 119 - 175.

Lee, C. J., S. C. Lyu, H.-W. Kim, C.-Y. Park and C.-W. Yang (2002). "Large-scale production of aligned carbon nanotubes by the vapor phase growth method." Chemical Physics Letters **359**: 109-114.

Lee, D., M. F. Rubner and R. E. Cohen (2005). "Formation of nanoparticle loaded microcapsules based on hydrogen-bonded multilayers." Chemistry of Materials **17**(5): 1099-1105.

Levitt, L. and C. W. Macosko (1997). "Extensional rheometry of polymer multilayers: a sensitive probe of interfaces." Journal of Rheology **41**(3): 671- 685.

Lindner, P. and T. Zemb (2002). Neutrons, x-rays and light: scattering methods applied to soft condensed matter. Amsterdam, Elsevier.

Liu, H. and S. Zheng (2005). "Polyurethane networks reinforced by polyhedral oligomeric silsesquioxane." Macromolecular Rapid Communications **26**: 196-200.

Liu, R. Y. F., T. E. Bernal-Lara, A. Hiltner and E. Baer (2004). "Interphase materials by forced assembly of glassy polymers." Macromolecules **37**(6972-6979).

Liu, R. Y. F., T. E. Bernal-Lara, A. Hiltner and E. Baer (2004). "Polymer interphase materials by forced assembly." Macromolecules **38**: 4819-4827.

Liu, R. Y. F., Y. Jin, A. Hiltner and E. Baer (2003). "Probing nanoscale polymer interactions by forced-assembly." Macromolecular Rapid Communications **24**(16): 943-948.

Liu, R. Y. F., A. P. Ranade, H. P. Wang, T. E. Bernal-Lara, A. Hiltner and E. Baer (2006). "Forced assembly of polymer nanolayers thinner than the interphase." Macromolecules.

Liu, X., T. P. Bigioni, Y. Xu, A. M. Cassell and B. A. Cruden (2006). "Vertically aligned dense carbon nanotube growth with diameter control by block copolymer micelle catalyst templates." Journal of Physical Chemistry B **110**: 20102 - 20106.

Lu, K., J. Jacob, P. Thiyagarajan, V. P. Conticello and D. G. Lynn (2003). "Exploiting amyloid fibril lamination for nanotube self-assembly." Journal of the American Chemical Society **125**: 6391 - 6393.

Lubansky, A. S., D. V. Boger and J. J. Cooper-White (2005). "Batchelor's theory extended to elongated cylindrical or ellipsoidal particles." Journal of Non-Newtonian Fluid Mechanics 130: 57-61.

Macosko, C. and J. Lorntson (1973). "The rheology of two blow-molding polyethylenes." Annual Technology Conference - Society of Plastic Engineers 19: 461-467.

Malkin, A. Y. and C. J. S. Petrie (1997). "Some conditions for rupture of polymeric liquids in extension." Journal of Rheology 41: 1-25.

Manias, E., A. Touny, L. Wu, K. Strawhecker, B. Lu and T. C. Chung (2001). "Polypropylene/Montmorillonite nanocomposites. Review of synthetic routes and materials properties." Chemistry of Materials 13: 3516 - 3523.

Marrucci, G. and G. Ianniruberto (2004). "Interchain pressure effect in extensional flows of entangled polymer melts." Macromolecules 37: 3934-3942.

Mazich, K. A. and S. H. Carr (1983). "The effect of flow on the miscibility of a polymer blend." Journal of Applied Physics 54(10): 5511 - 5514.

McKinley, G. H. (2005). Stretched to breaking point; Transient extensional rheology from the melt to the dilute
solution. Society of Rheology Annual meeting, Lubbock, TX.

McKinley, G. H. and O. Hassager (1999). "The considère condition and rapid stretching of linear and branched polymer melts." Journal of Rheology 43: 1195 - 1212.

McKinley, G. H. and T. Sridhar (2002). "Filament stretching rheometry of complex liquids." Annual Review of Fluid Mechanics 34: 375 - 415.

McLeish, T. C. B. and R. G. Larson (1998). "Molecular constitutive equations for a class of branched polymers: The Pom–Pom model,"." Journal of Rheology 42: 81 - 110.

Meissner, J. (1985). "Experimental aspects in polymer melt elongational rheology." Chemical Engineering Communications 33: 159 - 180.

Meissner, J. and J. Hostettler (1994). "A new elongational rheometer for polymer melts and other highly viscoelastic liquids." Rheologica Acta 33: 1-21.

Moniruzzaman, M. and K. I. Winey (2006). "Polymer nanocomposites containing carbon nanotubes." Macromolecules 39: 5194 - 5205.

Mueller, C., V. Topolkaraev, D. Soerens, A. Hiltner and E. Baer (2000). "Breathable polymer films produced by the microlayer coextrusion process." Journal of Applied Polymer Science 78: 816-828.

Munstedt, H. (1979). "New universal extensional rheometer for polymer melts. Measurements on a polystyrene sample." Journal of Rheology 24: 847 - 867.

Munstedt, H., S. Kurzbeck and L. Egersdorfer (1998). "Influence of molecular structure on rheological properties of polyethylenes—Part II: Elongational behavior,"." Rheologica Acta 37: 21-29.

Munstedt, H. and H. M. Laun (1979). "Elongational behavior of a low density polyethylene melt. II. Transient behavior in constant stretching rate and tensile creep experiments. Comparison with shear data. Temperature dependence of the elongational properties." Rheologica Acta 18: 492-504.

Munstedt, H. and H. M. Laun (1981). "Elongational properties and molecular structure of polyethylene melts." Rheologica Acta 20: 211-221.

Nazarenko, S., A. Hiltner and E. Baer (1999). "Polymer microlayer structures with anisotropic conductivity." Journal of Materials Science 34: 1461-1470.

Nolte, A. J., M. F. Rubner and R. E. Cohen (2004). "Creating effective refractive index gradients within polyelectrolyte multilayer films: molecularly assembled rugate filters." Langmuir 20(8): 3304-3310.

Okamoto, M., A. Kojima and T. Kotaka (1998). "Elongational flow and birefringence of low density polyethylene and its blends with ultrahigh molecular weight polyethylene." Polymer 39: 2149-2153.

Okamoto, M., P. H. Nam, P. Maiti, T. Kotaka, N. Hasegawa and A. Usuki (2001). "A house of cards structure in polypropylene/clay nanocomposites under elongational flow." Nano Letters 1(6): 295-298.

Okamoto, M., P. H. Nam, P. Maiti, T. Kotaka, T. Nakayama, M. Takada, M. Ohshima, A. Usuki, N. Hasegawa and H. Okamoto (2001). "Biaxial flow-induced alignment of silicate layers in polypropylene/clay nanocomposite foam." Nano Letters 1(9): 503-505.

Oster, G. and D. P. Riley (1952). "Scattering from cylindrical symmetric systems." Acta Crystallographica Section A 5: 272 - 276.

Padmanabhan, M., L. J. Kashagen and C. Macosko (1996). "Transient extensional viscosity from a rotational shear rheometer using fiber-windup technique." Journal of Rheology 40: 473-481.

Palierne, J. F. (1990). "Linear rheology of viscoelastic emulsions withe interfacial tension." Rheologica Acta 29(3): 204-214.

Pavoor, P. V. (2003). Tribological and mechanical characterization of polyelectrolyte multilayer nanoassemblies. CEP. Cambridge, MIT.

Pearson, G. H. and R. W. Connelly (1982). "The use of extensional rheometry to establish operating parameters for
stretching processes." Journal of Applied Polymer Science 27: 969-981.

Pionteck, J., J. Hu, G. Pompe, V. Albrecht, U. Schulze and E. Borsig (2000). "Characterisation of radiation behaviour of polyethylene/polymethacrylates interpenetrating polymer networks." Polymer 41: 7915-7923.

Plantard, G. and M. Papini (2002). "Radiative and electrical properties of granular materials: application to mixtures of insulating and conducting polymers." Journal of Quantitative Spectroscopy & Radiative Transfer 74: 329 - 337.

Prasad, R., V. Pasanovic-Zujo, R. K. Gupta, F. Cser and S. N. Bhattacharya (2004). "Morphology of EVA based nanocomposites under shear and extensional flow." Polymer Engineering and Science 44(7): 1220 - 1230.

Qi, H. J., K. B. K. Teo, K. K. S. Lau, M. C. Boyce, W. I. Milne, J. Robertson and K. K. Gleason (2003). "Determination of mechanical properties of carbon nanotubes and vertically aligned carbon nanotube forests using nanoindentation." Journal of Mechanics and Physics of Solids 51: 2213-2237.

Raffaelle, R. P., B. J. Landi, J. D. Harris, S. G. Bailey and A. F. Hepp (2005). "Carbon nanotubes for power applications." Materials Science and Engineering B 116: 233-243.

Rasmussen, H. K., J. K. Nielsen, A. Bach and O. Hassager (2005). "Viscosity Overshoot in the Start-Up of Uniaxial Elongation of Low Density Polyethylene Melts." Journal of Rheology 49: 369-381.

Rauschenberger, V. and H. M. Laun (1997). "A recursive model for rheotens tests." Journal of Rheology 41: 719-737.

Register, R. A. (2003). "On the straight and narrow." Nature 424: 378-379.

Romo-Uribe, A., P. T. Mather, T. S. Haddad and J. D. Lichtenhan (1998). "Viscoelastic and morphological behavior or hybrid styryl-based polyhedral oligomeric silsesquioxane (POSS) copolymers." Journal of Polymer Science: Part B: Polymer Physics 36: 1857 - 1872.

Rouse, J. H. and P. T. Lillehei (2003). "Electrostatic assembly of polymer/single walled carbon nanotube multilayer films." Nano Letters 3(1): 59 - 62.

Saito, T. and C. W. Macosko (2002). "Interfacial crosslinking and diffusion via extensional rheometry." Polymer Engineering and Science 42(1-9).

Schaefer, D. W., J. Zhao, J. M. Brown, D. P. Anderson and D. W. Tomlin (2003). "Morphology of dispersed carbon single-walled nanotubes." Chemical Physics Letters 375: 369-375.

Schrenk, W. J. and T. Alfrey Jr. (1978). Coextruded multilayer polymer films and sheets. Polymer Blends. D. Paul, Academic Press. 2: 129 -165.

Schulze, J. S., T. P. Lodge, C. W. Macosko, J. Hepperle, H. Munstedt, H. Bastian, D. Ferri, J. Groves, Y.-H. Kim, M. Lyon, T. Schweizer, T. Virkler, W. Wassner and W. Zoetelief (2001). "A comparison of extensional viscosity measurements from various RME rheometers." Rheologica Acta 40: 457-466.

Schweizer, T. (2000). "The uniaxial elongational rheometer RME—Six years of experience." Rheologica Acta 39: 428-443.

Sentmanat, M., B. N. Wang and G. H. McKinley (2005). "Measuring the transient extensional rheology of polyethylene melts using the SER universal testing platform." Journal of Rheology 49(3): 586-606.

Sentmanat, M. L. (2003). Dual windup extensional rheometer. US.

Sentmanat, M. L. (2003). A novel device for characterizing polymer flows in uniaxial extension. ANTEC.

Sentmanat, M. L. (2004). "Miniature universal testing platform: From extensional melt rheology to solid-state deformation behavior." Rheologica Acta 43: 657-669.

Sheng, N., M. C. Boyce, D. M. Parks, G. C. Rutledge, J. I. Abes and R. E. Cohen (2004). "Multiscale micromechanical modeling of polymer/clay nanocomposites and the effective clay particle." Polymer 45: 487 - 506.

Silberberg, A. and W. Kuhn (1952). "Miscibility of liquids influenced by rate of shear." Nature 170: 450 - 451.

Snow, E. S., J. P. Novak, P. M. Campbell and D. Park (2003). "Random networks of carbon nanotubes as an electronic material." Applied Physics Letters 82(13): 2145-2147.

Soong, S. Y., R. E. Cohen, M. C. Boyce and A. D. Mulliken (2006). "Rate-dependent deformation behavior of POSS-filled and plasticized poly(vinyl chloride)." Macromolecules 39: 2900 - 2908.

Sridhar, T. (1990). "An overview of the project M1." Journal of Non-Newtonian Fluid Mechanics 35(85-95).

Sulaiman, S., C. M. Brick, C. M. De Sana, J. M. Katzenstein, R. M. Laine and R. A. Basheer (2006). "Tailoring the global properties of nanocomposites. Epoxy resins with very low coefficients of thermal expansion." Macromolecules 39(16): 5167-5169.

Tangirala, R., E. Baer, A. Hiltner and C. Weder (2004). "Photpatternable reflective films produced by nanolayer extrusion." Advanced Functional Materials 14(5): 1 - 11.

Tanoue, S., L. A. Utracki, A. Garcia-Rejon, P. Sammut, M. Ton-That, I. Pesneau, M. R. Kamal and J. Lyngaae-Jorgensen (2004). "Melt compounding of different grades of polystyrene with organoclay. Part 2: Rheological properties." Polymer Engineering and Science 44(6): 1061 - 1076.

Torres, A., A. N. Hrymak, J. Vlachopoulos, J. Dooley and B. T. Hilton (1993). "Boundary conditions for contact lines in coextrusion flows." Rheologica Acta 32: 513-525.

Turri, S. and M. Levi (2005). "Structure, dynamic properties, and surface behavior of nanostructured ionomierc polyurethanes form reactive polyhedral oligomeric silsesquioxanes." Macromolecules 38: 5569 - 5574.

Utracki, L. A. and J. Lara (1984). "Extensional flow of mica-filled polyethylene." Polymer Composites 5(1): 44-51.

van der Hoeven, J. C., R. Wimberger-Friedl and H. E. H. Meijer (2001). "Homogeneity of multilayers produced with a static mixer." Polymer Engineering and Science 41(1): 32-42.

Verbeeten, W. M. H., G. W. M. Peters and F. P. T. Baaijens (2001). "Differential constitutive equations for polymer melts: The extended Pom–Pom model." Journal of Rheology 45: 823-843.

Vermogen, A., K. Masenelli-Varlot, R. Seguela, J. Duchet-Rumeau, A. Boucard and P. Prele (2005). "Evaluation of the structure and dispersion in polymer-layered silicate nanocomposites." Macromolecules 38: 9661 - 9669.

Wang, B. N., R. D. Bennett, E. Verploegen, A. J. Hart and R. E. Cohen (2007). "Quantitative characterization of the morphology of multi-wall carbon nanotube films by small-angle x-ray scattering." Journal of Physical Chemistry C 1: (Web ASAP).

Wang, H., Z. Xu and G. Eres (2006). "Order in vertically aligned carbon nanotube arrays." Applied Physics Letters 88: 213111: 1-3.

Wang, T. C., R. E. Cohen and M. F. Rubner (2002). "Metallodielectric photonic structures based on polyelectrolyte multilayers." Advanced Materials 13(21): 1534.

Wang, W., Q. Wu and Z. Qi (2003). "Unusual rheology behavior of ultra high molecular weight polyethylene/kaolin
composites prepared via polymerization-filling." Polymer International 52: 1078-1082.

Weber, M. F., C. A. Stover, L. R. Gilbert, T. J. Nevitt and A. J. Ouderkirk (2000). "Giant birefringent optics in multilayer polymer mirror." Science 287: 2451 - 2456.

Wei, B., R. Vajtai, Y. Y. Choi, P. M. Ajayan, H. Zhu, C. Xu and D. Wu (2002). "Structural characterizations of long single-walled carbon nanotube strands." Nano Letters 2(10): 1105-1107.

Wei, B. Q., R. Vajtai, Y. Jung, J. Ward, R. Zhang, G. Ramanath and P. M. Ajayan (2002). "Organized assembly of carbon nanotubes." Nature 416: 495 - 496.

Wei, B. Q., R. Vajtai, Y. Jung, R. Zhang, G. Ramanath and P. M. Ajayan (2003). "Assembly of highly organized carbon nanotube architectures by chemical vapor deposition." Chemistry of Materials 15: 1598 - 1606.

Whitesides, G. M. and B. Grzybowski (2002). "Self-assembly at all scales." Science 295: 2418 - 2421.

Wiest, J. M. (1989). "A differential constitutive equation for polymer melts." Rheologica Acta 28: 4-12.

Wilson, G. M. and B. Khomami (1993). "An experimental investigation of interrfacial instabilities in multilayer flow of viscoelastic fluids. II. Elastic and nonlinear effects in incompatible polymer systems." Journal of Rheology 37(2): 315-339.

Xu, Y., W. J. Brittain, C. Xue and R. K. Eby (2004). "Effect of clay type on morphology and thermal stability of PMMA-clay nanocomposites prepared by heterocoagulation method." Polymer 45: 3735-3746.

Yao, M., G. H. McKinley and B. Debbaut (1998). "Extensional deformation, stress relaxation and necking failure of viscoelastic filaments." Journal of Non-Newtonian Fluid Mechanics 79: 469-501.

Zhang, J., T. P. Lodge and C. Macosko (2006). "Interfacial slip reduces polymer-polymer adhesion during coextrusion." Journal of Rheology 50(1): 41-57.

Zhang, L., Z. Li, Y. Tan, G. Lolli, N. Sakulchaicharoen, F. G. Requejo, B. S. Mun and D. E. Resasco (2006). "Influence of a top crust of entangled nanotubes on the structure of vertically aligned forests of single-walled carbon nanotubes." Chemistry of Materials 18(23): 5624-5629.

Zhao, J., A. B. Morgan and J. D. Harris (2005). "Rheological characterization of polystyrene-clay nanocomposites to compare the degree of exfoliation and dispersion." Polymer 46: 8641 - 8660.

Zhao, R. and C. W. Macosko (2002). "Slip at polymer-polymer interfaces: rheological measurements on coextruded multilayers." Journal of Rheology 46(1): 145 - 167.

10. APPENDICES

10.1. RHEOLOGY AND MORPHOLOGY OF PC/PMMA MULTILAYERS

Multilayer coextrusion is an advanced polymer processing technique developed in the 1960's which is used to create composite films with complex hierarchical structures from two or more polymeric extrusion streams. (Alfrey Jr. and Schrenk 1980) Using this technique it is straightforward to incorporate POSS, clay or CNTs into a hierarchical structure provided by the multilayer film. The characteristic length scale of the structure spans many orders of magnitude, ranging from millimeters to nanometers. As opposed to self-assembly, these films are assembled by mechanically confining the extrusion stream and controlling the process die structure and the rheology of the extrusion streams. Thus the process has been called "forced assembly." The essential technology relies on two types of processing dies: 1) a feedblock and 2) layer multiplication or 'cut-and-fold' dies. An example of the multilayer coextrusion setup is shown in Figure 10-1.
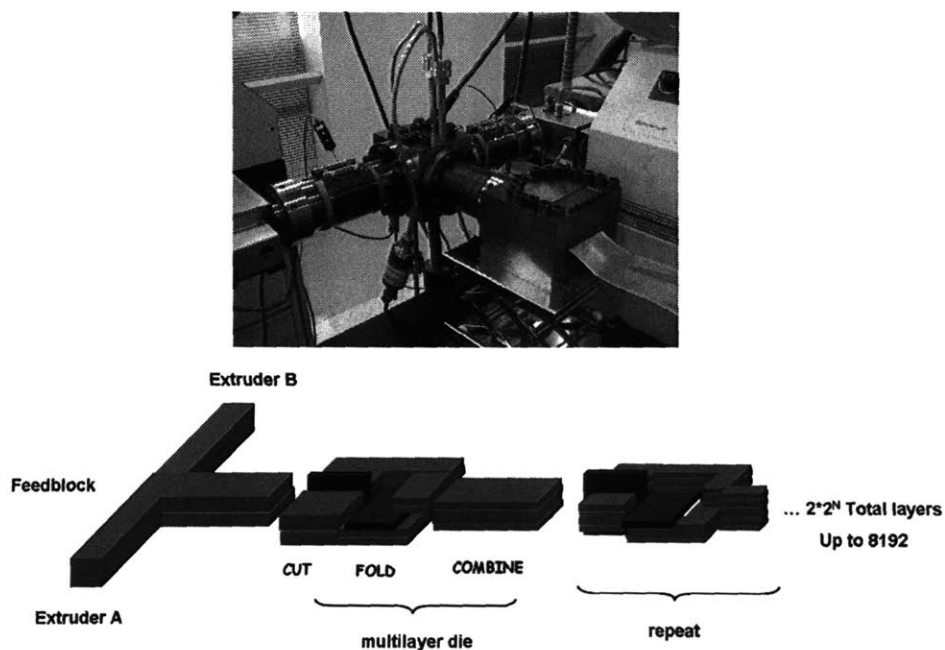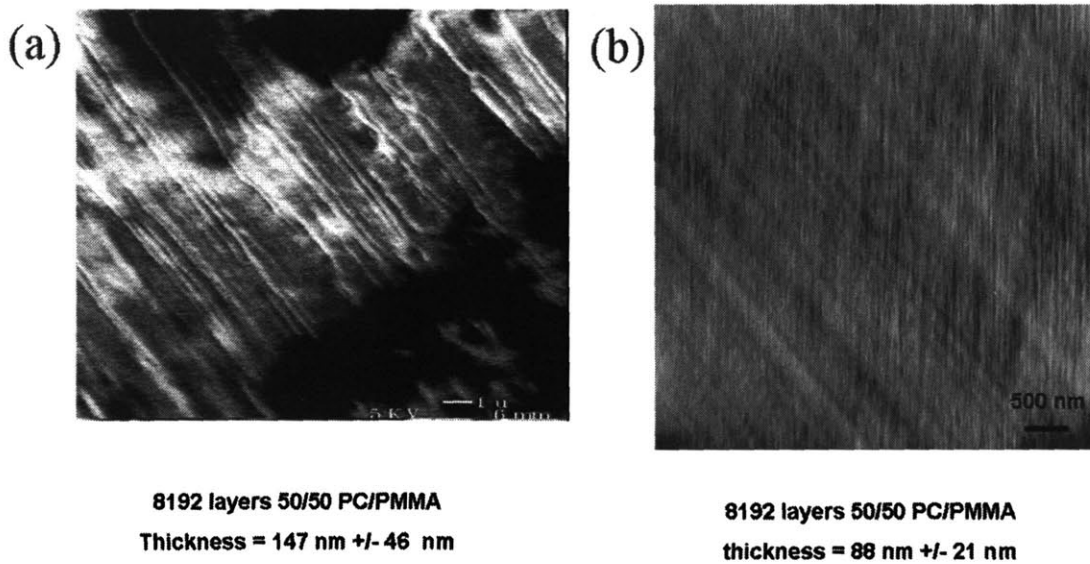

Figure 10-1. Multilayer coextrusion assembly (above) Photograph of square feedblock, series of layer multiplication dies, and an adjustable lip sheeting die. (below) Schematic representation of flow through the multilayer die assembly.

Though several morphologies are possible, a standard feedblock stratifies one stream over another, as illustrated above. When quenched the exiting film exhibits a lamellar morphology. Figure 10-2 shows a cross sectional SEM micrograph and atomic-force micrograph of a 50/50 PC/PMMA multilayer (where 50/50 denotes percentage contribution of flow rates from each extruder). The thicknesses of the layers are governed by three parameters: the relative flow rates from the extrusion streams which dictate both the composition and the relative thicknesses of the layers (neglecting any changes in density), the number of layer multiplication dies, N, and the final film thickness, t_{film}, determines individual film thicknesses, t_i, by:

$$t_i = \frac{q_i}{2^N} t_{film} \qquad\qquad (10\text{-}1)$$

where q_i is the relative flow rate of extrusion stream i. An example of this is shown in Figure 10-3.

(a)

8192 layers 50/50 PC/PMMA
Thickness = 147 nm +/- 46 nm

(b)

8192 layers 50/50 PC/PMMA
thickness = 88 nm +/- 21 nm

Figure 10-2. Cross-sectional micrographs from (a) SEM and (b) AFM, show lamellar morphology.
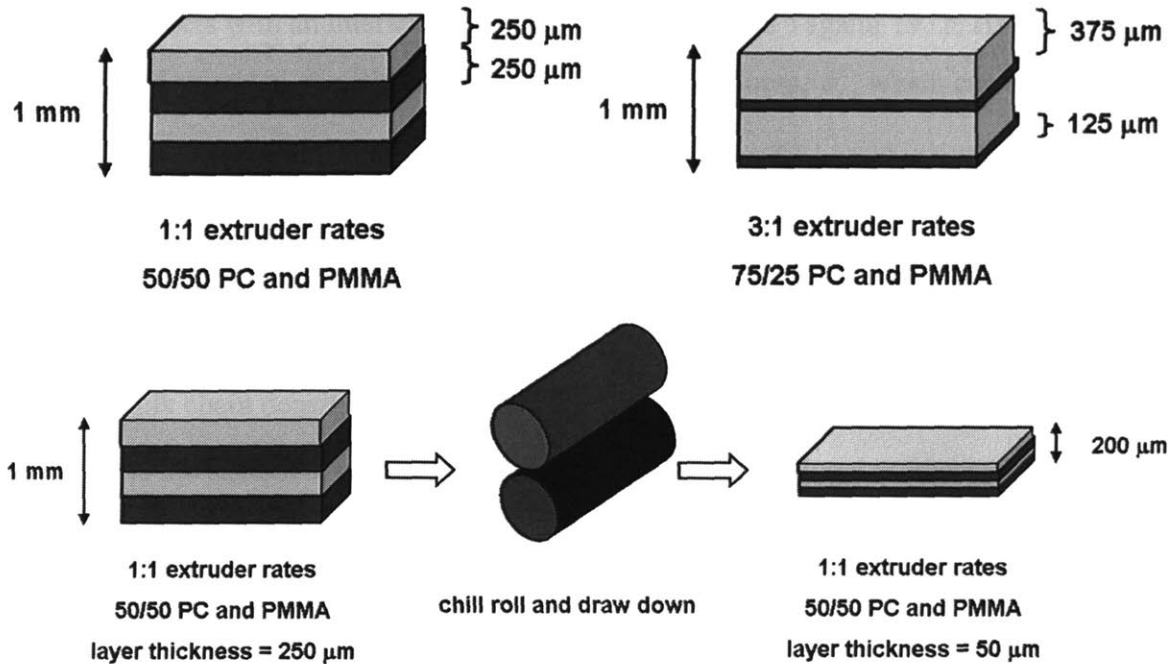
Figure 10-3. Example of how individual layer thicknesses are controlled by the relative extruder flow rates, q_i, (above) and the final film thickness, t_{film} (below).
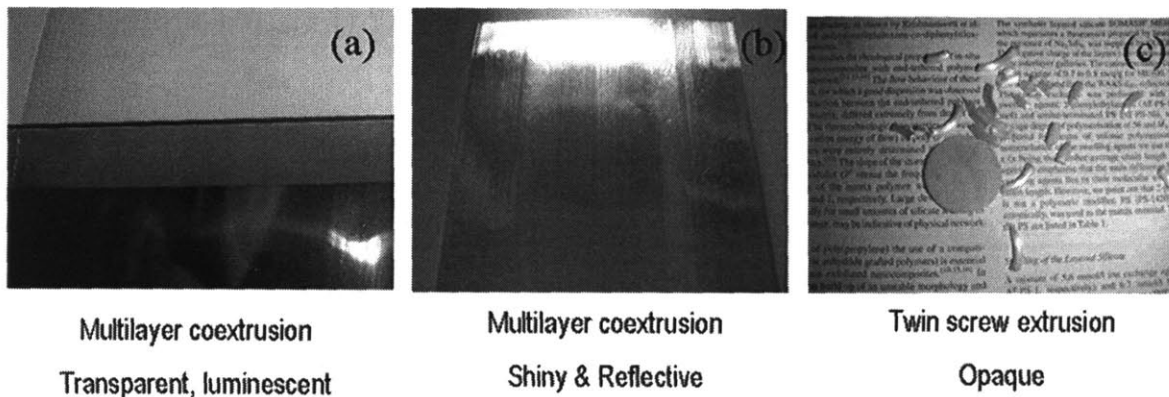
Multilayer coextruded films have shown remarkable improvement in properties over traditional composites. Observable success has been demonstrated for synergistic energy absorption in PC/PMMA multilayers (Kerns *et al.* 1999; Kerns *et al.* 2000), tailoring conductivity (Nazarenko *et al.* 1999) , barrier properties (Mueller *et al.* 2000; Jarus *et al.* 2002), and producing interesting optical effects (Chen *et al.* 1999; Weber *et al.* 2000; Tangirala *et al.* 2004). Indeed a simple visual comparison of three blends of polycarbonate (PC) and PMMA with the same volume fractions immediately illustrates how the morphology of blends can control the bulk properties (see Figure 10-4).

Recently methods for fabricating multilayers with layer thicknesses less than 20 nanometers has been demonstrated. (Liu *et al.* 2003; Liu *et al.* 2004; Liu *et al.* 2004; Liu *et al.* 2006) The resulting properties, such as the glass transition temperature, have been shown to have strong layer thickness dependence. This originates from an increased volume fraction of the interfacial region, or "interphase", where polymers from adjacent layers mix. The "interphase" has dimensions on the order of a few nanometers. Helfand and Tagami developed a theory for

171

symmetric polymers with an interaction parameter (Helfand and Tagami 1972; Helfand and Sapse 1975) and provided an estimate for the interfacial thickness, a_I, which can be determined from:

$$a_I = \left| \rho_0 \left[\frac{d\rho_A}{dz} \bigg|_{z=0} \right]^{-1} \right| = \frac{2b}{(6\chi)^{1/2}} \qquad (10\text{-}2)$$

where ρ_0 is bulk chain density, ρ_A is the density of chains of type A (versus B), z is the length dimension, b is the statistical segment length and χ is the Flory-Huggins interaction parameter. Representative predictions from this theory for PS, PMMA, and PC pairs are shown in Figure 10-5, illustrating the change in density of type A across the interphase as a function of χ.

(a)	(b)	(c)
Multilayer coextrusion	Multilayer coextrusion	Twin screw extrusion
Transparent, luminescent	Shiny & Reflective	Opaque

Figure 10-4. Three films of 50/50 PC/PMMA are shown as (a) 8192 layers of a multilayer with $t_{film} = 0.09$ mm, (b) 8192 layers of a multilayer with $t_{film} = 0.9$ mm, and (c) blended in a twin-screw extruder. The variation in optical properties goes from transparent to reflective to opaque, reflecting the underlying morphology of the blend.

For typical layer thicknesses, the volume fraction of the interphase is small. However as layer thicknesses decrease to nanometer dimensions, the length scales of the individual layers and the interphase become comparable, and the relative contribution of the properties of the interphase becomes larger. The film, which has macroscopic properties determined by a compositional average, behaves differently to reflect the larger volumetric contribution of the interphase. Liu *et al.* demonstrated how the permeability through thin multilayer films from several different polymer pairs increases above the native permeability of either constituent

polymer at layer thicknesses less than approximately ten times the interfacial thickness calculated from Equation 10-2. (Liu *et al.* 2004) For a PC/PMMA system which exhibits two distinct T_gs in differential scanning calorimetry or dynamic mechanical analysis, shows a convergence to a single T_g representative of the thermal characteristics of the interphase (see Figure 10-6), which obeys the Fox equation:

$$\left(\frac{1}{T_g}\right)_{composite} = \left(\frac{w_1}{T_g}\right)_1 + \left(\frac{w_2}{T_g}\right)_2 \qquad (10\text{-}3)$$

where w represents the weight fraction of the constituent polymers. The interfacial volume fraction was calculated by:

$$\phi_{interface} = \frac{a_I\left(N_{layers} - 1\right)}{t_{film}} \qquad (10\text{-}4)$$
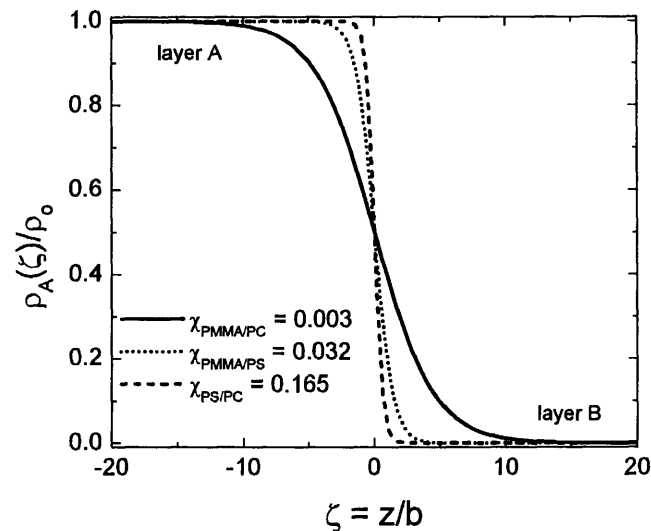
Figure 10-5. Predictions from Helfand-Tagami theory for symmetric polymer interfaces
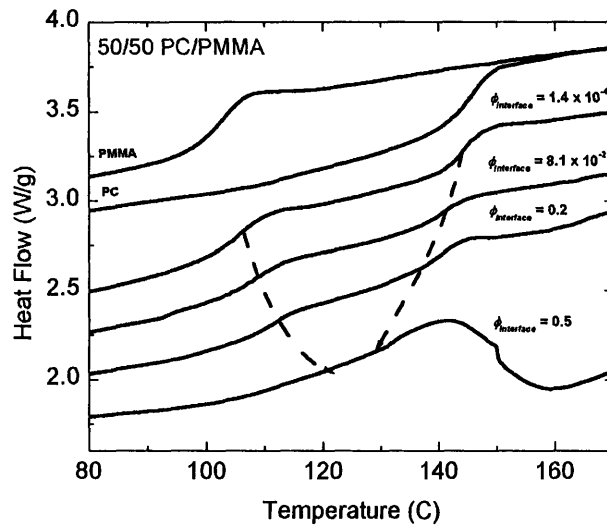
Figure 10-6. Multilayers demonstrate convergence of T_gs in DSC as volume fraction of interphase is increased.

The large changes in morphological properties can have a large impact on the rheology of coextruded multilayers. A general characterization of the rheology clearly has importance in tailoring the extrusion process as multilayer coextrusion is highly sensitive to mismatches in rheological properties including shear viscosity or elasticity. Differences in these properties can give rise to secondary flows, interfacial instabilities and layer rearrangement. A large body of experimental and theoretical work has been developed to address flow in a coextrusion process, demonstrating the necessity of careful control of processing parameters to maintain the morphological integrity of the multilayer film (Han et al. 1982; Hinch et al. 1992; Larson 1992; Torres et al. 1993; Wilson and Khomami 1993; Dooley et al. 1998; Kwon and Zumbrunnen 2001; van der Hoeven et al. 2001). Thus the a priori characterizations of rheological material functions are crucial to the construction of the films.

In addition rheology can provide a sensitive characterization of the underlying morphology properties of the coextruded multilayer. Because of the large and quantifiable volume fraction of interphase in coextruded multilayers, the films can be used to supply quantitative measurements of the interfacial tension between polymer pairs. Many theoretical

and experimental developments have been performed (Palierne 1990; Gramespacher and Meissner 1992; Graebling *et al.* 1993; Delaby *et al.* 1995; Gramespacher and Meissner 1995; Gramespacher and Meissner 1997; Levitt and Macosko 1997; Handge and Potschke 2004). Recently Zhao and Macosko demonstrated that measurements of lower than expected shear viscosities reveal the presence of apparent slip at the interface between immiscible polymer pairs (Zhao and Macosko 2002). Utilizing the theoretical treatment of Goveas and Fredrickson (Goveas and Fredrickson 1998), they determined that reduced entanglement density due to enthalpic interactions between dissimilar polymer pairs. Thus they provide a formalism whereby the nature of the interface (Rouse-like or entangled) can be determined. Zhang *et al.* extend the analysis to illustrate how bulk properties, such as adhesion between layers, is affected by the thermodynamic incompatibility during processing (Zhang *et al.* 2006).

Figure 10-7 compares the values for zero-shear viscosities, η_0, and the complex viscosities, η^*, for PMMA, PC, 50/50 PC/PMMA multilayers, and twin-screw extruded (TSE) blends of 50% wt./wt. PC and PMMA. Although PC and PMMA do not exhibit strong immiscibility (i.e. the interfacial tension is relatively small), measured viscosities for the 50/50 PC/PMMA multilayer are both lower than the expected value determined by the log-additive rule:

$$\log \eta_{\text{composite}} = \sum_i \phi_i \log \eta_i \qquad (10\text{-}5)$$

and also lower than the measured value of the least viscous constituent polymer. This is a clear experimental indication of apparent slip at the interface of PC and PMMA. It is noteworthy that we observe a reduction in viscosity in SAOS, whereas Zhao *et al.* were not able to observe apparent slip in dynamic oscillation. This difference with our system of PC/PMMA can arise from several different factors including applied shear stress, higher number of layers, molecular weight of the polymer chains, and the choice of polymers themselves (along with relevant corresponding properties such as molecular weight between entanglements, M_e). They restricted their measurements to layer numbers below 64 to avoid the possibility of layer rearrangement and corresponding loss of the lamellar morphology. With 8192 layers, our films can provide over

two orders of magnitude more interfacial material, which allows for a more sensitive measurement of the rheology of the interface.
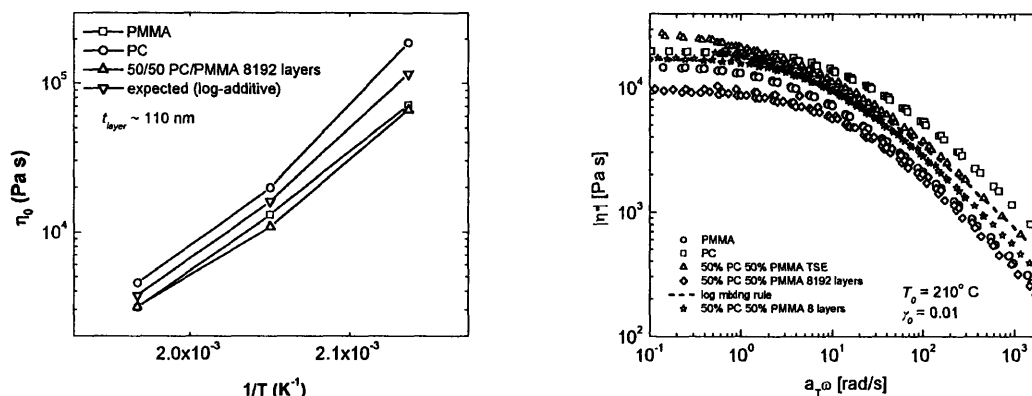

Figure 10-7. Comparison of zero-shear viscosities (left) and complex viscosities (right) for PC, PMMA and 50/50 PC/PMMA multilayers.

Figure 10-8 shows a comparison of storage moduli, G', for PC, PMMA, a multilayer, and a blend formed by twin-screw extrusion (TSE) measured from 160° $C \le T \le 230^\circ$ C and shifted using time-temperature superposition to a reference temperature of $T_0 = 190^\circ$ C. Both PC and PMMA exhibit typical terminal behavior at frequencies $\omega < 1$ rad/s with the characteristic slope of -2. The blends shows a broad, low frequency plateau around $\omega < 10^{-3}$ rad/s which is characteristic of polymer blends that form a dispersion or emulsion (Palierne 1990; Graebling *et al.* 1993). Palierne illustrated that small deformation of droplets which recover in the presence of interfacial tension can give rise to a long relaxation times which and developed a theoretical model which can prdict this plateau assuming spherical inclusions in a matrix and given the rheological properties of the polymers, interfacial tension between the polymers, and the size distribution of spheres. The data for the blend formed by TSE shows the onset of the plateau at frequencies as large as $\omega \approx 0.1$ rad/s and that clearly TTS does not hold for the blend at lower frequencies. However, the data for the multilayer does not show deviation from TTS until very low frequencies, below $\omega < 10^{-3}$ rad/s. We expect that the blend from TSE would give rise to morphologies such as dispersed droplets or a co-continuous interpenetrated structure (see Figure 10-9). These morphologies tend to give rise to an increase in the interfacial area during

176

deformation, resulting in the plateau in storage modulus. However shear deformation of the lamellar morphology of the multilayer in SAOS, with the layers aligned parallel to the shearing plates, results in the layers "sliding" along one another. This results in the observed apparent slip, but does not generate additional interface through the deformation. Thus we do not expect a Palierne-type plateau in G' for measurement of the multilayer. At high measurement temperatures, corresponding to low values of $a_T\omega$, the plateau does appear as layers break up into distinct droplets driven by interfacial energy and increased mobility of the chains. From the measurements of G', we believe that we do not have layer break up prior for measurements taken $T \leq 220^o$ C and that SAOS measurements can accurately reveal the rheological nature of the interface for PC/PMMA multilayers..
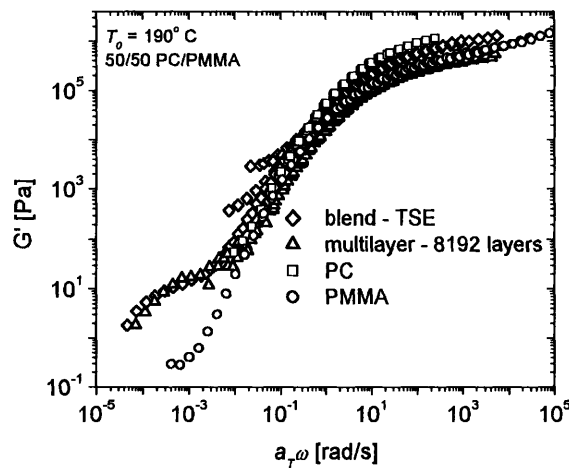

Figure 10-8. Measurements of storage modulus illustrating low frequency plateau corresponding to long relaxation time associated with presence of non-lamellar morphology (droplets or co-continuous structure).
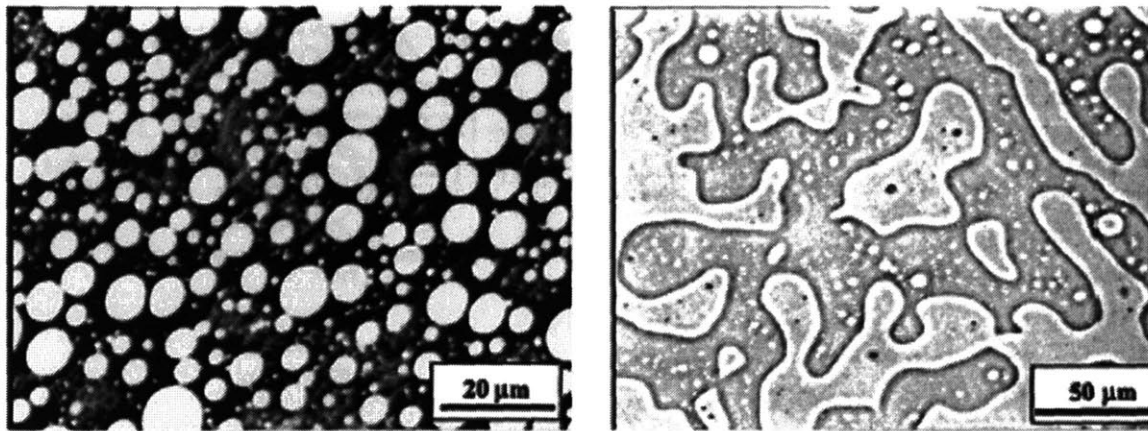
Figure 10-9. Example of PS/PMMA blends in droplet (left) and co-continuous interpenetrated morphology (right). Adapted from (Handge and Potschke 2004)

Thus we have extended the experimental methodology, introduced by Zhao and Macosko, which can measure the relationship between the interactions between polymer pairs (as defined by interfacial tension of the Flory-Huggins interaction parameter, χ) and the resulting bulk rheology of the interface and the film. We combine the experimental formalism with the theoretical predictions of Goveas and Fredrickson, which was also discussed in Zhao and Macosko, which examined the limiting cases of apparent slip if the interface demonstrated either Rouse-like or entangled behavior (Goveas and Fredrickson 1998). Figure 10-10 illustrates two limiting cases for entangled melts and our physical interpretation of deformation at the interface during shear flow. Using molecular arguments Goveas and Fredrickson develop the expected central theme that Rouse-like interfaces should give rise to more apparent slip than an entangled interface. In addition they offer expressions for the shear viscosities in the two limiting cases which we can compare to our experimental results, shown in Figure 10-11. The predictions for the entangled and Rouse-like interface indeed bound the experimental results determined from SAOS. It is reasonable to conclude that the rheological nature of the interface in PC/PMMA multilayers exhibits a reduced entanglement density. This is a reasonable conclusion, given the relatively small interaction between PC and PMMA which is markedly amplified by the large volume of interface.

178
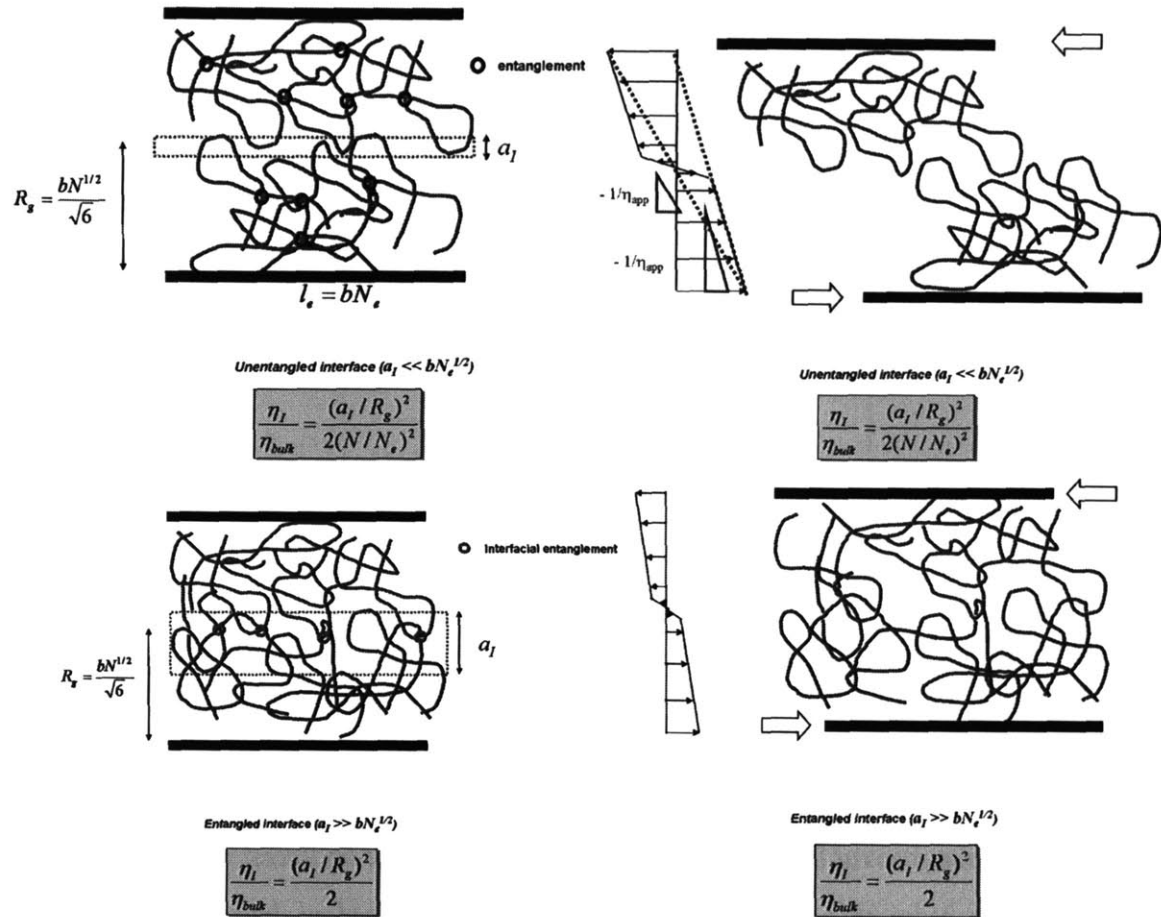
Figure 10-10. Illustration of differences between Rouse-like interface and entangled interface. Rouse-like behavior for the interface is shown on top with and without shear (right and left, respectively). Entangled interface is shown below with and without shear (right and left, respectively).

In summary we demonstrated the fabrication of PC/PMMA multilayers using coextrusion. We were able to validate the lamellar morphology using SEM and AFM and demonstrated the large presence of kinetically "locked-in" interphase resulting in the measurement of a converged T_g in DSC. Using dynamic oscillation and steady-shear measurements, we observed a bulk reduction in the viscosity of PC/PMMA multilayers and the presence of a long relaxation time plateau in the storage modulus, consistent with loss of layer integrity at higher measurement temperatures. Using previously developed theoretical predictions, we determined that our measurements for viscosity suggest a small reduction in entanglement density at the interface.
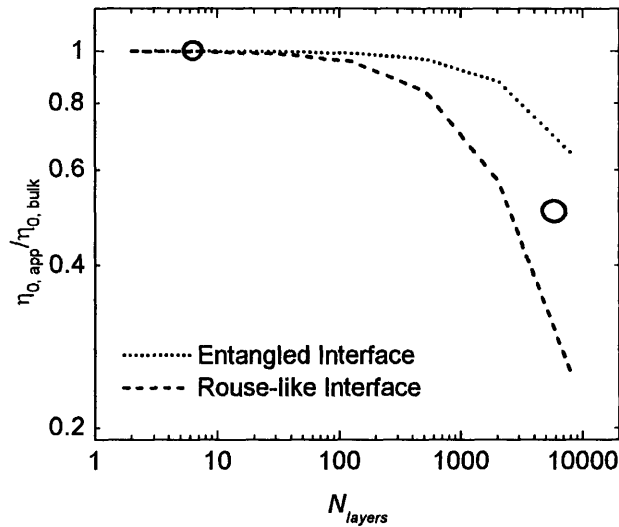
Figure 10-11. Experimental measurements of shear viscosity of 50/50 PC/PMMA compared to the bounds established by the theoretical work of Goveas and Fredrickson (Goveas and Fredrickson 1998).

Though the relevant parameter space for further rheological investigations of coextruded multilayer films is broad, including such changes as χ, M_w, M_e, a straightforward extension would be to look at different polymer pairs which could give rise to changes in several of these variables. We expect that a through investigation of PC, PS and PMMA multilayers would yield a graph akin to Figure 10-12.
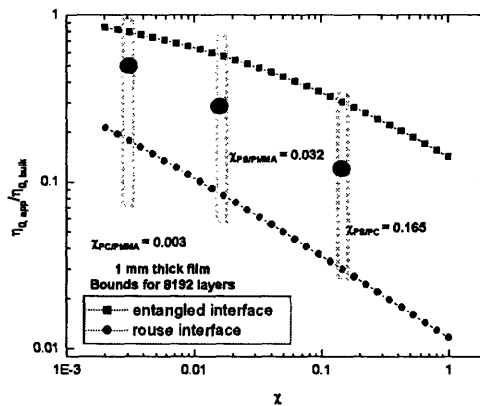
Figure 10-12. Anticipated rheological behavior of multilayers as a function of χ.
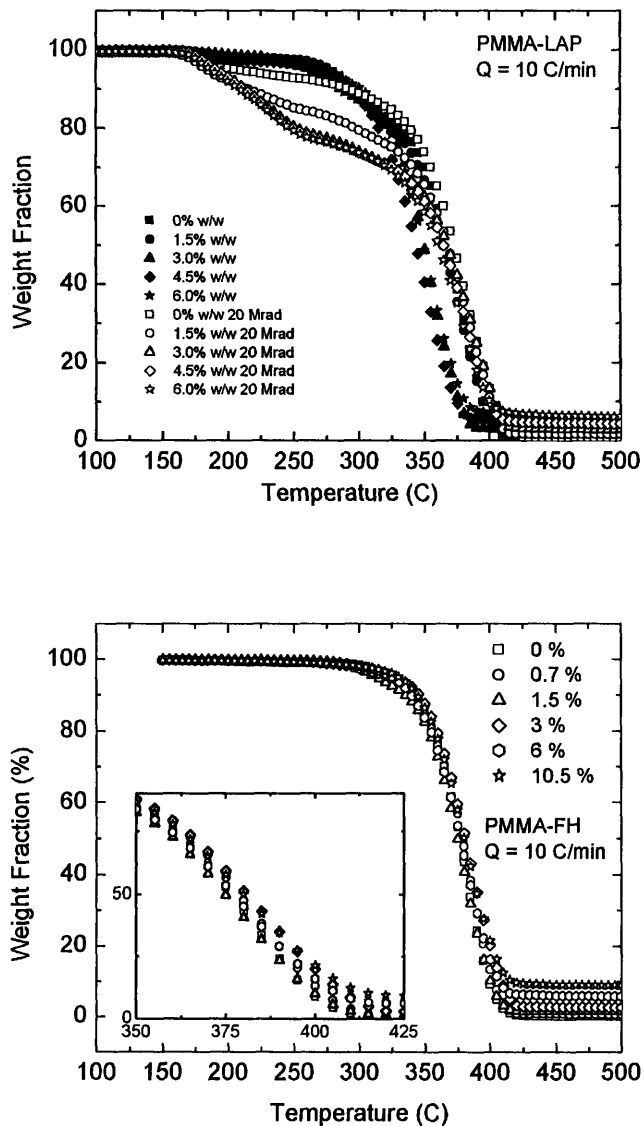
10.2. ELECTRON BEAM IRRADIATION OF PMMA

Electron beam irradiation has been shown to be effective at cleaving polymer chains which can have a negative impact on the mechanical properties of polymers (Kudoh *et al.* 1996; Pionteck *et al.* 2000). However for the rheological experiments with PMMA-Laponite nanocomposites synthesized by emulsion polymerization in Chapter 6, the as-synthesized molecular weights were too high to be accessed by melt shear rheology. Normally this can be ameliorated using a higher measurement temperature and invoking the principle of time-temperature superposition. However, as shown in Figure 10-13, thermal degradation of the PMMA is onset around $T_0 = 270^\circ$ C, which does not expand the experimental frequency window sufficiently. Because of the high M_w of the PMMA, the reptation time, τ_p, is long and the rubbery plateau extends to very low frequencies, $\omega < 10^{-1}$ rad/s, as shown in the left panel of Figure 10-14. After exposure to 20 MRads of electron beam radiation, the rubbery plateau extends to only frequencies of $\omega \sim 10^1$ rad/s, which allows for the experimental observation of the low frequency plateau associated with the network of percolated clay sheets.

To certify that the change in rheological properties is the result of a decrease in the molecular weight of the polymeric matrix, gel permeation chromatography (GPC) was performed on the as-synthesized PMMA before and after irradiation. From Figure 10-15, we observe more than an order of magnitude decrease in the M_w, and a normal distribution around the mean, confirming the reduction in molecular weight of the matrix.

There are a few drawbacks associated with the use of electron beam irradiation for polymer chain cleavage. The TGA curves in Figure 10-13 indicate the earlier onset of thermal degradation to temperatures above $T > 190^\circ$ C, which necessitated the use of time-temperatrue superposition (TTS) in the rheological measurements of Chapter 6 and increasing the difficulty of the compression molding process. Furthermore, rheological data in the right panel of Figure 10-15 does not show the expected terminal slope of -2 for the pure PMMA, again indicative of degradation. It is noteworthy that the irradiated samples show greater degradation at higher loadings of clay, which corresponds to the greater weight loss at $T > 250^\circ$ C in the TGA curves

of Figure 10-13. We speculate that this may originate from the presence of the percolated network enhancing transport of the radical species, or serving as loci of radical generation. Despite the drawbacks associate with degradation, electron beam irradiation is a valuable tool for studying filled polymer systems by altering the properties of the matrix and isolating the effect of the filler itself.

Figure 10-13. TGA profiles for PMMA-LAP nanocomposites with (dark symbols) and without (open symbols) electron beam irradiation (above) and TGA profiles for unmodified PMMA-FH (below).
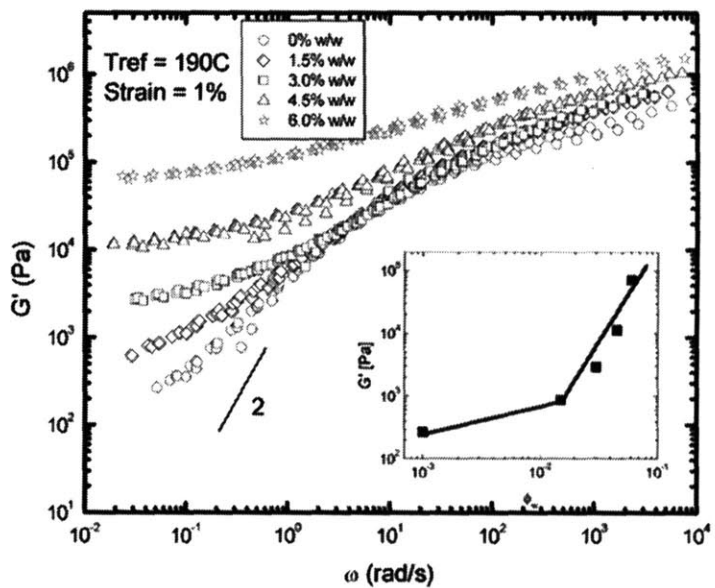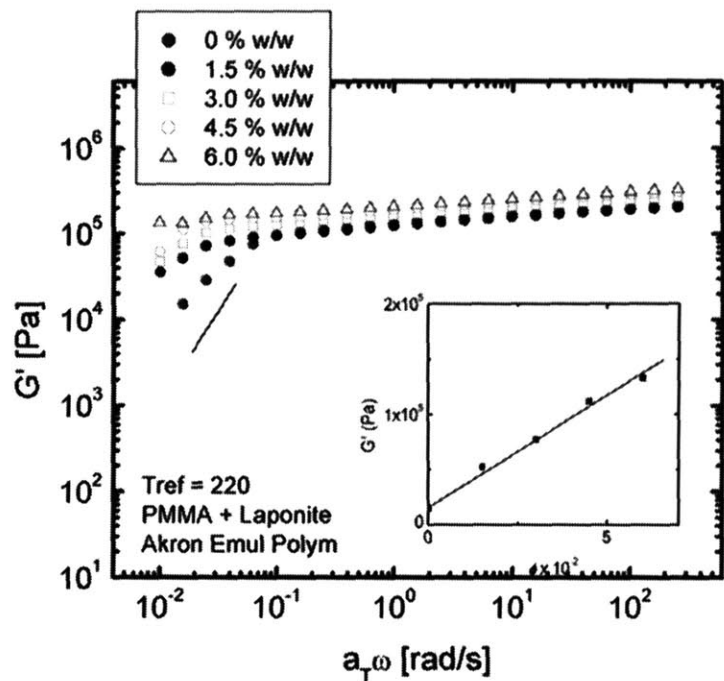
Figure 10-14. A comparison of PMMA-LAP samples before (above) and after (below) exposure to 20 MRads of electron beam radiation.
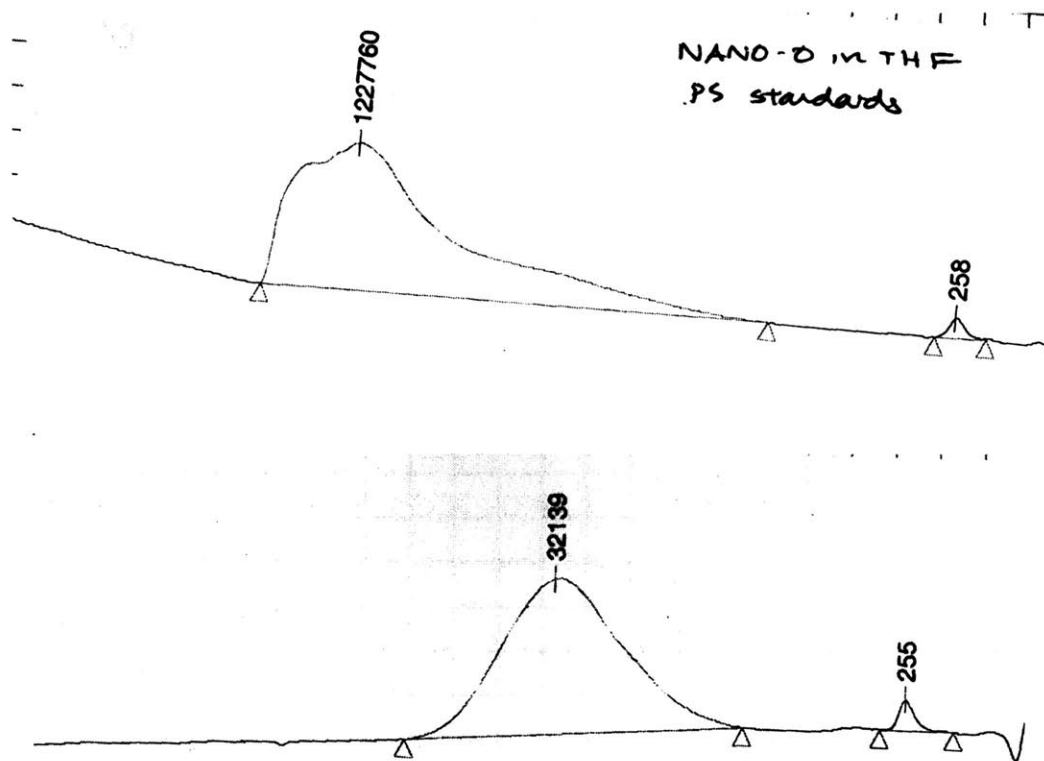
Figure 10-15. GPC traces of emulsion polymerized PMMA before (above) and after (below) exposure to 20MRads of ionizing electron beam radiation.

11. BIOGRAPHICAL INFORMATION

Benjamin Ning-Haw Wang was born in Schenectady, New York moved to Santa Monica, California at a young age and subsequently graduated from the local Santa Monica High School. He attended Stanford University (Stanford, CA) from September 1994 to June 1998, finishing with a Bachelor of Science in Chemical Engineering. He spent his undergraduate summers in industrial research labs at Rockwell Science Center in Thousand Oaks, CA (1995) working on electrochemical deposition for re-writeable printing presses and TRW in Redondo Beach, CA (1996-1998) characterizing compound semiconductor devices grown fom molecular beam epitaxy processes. After graduation, he began work in the microfluidics R&D group at Caliper Technologies in Mountain View, CA, (1998 – 2002) developing enzymatic and cell-based assays for bench-top and high-throughput drug screening applications.

In the autumn of 2002, Ben entered the doctoral program in Chemical Engineering at Massachusetts Institute of Technology in Cambridge, MA. In the second semester he joined the research groups of Professors Robert E. Cohen and Gareth H. McKinley as a co-advised student beginning his thesis work on "Rheological and morphological characterization of hierarchically nanostructured materials."